

© 2019 Andy K. Yoon

HIGH-FREQUENCY, SLOTLESS PERMANENT MAGNET SYNCHRONOUS
MOTOR FOR AIRCRAFT PROPULSION

BY

ANDY K. YOON

DISSERTATION

Submitted in partial fulfillment of the requirements
for the degree of Doctor of Philosophy in Electrical and Computer Engineering
in the Graduate College of the
University of Illinois at Urbana-Champaign, 2019

Urbana, Illinois

Doctoral Committee:

Associate Professor Kiruba Haran, Chair
Assistant Professor Arijit Banerjee
Professor Jianming Jin
Professor Philip T. Krein

ABSTRACT

While electric machines have already shown impact in applications where efficiency, reliability, and cost are critical, newer applications are instigating development of next-generation, lightweight, power-dense motors. The benefit of lower weight in a motor is especially attractive when considered for aerospace applications, such as electric propulsion for aircraft. More specifically, significant reduction of weight and/or volume of the propulsor may allow placement of more batteries for increased overall energy storage capability for the aircraft, or reduction in energy needed during take-off or cruising. In fact, recent analysis has shown that hybridization of commercial aircraft could allow up to 33% reduction in fuel consumption, 55% reduction in NOx emissions at cruise, and 60% reduction in NOx emissions during landing and take-off. Furthermore, the National Aeronautics and Space Administration (NASA) has identified lightweight, low-volume electric machines as one of the key enabling technologies.

This dissertation details work accomplished in the development of a 1 MW, 13 kW/kg, high-frequency electric machine design for improving specific power density for weight- and/or volume-sensitive applications. Analytical models that correspond to this topology are discussed. Slotless topology is compared to conventional slotted motor topology using the analytical models to show slotless topology's potential for high specific power at higher frequencies. Furthermore, the models are used to show the scalability of the high-frequency, slotless machine at different speeds. The results show that the topology maintains the lightweight characteristics even at lower speeds. The study is extended to include a specific aerospace application, and three possible motor-fan integrations are presented.

While the benefit in specific power density is highlighted, the proposed slotless, cantilevered rotor topology is sensitive to manufacturing tolerances. Particularly, the low reactance of the motor and the slotless structure con-

tributes to the increase in circulating current in the armature coils. The aforementioned analytical model is used to predict the imbalance in back-EMF and thus the circulating current due to the manufacturing tolerances, and a low-field rotor is constructed to verify the prediction. The experimental measurements point to shortcomings of the rotor eccentricity model in predicting the circulating current in the coils. The relationships between manufacturing tolerances in coils and circulating current are highlighted.

*To all the special people in my life who have helped me
through my life's transients*

ACKNOWLEDGMENTS

First and foremost, I would like to express my sincere gratitude to my advisor, Dr. Kiruba Haran, for his guidance, support, and encouragement. I am inspired by his practical and creative approach to tackling engineering problems. I feel privileged for having had the opportunity to work with him. I would also like to thank the rest of my doctoral committee for their valuable insights and support.

I would like to thank all the fellow students in the Power and Energy Systems group at Illinois. The lifelong comradery that exists in the group is unique and incredible, and I am grateful to have been a part of it.

Lastly, I would like to thank the Grainger Center for Electric Machinery and Electromechanics, the Power Optimization of Electro-Thermal Systems Engineering Research Center, and the National Aeronautics and Space Administration for their financial support.

TABLE OF CONTENTS

| | | |
|------------|---|----|
| CHAPTER 1 | INTRODUCTION | 1 |
| 1.1 | Summary of work accomplished | 4 |
| CHAPTER 2 | POWER DENSITY | 6 |
| CHAPTER 3 | 1 MW, HIGH-FREQUENCY, SLOTLESS, PERMANENT MAGNET SYNCHRONOUS MOTOR | 12 |
| CHAPTER 4 | MODELING OF A SLOTLESS PERMANENT MAGNET SYNCHRONOUS MOTOR | 20 |
| 4.1 | Air gap field and torque computation | 20 |
| 4.2 | Losses | 30 |
| CHAPTER 5 | CASE STUDIES | 37 |
| 5.1 | Toothed topology vs. slotless topology | 37 |
| 5.2 | STARC-ABL | 41 |
| CHAPTER 6 | EFFECTS OF MANUFACTURING TOLERANCES ON CIRCULATING CURRENT | 55 |
| 6.1 | Analytical model | 57 |
| 6.2 | Analytical results and comparison | 61 |
| 6.3 | Experimental validation with low-field rotor | 68 |
| CHAPTER 7 | CONCLUSION | 80 |
| REFERENCES | | 82 |

CHAPTER 1

INTRODUCTION

According to the Vision 2050 report by the International Air Transportation Association (IATA), a fourfold increase in number of air passengers and a tenfold increase in amount of goods transported by air are projected by 2050, compared to the 2010 data [1]. The European Commission has estimated a 700% increase in aircraft emissions by 2050, compared to the 2005 data [2]. The resulting financial implications due to the cost of jet fuel and environmental concerns due to aviation emissions are instigating a general interest in reducing the thrust-specific fuel consumption and energy consumption of aircraft.

Initial steps toward reducing economic and environmental impact have been taken with the development of more electric aircraft (MEA) [3,4]. In these aircraft, most non-propulsive components, such as hydraulic, pneumatic, and mechanical systems, are replaced with electrical systems. Although the demonstrated benefit of MEA is impressive, typically over 90% of fuel is used for propulsion. Thus, a more significant reduction of specific fuel consumption and energy consumption of aircraft can be achieved by an electric propulsion system [5].

Equivalent concerns have caused much progress to be made for automotive, locomotive, and marine vehicles. In each case, significant reductions in fuel use and/or emissions have been demonstrated [6,7]. While fully electric large transonic aircraft are still considered infeasible due to immature energy storage technologies [8], turboelectric concept studies are showing promising benefits [9]. In a turboelectric aircraft power system, electric generators convert turbine engine power into electricity, which is used to drive the electric fans for propulsion. Studies have shown that this drive architecture allows reduction of fuel consumption from the drive perspective. Furthermore, the ease of routing electricity, compared to routing jet fuel, allows distributed propulsion, which provides an additional reduction of fuel consumption from

an aerodynamic perspective [10]. Distributed propulsion enables aircraft designs that include propulsion-airframe integration that was considered impractical with traditional turbofan engines. For example, Boeing’s partnership with the National Aeronautics and Space Administration (NASA) on Subsonic Ultra Green Aircraft Research (SUGAR) has brought about a concept aircraft based on a 85 to 215 passenger Boeing 737, as shown in Fig. 1.1 [11]. This aircraft has the potential to reduce energy use by 53% and NOx emission by 77-87%. NASA N3-X, based on a 400-passenger Boeing 777, has the potential to reduce energy use by 63% and NOx emission by 90% for a given mission [12].



Figure 1.1: Advanced turbo electric concept studies. Boeing SUGAR (left) and NASA N3-X (right).

While electric machines have been thought to reach the threshold of performance and reliability for industrial applications, the emergence of electric propulsion now imposes a new set of more stringent performance requirements. More specifically, high specific power (power per unit mass) is required for generators and motors. The specific power of general-purpose industrial motors is in the range of 0.1 - 0.5 kW/kg. The automotive industry utilizes drive motors with specific power in the range of 1 - 3 kW/kg [13]. The impact of electric drive specific power on turboelectric aircraft performance is shown in Fig. 1.2 [14]. In the figure, break-even specific power and efficiency lines are shown with three assumed key performance parameter benefits. These key performance parameter benefits include enhanced aerodynamic and propulsion efficiency from the configuration change. For example, with a medium-level benefit assumption, the minimum required motor drive specific power should be 5 kW/kg if the system is 100% efficient and the minimum required efficiency is 90% at a specific power of 15 kW/kg. The area above each line corresponds to fuel savings.

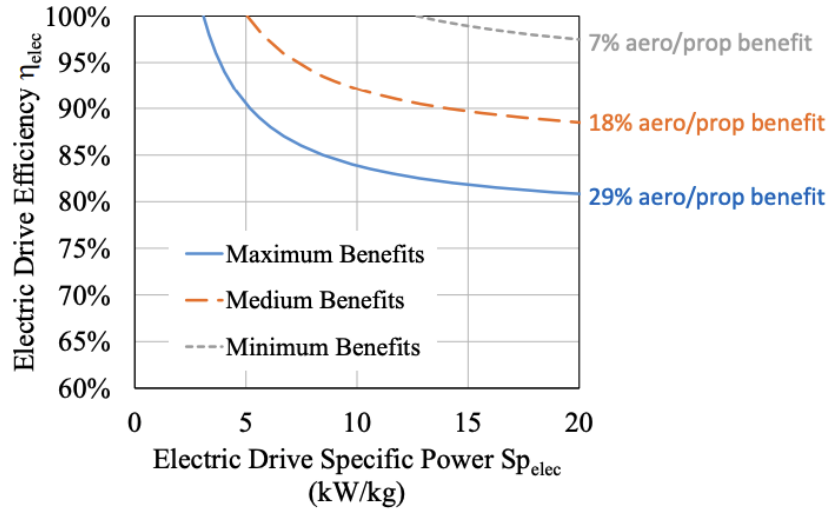


Figure 1.2: Key performance parameter break-even curves for a range of benefits [14].

Based on these findings, NASA has developed a technology roadmap for enabling technologies. Fig. 1.3 shows the roadmap for non-cryogenic electric machines. Today, the state of the art is by Siemens with a specific power of 5.2 kW/kg at a rated power of 260 kW [15]. The key milestone for developing concept airplanes calls for a megawatt-class motor that has a specific power of 13 kW/kg.

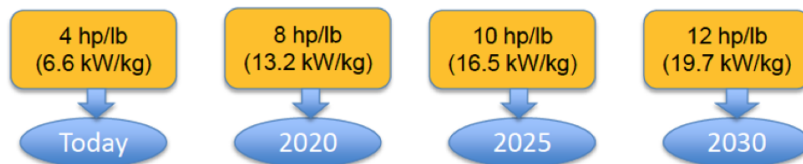


Figure 1.3: NASA technology roadmap [16].

Weight-sensitive applications like aircraft motors and generators typically achieve high specific power through aggressive cooling and high speed. In the adjacent field of power electronics, a major trend in recent years has been to increase switching frequency, especially with the advent of wide bandgap devices, to reduce requirements on the passive energy buffer components [17–19]. Interestingly, both efficiency and power density have improved in this period. Similar advances have been made in high-frequency transformers [20]. In a power-electronic-fed motor drive, the electromagnetic components of the motor are analogous in some senses to the inductors which

have been minimized in the drives. This dissertation explores the opportunity for improvements in electrical machines following a similar approach.

Chapter 2 discusses, starting from a classical machine sizing equation, how the adoption of high fundamental frequency for electric machines can be beneficial in increasing specific power. Chapter 3 discusses additional approaches taken to develop a 1 MW permanent magnet synchronous motor that meets the specification solicited by NASA. Key specifications and features are discussed. In Chapter 4, analytical models that describe the 1 MW motor topology are discussed, including air gap field and torque calculation, as well as copper, iron, and windage losses. Validations of the models are also presented. In Chapter 5, the developed analytical models are used to compare toothed and slotless topologies, and the scalability of the high-frequency, slotless topology is explored. The key risk (circulating current) of the motor's topology is detailed in Chapter 6, with results from a low-field spin test. Finally, the conclusion is presented in Chapter 7.

1.1 Summary of work accomplished

This section summarizes the design effort of high-frequency electric machines that includes the following work completed.

- In [21], design choices for a high-frequency, high-tip-speed, 1 MW machine are detailed. Reasons for adopting an air core, outer rotor, air gap wound topology are presented. Initial optimization of copper, magnet, and stator yoke radial dimensions is presented. The initial design parameters are included, along with projected losses and weight.
- Ref. [22] improves on initial optimization of [21] by including first-order thermal and mechanical effects to perform a multi-physics optimization. Several machine design parameters and their effects on machine performance and weight are presented.
- In [23], copper losses in a slotless machine with Litz coils have been investigated. Analytical models for ac and dc losses are presented and validated via finite element analysis and indirect balanced calorimetry test.

- Ref. [24] provides challenges in mechanical design of the motor design due to high tip speeds and outer-rotor configurations. Mechanical risks such as rotor expansion and vibration are identified, analytically calculated, and validated using a non-magnetic rotor. An analytical model for windage losses has been presented and compared to the results of the spin test.
- Ref. [25] presents how the high-frequency design scales to a concept aircraft by NASA using developed analytical models. The results show that low-weight characteristics are maintained at lower speeds. Further design analyses are performed in [26].
- Ref. [27] investigates the impact of rotor eccentricity on imbalance of back-EMF and thus circulating current. A model for rotor eccentricity is developed and ways to estimate back-EMF magnitude and phase shift are investigated. In [28], the models are compared with experimental values to show that the model is valid for predicting eccentricity based on back-EMF magnitude measurements.

CHAPTER 2

POWER DENSITY

Electrical machine design is a complex trade-off of electromagnetics, thermal, and mechanical considerations. Today, a multi-physics model embedded within an optimization scheme may be required to maximize specific power. However, with appropriate approximations and high-level assumptions, it may be useful to get an intuitive understanding of general trends. We use this approach to assess the potential for high-frequency machines.

Numerous electrical machine topologies abound, and several iterations and combinations of them are being explored by researchers [4, 29, 30]. The focus of this chapter is on applications requiring high specific power, so we start with key parameters of interest and whether they lead to some topologies being favored.

The well-known expression for motor power in terms of air gap shear stress, which is obtained from torque produced in the air gap multiplied by angular velocity, is shown as

$$\text{Power} = k_\omega A_{peak} B_{peak} n V_r, \quad (2.1)$$

where k_ω , A , B , n , and V_r represent winding factor, electrical loading, magnetic loading, angular speed, and rotor volume, respectively. The electrical loading is defined as the linear (sheet) current density around the airgap circumference as

$$A = (1 - \tau) d_{cu} J_{slot}, \quad (2.2)$$

where d_{cu} and J_{slot} refer to copper radial depth and slot current density, respectively. τ refers to the tooth width to tooth pitch ratio, which is typically 0.5 for electric machines. The magnetic loading is defined as flux density over the rotor surface. In a toothed machine, the flux density in the teeth is limited to about 1.6 T (saturation flux density of typical iron alloy) to

manage iron losses. Coupled with a typical value of τ , air gap flux density is then typically limited to $B_{ag} \approx \tau B_{teeth} = 0.8T$. Note that electric loading is typically referred to with rms values and magnetic loading is typically referred to with average flux density values, but defined with peak values in this case. The product of electric loading and magnetic loading is related to air gap shear stress, σ , as

$$\sigma = \frac{1}{2} k_{\omega} A_{peak} B_{peak}. \quad (2.3)$$

Air gap shear stress refers to the tangential force per unit of swept rotor surface area. Thus, torque per rotor volume is given as 2σ . Typical values of torque per rotor volume and air gap shear stress are given in Table 2.1. Small totally enclosed motors rarely have fans and are cooled entirely on conduction. With low-performance ferrite magnets, these motors are characterized by the lowest TRV. As higher performance magnets are utilized (higher magnetic loading), TRV can be increased even for totally enclosed motors. Higher values for TRV can be observed for forced-air cooling through external fan, and the highest values are observed for liquid-cooled machines. These machines achieve high TRV by pushing electric loading.

Table 2.1: Typical values for TRV and σ [31]

| Class of machine | TRV [kNm/m ³] | σ [lbf/in ²] |
|---|---------------------------|---------------------------------|
| Small totally enclosed motors (Ferrite magnets) | 7 - 14 | 0.5 - 1 |
| Totally enclosed motors (Rare Earth magnets) | 14 - 42 | 1 - 3 |
| Totally enclosed motors (Bonded NdFeB magnets) | 20 | 1.5 |
| Integral-hp industrial motors | 7 - 30 | 0.5 - 2 |
| High-performance servomotors | 15 - 50 | 2 - 4 |
| Aerospace machines | 30 - 75 | 2 - 5 |
| Large liquid-cooled machines (e.g. turbogenerators) | 100 - 250 | 7 - 18 |

To find the power density relationship, we define λ as

$$\begin{aligned} \lambda_1 &= \frac{D_{ag}}{D_o}, \\ \lambda_2 &= \frac{D_i}{D_{ag}}, \end{aligned} \quad (2.4)$$

where D_{ag} , D_o , and D_i refer to air gap diameter, machine outer diameter, and machine inner diameter, respectively [32]. Note that both λ_1 and λ_2

may approach zero for low pole count machines, and one for high pole count machines. Total enclosed volume of the machine can be expressed in terms of λ_1 as

$$V_{enclosed} = \frac{\pi D_{ag}^2 L_{stk}}{4\lambda_1^2}, \quad (2.5)$$

and thus power density can be shown as

$$\text{Power Density} = 4k_{\omega} A_{peak} B_{peak} \lambda_1^2 n. \quad (2.6)$$

Equation (2.6) points to the usual emphasis on cooling to maximize electrical loading and better magnetic materials to maximize magnetic loading. Table 2.2 shows types of cooling techniques and corresponding typical current density [33–35]. These current density values assume that the windings have appropriate heat transfer mechanisms. In typical air cooled machines, the fan is mounted outside the frame which focuses air outside of the motor. Liquid cooled machines typically have a channel around the outside of the stator with a cooling fluid circulating to remove the heat. Note that electrical loading can be said to be proportional to current density assuming that the radial depth of armature coils is constant. The table shows that liquid convection is more efficient for heat extraction than air convection and allows higher electric loading. This is because liquid has higher density and specific heat than air. Typically, small industrial motors utilize forced air cooling or conduction for its simplicity in implementation. However, for larger machines (larger than 100 kW), liquid cooling is common to manage the heat load from the high electromagnetic forces required. The auxiliary weight that the cooling mechanism adds to the motor weight must be considered.

Magnetic loading, or peak air gap flux density, is typically limited to 1 T due to ferromagnetic materials or magnets. Machines that utilize permanent magnet (surface permanent magnet or interior permanent magnet) are typically characterized by high magnetic loading that is close to 1 T. Other types of machines such as induction machines are characterized by lower magnetic loading. In these machines, magnetic loading can be maximized by reducing the magnetic path.

The equation also shows that power density is maximized for maximum λ_1 . Note that λ_1 can be maximized by reducing the yoke depth through high pole count and optimization of slot depth without reducing electrical

Table 2.2: Force convection cooling techniques and corresponding typical current density

| Method | Max J [A/mm ²] |
|----------------|----------------------------|
| Forced air | 5 - 12 |
| Indirect water | 10 - 15 |
| Indirect oil | 10 - 15 |
| Liquid bath | up to 25 |
| Direct liquid | up to 30 |
| Oil spray | over 28 |

loading. A direct way to increase power density for conventional machines is to maximize the speed. Due to rotor dynamics, structural integrity of the rotor, and windage losses, practical limits in many applications limit the rotor tip speed to 80-90% of the speed of sound [36]. In terms of tip speed, v , an alternate form of (2.1) can be realized as

$$\text{Power} = \frac{\pi}{4} k_{\omega} A_{peak} B_{peak} v D_{ag} L_{stk}. \quad (2.7)$$

Under the assumption that air gap diameter and stack length are of the same order for conventional industrial machines, we can establish that weight is proportional to D_{ag}^3 while power grows with D_{ag}^2 . This relationship assumes that tip speed is kept constant, so that angular speed has to increase with increasing diameter. Thus, power density of conventional designs can be said to be proportional to $1/\sqrt{\text{power}}$, assuming that tip speed is at a maximum limit. Note that for very large machines such as hydroturbines, iron is confined to the rim and weight can be said to be proportional to D_{ag} . However, these machines are typically characterized by very low tip speed and thus low power density (or specific power).

A survey of machines shows that many follow this relationship, as shown in Fig. 2.1 [13]. The survey includes a wide range of machines. The surveyed topologies include radial flux permanent magnet machines, axial flux permanent magnet machines, induction machines, switched reluctance machines, and wound-field synchronous machines and are denoted by RFPM, AFPM, IM, SRM, and WFSM, respectively. Superconducting machine (SCM) is also shown for comparison. The figure shows higher specific power at lower power rating, and lower specific power at higher power rating, with the exception of outliers. One of them is an oil cooled WFSM developed to be a genera-

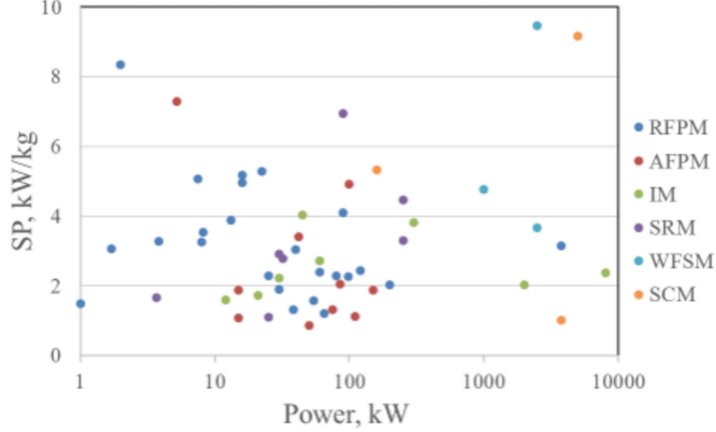


Figure 2.1: Distribution of specific power vs. rated power.

tor attached to the Rolls Royce T406 turboshaft engine [37]. The machine achieves high specific power by pushing very high current density with oil spray cooling. While the specific power presented here seems high, it should be noted that the presented data is for peak power with intermittent operation. The other data point with high specific power is a superconducting machine. These machines achieve high specific power through very high air gap flux densities (up to 7 T).

To see what factors affect the specific power of a high-frequency machine, we first express volume of active materials as

$$\begin{aligned}
 V_{act} &= \frac{\pi}{4} (D_o^2 - D_i^2) L_{stk} \\
 &= \frac{\pi}{4} \left(\frac{1}{\lambda_1^2} - \lambda_2^2 \right) D_{ag}^2 L_{stk}.
 \end{aligned} \tag{2.8}$$

Power density, in terms of power per volume of active materials, can be expressed as

$$\text{Power Density}_{act} = \frac{2k_\omega A_{peak} B_{peak} n}{\frac{1}{\lambda_1^2} - \lambda_2^2}. \tag{2.9}$$

For high-frequency machines, rotor radial dimension, d_r , and stator radial dimension, d_s , can be much less than that of the air gap diameter. Thus, the

denominator of power density in (2.9) can be expressed as

$$\begin{aligned} \frac{1}{\lambda_1^2} - \lambda_2^2 &= \left(\frac{D_o + D_i}{D_{ag}} \right) \left(\frac{D_o - D_i}{D_{ag}} \right), \\ &\approx 4 \frac{d_s + d_r}{D_{ag}}, \end{aligned} \quad (2.10)$$

and power density of high-frequency machines can be expressed as

$$Power\ Density_{act} \approx \frac{4k_\omega A_{peak} B_{peak} v}{(d_s + d_r)}. \quad (2.11)$$

The weights of steel, coils (copper and insulation), and magnets are of the same order, so the above expression can be said to be proportional to specific power (power-to-weight ratio). Note that for a more accurate representation of specific power, auxiliary components such as structure and cooling infrastructure must be taken into account. From (2.11), it can be said that specific power is then proportional to $freq^i$ where $1 < i < 2$. While speed and cooling are generally the parameters used for designing conventional electric machines, closer examination shows significant specific power improvement is possible through the adoption of high frequency and high tip speed. Unlike conventional machines, these machines have specific power that scales well with power and speed, as long as high tip speed is achieved. However, adoption of high fundamental frequency and high tip speed results in many challenges. Chapter 3 explores approaches to accommodate high fundamental frequency and high tip speed, along with additional approaches to reduce heavy iron alloy in a machine while maintaining high electric and magnetic loading.

CHAPTER 3

1 MW, HIGH-FREQUENCY, SLOTLESS, PERMANENT MAGNET SYNCHRONOUS MOTOR

While adoption of high fundamental frequency seems beneficial in reducing the magnetic circuit of the motor, leading to a more air core topology, several factors need to be considered. Losses in magnetic core are determined by the peak flux density in the core and frequency of the time-varying flux density. While flux density in the yoke can be controlled by adjusting the thickness of the yoke to mitigate iron losses at high frequency, flux density in the teeth is not governed by frequency or number of poles. Consequently, stator teeth are typically characterized to have the highest levels of iron losses in a motor. However, stator teeth can be eliminated for a slotless topology, as illustrated in Fig. 3.1. In toothed topology, the magnetic circuit is defined by the stator teeth and the coils experience minimal external magnetic field. However, the elimination of teeth and the resulting slotless topology cause the armature coils to experience the full air gap field. The resulting effect on ac losses can be mitigated by using Litz wires to form armature coils. Litz wire consists of compacted film-insulated wires or groups of compacted film-insulated wires twisted and compressed into a rectangular profile with outer insulation. This is also attractive for manufacturing purposes. These Litz wires can be manufactured into a rectangular profile, making it easier to manufacturing form-wound coils.

To further reduce the amount of iron, a Halbach array can be used to form the field magnets. In conventional surface permanent magnet machines, field magnets are oriented radially, requiring a back iron to conduct magnetic flux. Alternatively, the magnets can be arranged to have a spatially rotating pattern of magnetization. When the magnets are arranged in such a way, magnetic field is augmented on one side of the array, while cancelling the field to near zero on the other side [38]. This is illustrated in Fig. 3.2. The left illustration shows the field from magnets that are magnetized pointing up or down, to represent radially magnetized field magnets. In this case, magnetic

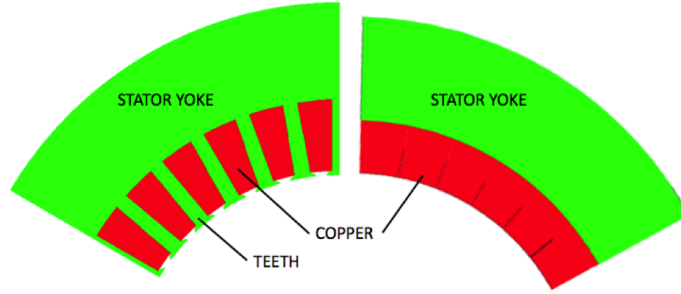


Figure 3.1: Illustration comparing the toothed topology (left) and slotless topology (right).

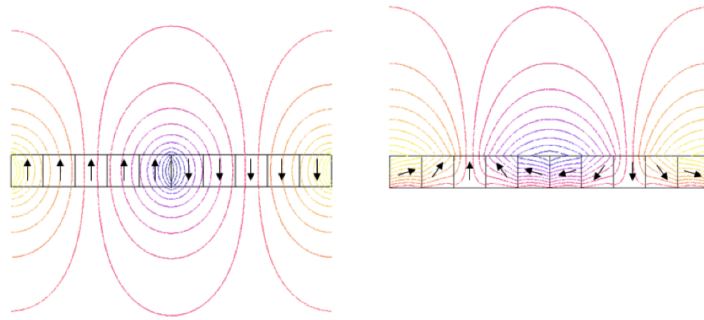


Figure 3.2: Illustration demonstrating field cancellation of Halbach arrayed magnets. Conventional radially oriented field magnets (left). Halbach arrayed magnets (right).

yoke needs to be included in the non-air gap side to reduce the reluctance. However, from the right illustration, the effect of field containment within the magnets is observed.

Another approach to attain high specific power is to design for a high rotor tipspeed, as shown in (2.11). Surface permanent magnet machines employ a retaining ring to restrain the field magnets. Typically, rotor tipspeeds of these machines are relatively low, requiring only a modest thickness of the retaining ring. Coupled with toothed laminations, magnetic loading is minimally affected by the retaining ring for these machines. However, to accommodate a high rotor tipspeed, a retaining ring of substantial thickness needs to be employed. For the proposed slotless topology, an inner rotor can be disadvantageous because the resulting electromagnetic gap can be very large. However, if the rotor can be placed outside of the stator, a minimum distance between the coils and the magnets can be kept, even with a retaining ring. Fig. 3.3 illustrates the benefit of an outer rotor topology.

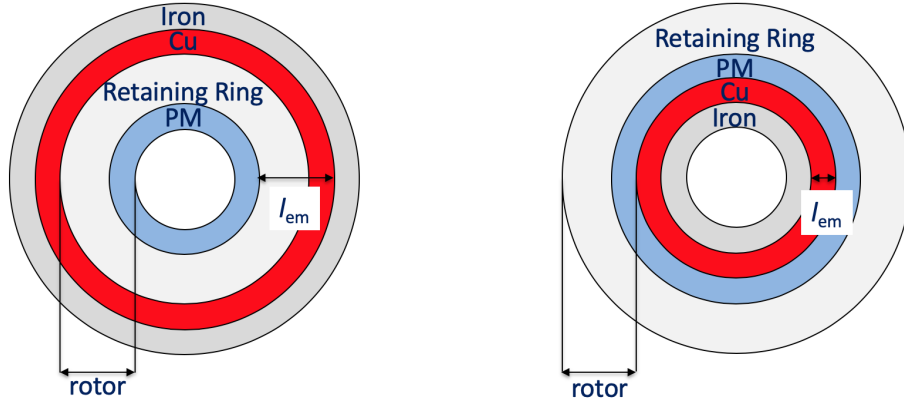


Figure 3.3: Illustration comparing inner and outer rotor topology. Inner rotor topology with slotless configuration is characterized by a large electromagnetic air gap, l_{em} (left). Outer rotor topology minimizes electromagnetic air gap while accommodating a thick retaining ring (right).

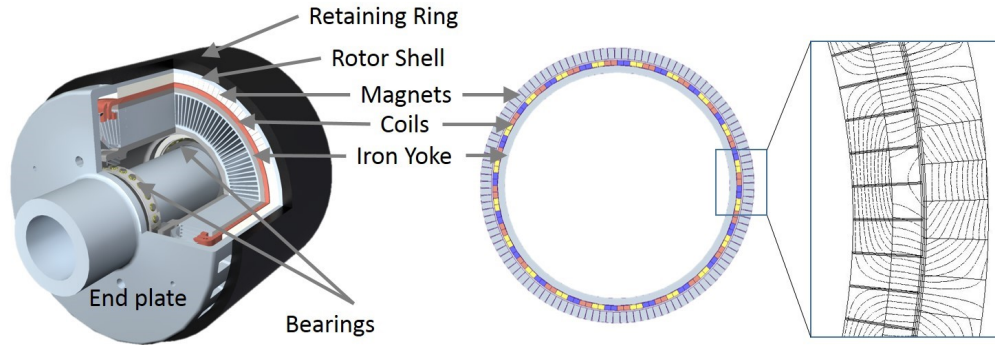


Figure 3.4: CAD representation of the full motor (left) and 2D cross-section showing active materials and field lines (right).

The resulting design of the 1 MW motor is shown in Fig. 3.4 (left), and the radial dimensions of the motor are shown in Fig. 3.5. The retaining ring, rotor shell, and the magnets compose the rotor. Litz armature coils, iron yoke, and the aluminum heat sink compose the stator. The rotor shell allows a cantilevered assembly between the rotor and the stator via two bearings. Shown in Fig. 3.4 (right) are active materials for this motor. Compared to the traditional, metal core topology, this air core topology demonstrates a very thin radial build of active materials. As a result, the topology leaves much room for aggressive cooling. In fact, the cooling method of the 1 MW motor is implemented by a centrifugal fan mounted on the rotor. When the rotor spins, air is pumped through the machine, pulling in air from the free end of the cantilevered structure, as shown in Fig. 3.6. In fact, while other

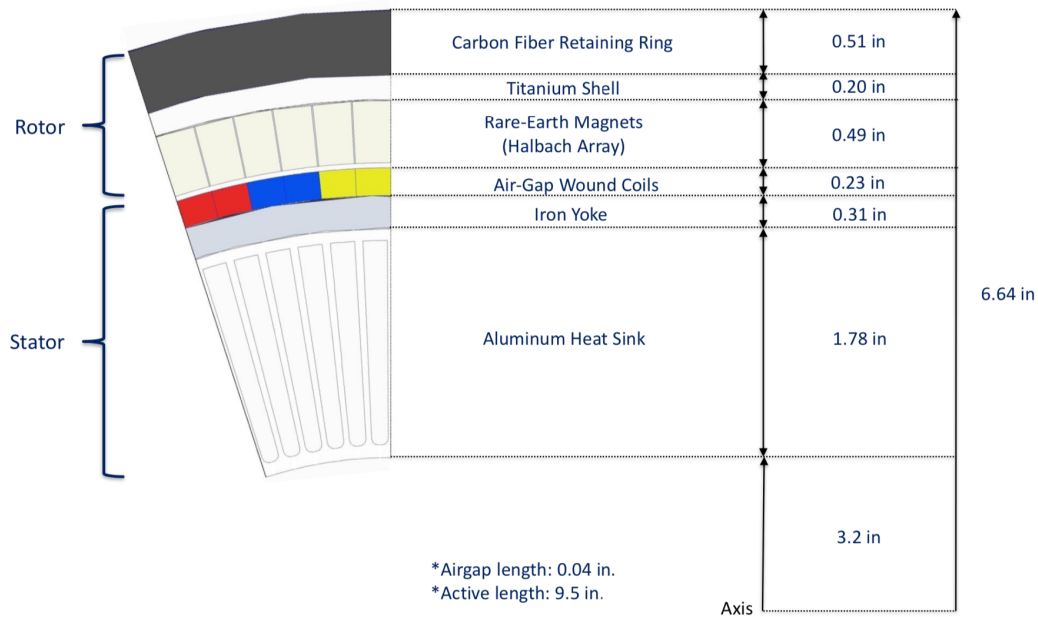


Figure 3.5: Radial dimension of the 1 MW motor.

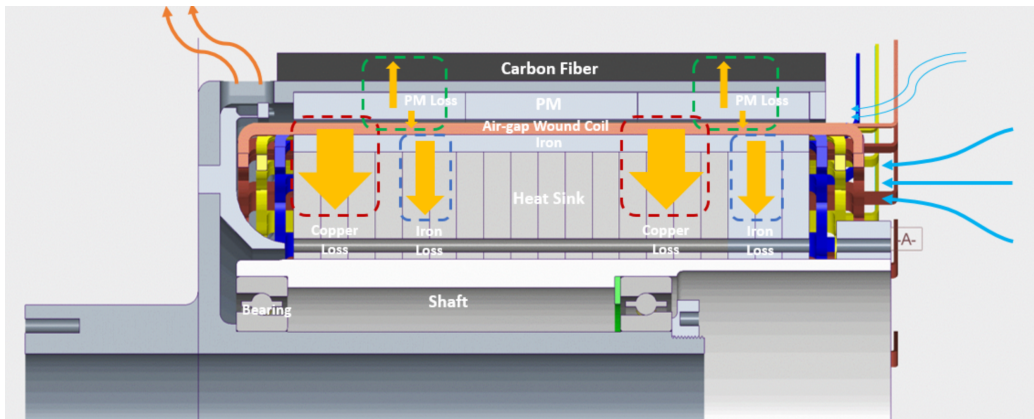


Figure 3.6: Heat flow path for 1 MW motor. Cool air (denoted by blue arrows) is sucked in from the free end (right side of the figure), and blown out radially (left side of the figure).

motors with similar levels of electrical loading utilize liquid cooling that adds significant auxiliary weight, this topology is able to achieve effective thermal management through simple forced-air cooling. The fan blades were designed with a target airflow speed of 20 m/s in the heat exchanger, and the air flow was validated with a rotor spin test [39]. Armature coils are precast using ceramic filled resin to further improve thermal performance of the copper. To improve manufacturing and assembly qualities of the coils, coils of each

phase are staggered with respect to coils of another phase. The resulting coils have different end-winding length between the phases, but can easily be addressed with appropriate drive control. Key metrics of the 1 MW motor are summarized in Table. 3.1.

Table 3.1: Key metrics

| | | |
|-----------------------|--------|-------|
| Rated Power | 1 | MW |
| Rated Torque | 665 | Nm |
| Rated Efficiency | 97.4 | % |
| Stator Weight | 34.4 | kg |
| Rotor Weight | 42 | kg |
| Specific Power | 13 | kW/kg |
| Nominal Speed | 15,000 | rpm |
| Tip Speed | 270.3 | m/s |
| Cooling, Forced air | 20 | m/s |
| Number of Poles | 20 | - |
| Synchronous reactance | 0.06 | p.u. |
| Insulation Class | H | - |

Table 3.2: Key metric comparison

| - | Best in Class | Illinois |
|---|-----------------------|--------------------|
| Copper current density [A/mm ²] | 30 (liquid cooled) | 18 (air cooled) |
| Electric loading [kA/m] | 50 | 39 |
| Air gap flux density [T] | 1 | 0.95 |
| Shear stress [kPa] | 20-35 | 23.6 |
| Rotor tip speed [m/s] | 300 | 270.3 |

While the motor is projected to achieve a very high specific power of 13 kW/kg, comparison of key design metrics with “best in class” values can provide more insight, as shown in Table 3.2 [40–43]. The highest copper current available in literature was about 30 A/mm². For air cooled machines, typical values range 5-12 A/mm² [33]. Compared to that value, the Illinois motor shows a higher current density. While this usually presents challenges in thermal management, a narrow radial depth of the copper region allows for manageable electric loading, and thus heat flux. Note that the electric loading does not exceed the best-in-class value. The table also shows that the Illinois motor is pushing the air gap flux density to its limits. While the large magnetic gap due to slotless topology typically makes achieving high air gap

flux density a challenge, the Halbach array overcomes the high reluctance. The table clearly shows that the achievement of high specific power is a result of pushing the metrics simultaneously, along with significant elimination of heavy material compared to conventional designs.

Materials used for the design of the motor were carefully selected after a rigorous trade-off of weight and performance. Table 3.3 shows the material used for key parts of the motor. Carbon fiber is known to have high stiffness, high tensile strength, high temperature tolerance, low thermal expansion, and low weight, and thus was chosen for the retaining ring. The rotor shell not only plays a critical role in housing magnets, but also provides an interface between the stator and the rotor via the end plate. Titanium has the highest strength-to-density ratio among metallic elements, and has been chosen for the rotor shell. The fan is also titanium. Proper mechanical analyses and tests have been performed to ensure structural integrity (both static and dynamic) of these parts [44].

Typically, a material with high saturation flux density is utilized for the stator yoke for high-performance machines. For example, Vacoflux 50 is a cobalt-iron alloy which has saturation flux density of 2.1 T. Employing a material with high saturation flux density allows reduction in yoke thickness. While this was initially considered for the motor design, Permenorm 5000 V5 (nickel-iron alloy) is chosen for the stator yoke for the final design. While this material has a lower saturation flux density (1.5 T), the material is found to have lower iron losses. When a trade-off study was performed comparing Vacoflux 50 (2 mil lamination) and Permenorm 48 (4 mil lamination), the yoke made from Permenorm 5000 V5 is found to be heavier by 2.5 kg, but the iron loss reduction is observed from 2 kW to 1.1 kW, even with twice the lamination thickness.

Table 3.3: Material for key parts

| Part | Material |
|----------------|--------------------------|
| Retaining ring | IM7/PEEK Carbon fiber |
| Rotor shell | Ti.6_Al.4V Titanium |
| Fan | Ti.6_Al.4V Titanium |
| Heat sink | Aluminum 6061 |
| Stator yoke | NiFe (Permenorm 5000 V5) |
| Magnet | NdFeB (N45UH) |

Neodymium boron iron (NdFeB) magnets are popular among machine designers due to their high energy density. However, the hotspot temperature in magnets is found to reach 150 °C. At these temperatures, reduction in performance of the magnets as well as a risk of demagnetization has to be considered carefully. While NdFeB magnets excel at lower operating temperatures (120 °C), samarium cobalt (SmCo) displays more robustness under high temperature conditions. A comparison of N45UH (NdFeB) and Recoma 35E (SmCo) under rated machine load shows that while N45UH experiences 3.62% demagnetization at 150 °C, it is still able to supply the highest air gap flux density of 0.9 T. REcoma 35E is able to produce 0.81 T of flux density in the air gap. The magnet losses were found to be only 0.5% of the machine rating. This is due to another attractive feature of the motor where the slotless topology coupled with Halbach array creates a highly sinusoidal back-EMF waveform.

While the air gap flux density exhibits 13th harmonic from the spatial discretization of the Halbach array, the harmonics are quickly attenuated due to the large magnetic gap, as observed in Fig. 3.7. As a result, the motor has a sinusoidal back-EMF waveform, as shown in Fig. 3.8. Design and prototyping effort of this 1 MW motor included development effort of modular, multilevel inverters that have shown to be effective at minimizing total harmonic distortion (THD) [45]. This, coupled with a sinusoidal airgap field, allows the topology to have very low torque ripple.

Table 3.4: Loss breakdown

| | | |
|------------------------|-----|----|
| Iron losses | 1.1 | kW |
| Copper losses (dc) | 6.7 | kW |
| Copper losses (ac) | 2.0 | kW |
| PM eddy current losses | 0.5 | kW |
| Windage and fan losses | 11 | kW |
| Bearing loss | 0.2 | kW |
| Additional | 3 | kW |

Through analytical and empirical methods, coupled with a series of bench tests (discussed in the next chapter), losses for the 1 MW motor have been characterized and shown in Table 3.4. The three most dominant loss mechanisms for the machine are found to be iron, copper, and windage. While ac losses are typically of concern at high fundamental frequencies, proper

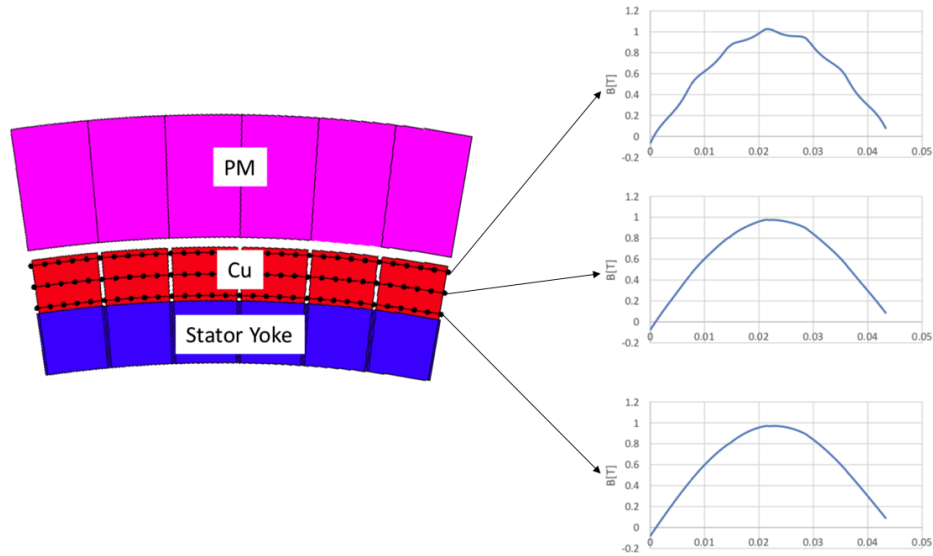


Figure 3.7: Air gap flux density profile obtained via FEA at different points along the radial dimension of the coil.

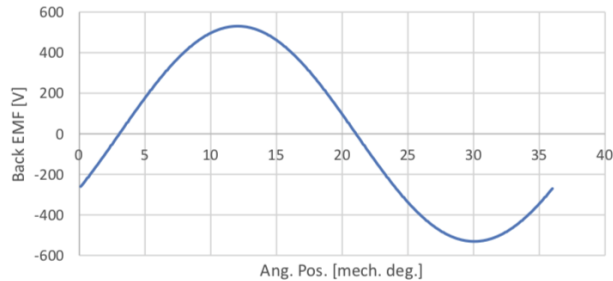


Figure 3.8: Back-EMF of the 1 MW motor. Magnitude corresponds to phase voltage magnitude.

selection of Litz wires results in ac loss that is manageable. Through the use of very thin laminations (0.05 mm) for the stator yoke, iron losses are also minimized. Total projected efficiency points to 97.4% for the motor. While the motor is optimized at 15000 rpm to be integrated within jet engines at high speed, the machine may be attractive in various applications at different power levels and speeds. Chapter 4 describes an analytical model that can quickly (compared to FEA) predict the electromagnetic performance of the topology, followed by analytical/empirical models for the major loss mechanisms for the topology. These models can prove to be very useful in quickly exploring the potential benefit of the topology for different applications.

CHAPTER 4

MODELING OF A SLOTLESS PERMANENT MAGNET SYNCHRONOUS MOTOR

An analytical model for the slotless, air core PMSM that has been developed to predict electromagnetic, thermal, and mechanical performance, is described in the following sections. A model for computing air gap field and torque has been developed and validated using bench tests. The loss models include the three most dominant loss mechanisms and also have been validated and calibrated with experiments and can serve as useful tools in quickly sizing machines of this topology. As one of the main fixed variable constraints for machine design is air gap heat flux, the losses are presented in the form of heat flux as well.

4.1 Air gap field and torque computation

4.1.1 Analytical model

While finite element method (FEM) provides accurate field distribution in the air gap, it is not suitable for comparative studies with dozens of cases due to its high computation time. In the case of conventional machines, characterized by small air gaps, magnetic equivalent circuit (MEC) models are often used. In the case of a slotless, air gap wound topology, simplified models such as MEC should be avoided because of the larger magnetic air gap and the resulting increase in air gap leakage. Thus, to calculate air gap field for a given geometry and the resulting torque, an analytical model (shown in Fig. 4.1) based on flux-potential transfer relations is used [46].

To obtain the model for air gap field due to magnets, we begin with

$$\mathbf{B}_n = \mu_o (\mathbf{H}_n + \mathbf{M}_n), \quad (4.1)$$

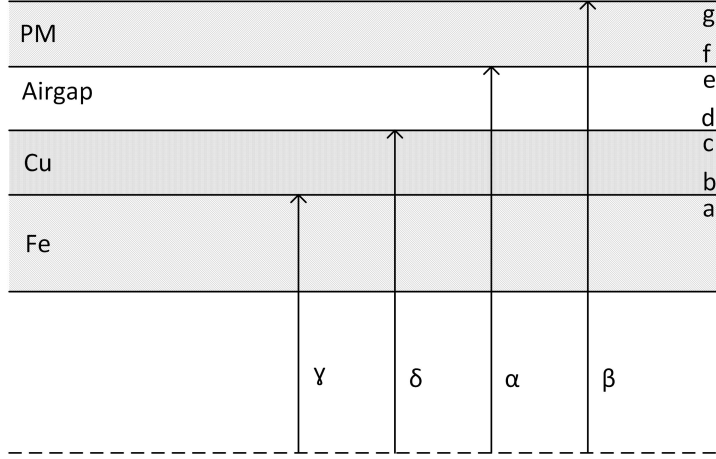


Figure 4.1: Analytical Model for toothless topology without rotor yoke.

where \mathbf{M} is the magnetization intensity vector. Applying curl on both sides, and given uniform μ_o ,

$$\nabla \times \mathbf{B}_n = \mu_o \nabla \times \mathbf{M}_n \quad (4.2)$$

can be established provided that the permanent magnet region is absent of free current such that Ampere's law gives $\nabla \times \mathbf{H}_n = 0$. Note that in machines, eddy currents exist in magnets leading to ohmic losses, but are neglected in this formulation. Expressing \mathbf{B}_n in terms of magnetic vector potential,

$$\begin{aligned} \nabla \times \mathbf{B}_n &= \nabla \times (\nabla \times \mathbf{A}_n) \\ &= \nabla (\nabla \cdot \mathbf{A}_n) - \nabla^2 \mathbf{A}_n. \end{aligned} \quad (4.3)$$

Using the Coulomb gauge condition, (4.2) and (4.3) can be combined to establish a Poisson equation,

$$\nabla^2 \mathbf{A}_n = -\mu_o \nabla \times \mathbf{M}_n, \quad (4.4)$$

where the subscript n denotes the harmonic number to account for a non-sinusoidal magnetization vector. Assuming a general form of \mathbf{A}_n and \mathbf{M}_n such that

$$\begin{aligned} \mathbf{A}_n &= \text{Re} [A_{z,n} e^{-jnp\theta}] \hat{\mathbf{z}} \\ \mathbf{M}_n &= [M_{r,n} e^{-jnp\theta} \hat{\mathbf{r}} + M_{\theta,n} e^{-jnp\theta} \hat{\boldsymbol{\theta}}], \end{aligned} \quad (4.5)$$

(4.4) can be solved as

$$\frac{\partial^2}{\partial r^2} A_{z,n} + \frac{1}{r} \frac{\partial}{\partial r} A_{z,n} - \left(\frac{np}{r}\right)^2 A_{z,n} = -j\mu_o \frac{np}{r} M_n, \quad (4.6)$$

where r , p and θ refer to radius, number of pole pairs, and angular position, respectively. $A_{z,n}$, $M_{r,n}$, and $M_{\theta,n}$ refer to magnitudes of magnetic vector potential, radial magnetization vector, and tangential magnetization vector, of the n^{th} harmonic. Variable M_n is calculated as $M_{r,n} + M_{\theta,n}/jnp$. Fig. 4.2 shows an example of radial and tangential magnetization magnitudes for a Halbach array.

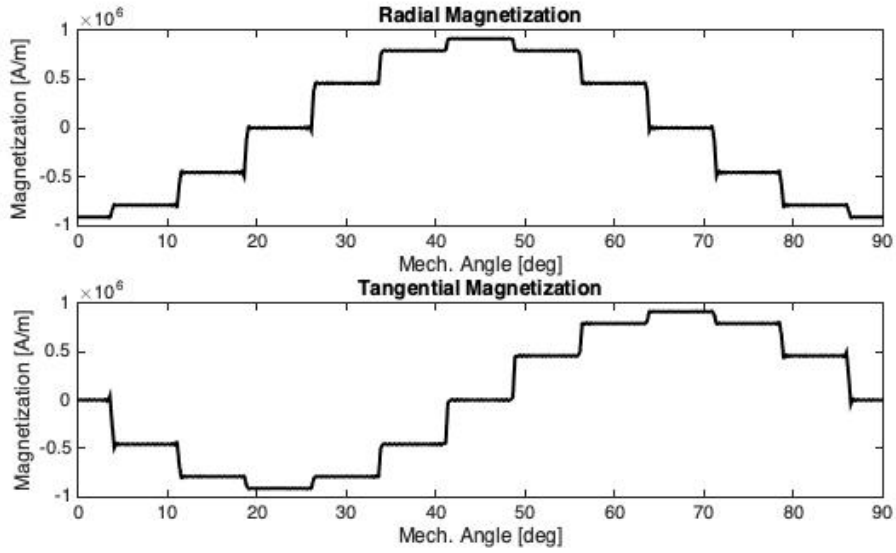


Figure 4.2: Radial magnetization, M_r , and tangential magnetization, M_θ , for one pole pair of an 8-pole rotor. The results here show the sum of 100 harmonic contents.

Upon finding homogeneous and particular solutions for (4.6), a general transfer relation between the magnetic vector potentials and the tangential flux densities at two different boundaries (e.g. boundaries denoted by f and g from Fig. 4.1) can be established as

$$\begin{bmatrix} B_{\theta n}^f \\ B_{\theta n}^g \end{bmatrix} = \begin{bmatrix} F_o(\beta, \alpha) & G_o(\alpha, \beta) \\ G_o(\beta, \alpha) & F_o(\alpha, \beta) \end{bmatrix} \begin{bmatrix} A_{z,n}^f \\ A_{z,n}^g \end{bmatrix} - M_s \begin{bmatrix} X_s \\ Y_s \end{bmatrix}, \quad (4.7)$$

where

$$\begin{aligned} M_s &= \frac{j\mu_o np M_n}{(np)^2 - 1}, \\ X_s &= \alpha F_o(\beta, \alpha) + \beta G_o(\alpha, \beta) + 1, \\ Y_s &= \alpha G_o(\beta, \alpha) + \beta F_o(\alpha, \beta) + 1, \end{aligned}$$

and F_0 and G_0 are characterized as

$$\begin{aligned} F_0(x, y) &= \frac{np \left[\left(\frac{x}{y}\right)^{np} + \left(\frac{y}{x}\right)^{np} \right]}{y \left[\left(\frac{x}{y}\right)^{np} - \left(\frac{y}{x}\right)^{np} \right]}, \\ G_0(x, y) &= \frac{2np}{x} \frac{1}{\left[\left(\frac{x}{y}\right)^{np} - \left(\frac{y}{x}\right)^{np} \right]}. \end{aligned}$$

Applying a boundary condition $H_\theta^e = H_\theta^f$ to (4.2) results in a transfer relation between boundaries e and h,

$$\begin{bmatrix} B_{\theta n}^e \\ B_{\theta n}^h \end{bmatrix} = \begin{bmatrix} F_o(\beta, \alpha) & G_o(\alpha, \beta) \\ G_o(\beta, \alpha) & F_o(\alpha, \beta) \end{bmatrix} \begin{bmatrix} A_{z,n}^e \\ A_{z,n}^h \end{bmatrix} + \begin{bmatrix} -\mu_o M_{\theta,n} - M_s X_s \\ -\mu_o M_{\theta,n} - M_s Y_s \end{bmatrix}. \quad (4.8)$$

Furthermore, noting that no magnetization source exists between boundaries b and e, the transfer relation can be shown as

$$\begin{bmatrix} B_{\theta n}^b \\ B_{\theta n}^e \end{bmatrix} = \begin{bmatrix} F_o(\alpha, \gamma) & G_o(\gamma, \alpha) \\ G_o(\alpha, \gamma) & F_o(\gamma, \alpha) \end{bmatrix} \begin{bmatrix} A_{z,n}^b \\ A_{z,n}^e \end{bmatrix}. \quad (4.9)$$

Then, combining (4.7), (4.8), and (4.9), with a boundary condition stating that $B_\theta^b = 0$, we can obtain B_θ^e and B_θ^h as

$$\begin{bmatrix} B_{\theta n}^e \\ B_{\theta n}^h \end{bmatrix} = \begin{bmatrix} 1 - \frac{F_o(\alpha, \gamma) F_o(\beta, \alpha)}{-G_o(\alpha, \gamma) G_o(\gamma, \alpha) + F_o(\gamma, \alpha) F_o(\alpha, \gamma)} & -\frac{\beta}{np} G_0(\alpha, \beta) \\ -\frac{F_o(\alpha, \gamma) G_o(\beta, \alpha)}{-G_o(\alpha, \gamma) G_o(\gamma, \alpha) + F_o(\gamma, \alpha) F_o(\alpha, \gamma)} & 1 - \frac{\beta}{np} F_0(\alpha, \beta) \end{bmatrix}^{-1} \quad (4.10)$$

$$\times \begin{bmatrix} -\mu_o M_{\theta,n} - M_s X_s \\ -\mu_o M_{\theta,n} - M_s Y_s \end{bmatrix}. \quad (4.11)$$

From these results, tangential flux densities at all boundaries can be com-

puted using the transfer relations. The radial component of the flux density can be obtained by computing the curl of the magnetic vector potential. Fig. 4.3 shows the flux density of the Halbach array using the described transfer relations. Note that the inactive side result shows the effectiveness of field cancellation.

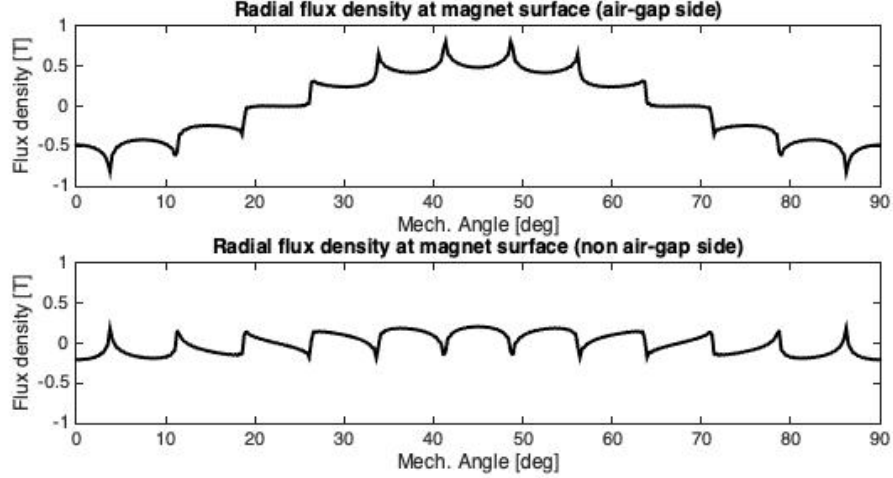


Figure 4.3: Magnetic flux density at Halbach array magnet surface. Air gap side (top), and inactive side (bottom).

To find the magnetic field due to the armature coils, we start with

$$\nabla \times \mathbf{H}_n = \mathbf{J}_{f,n} \quad (4.12)$$

and

$$\mathbf{B}_n = \mu_o \mathbf{H}_n, \quad (4.13)$$

where \mathbf{J}_f refers to free current. Applying curl on both sides, and then using the Coulomb gauge condition, we can establish a Poisson equation,

$$\nabla^2 \mathbf{A}_n = -\mu_o \mathbf{J}_{f,n}. \quad (4.14)$$

Thus the transfer relation between the magnetic vector potentials and the tangential flux densities at two different boundaries (e.g. boundaries denoted by b (with radius of γ) and c (with radius of δ)) due to the coils can be shown as

$$\begin{bmatrix} B_{\theta n}^b \\ B_{\theta n}^c \end{bmatrix} = \begin{bmatrix} F_o(\delta, \gamma) & G_o(\gamma, \delta) \\ G_o(\delta, \gamma) & F_o(\gamma, \delta) \end{bmatrix} \begin{bmatrix} A_{z,n}^b \\ A_{z,n}^c \end{bmatrix} - J_{fs} \begin{bmatrix} X_{fs} \\ Y_{fs} \end{bmatrix}, \quad (4.15)$$

where

$$J_{fs} = \frac{\mu_o J_{zn}}{(np)^2 - 1},$$

$$X_{fs} = \gamma F_o(\delta, \gamma) + \delta G_o(\gamma, \delta) + 1,$$

$$Y_{fs} = \gamma G_o(\delta, \gamma) + \delta F_o(\gamma, \delta) + 1.$$

Note that J_{zn} refers to magnitude of current density distribution of the n^{th} harmonic. Using the described method, magnetic fields generated by the

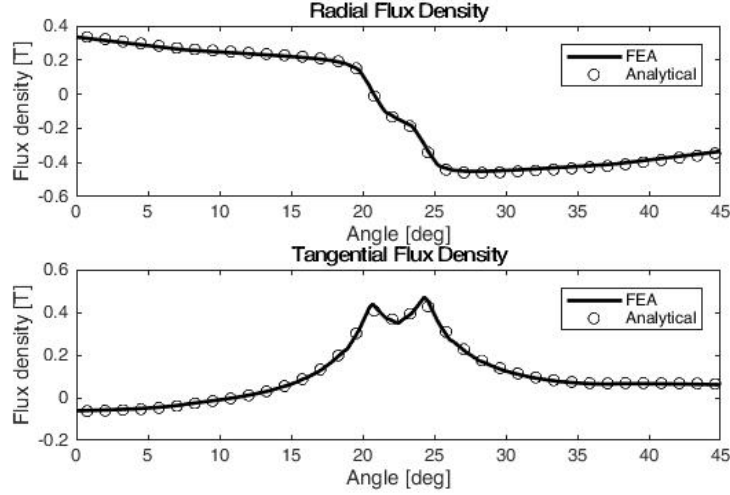


Figure 4.4: Air gap field comparison between FEA and analytical method of an 8-pole toothless motor.

permanent magnet can be computed at a certain boundary, and can be superposed with the calculated magnetic field generated by the copper coils at the same boundary to evaluate the Maxwell stress tensor. Then the torque can be calculated as

$$Torque = \frac{D_{ag} \pi D_{ag} L_{stk}}{4 \Delta\theta \mu_o p} \langle B_n B_\theta \rangle, \quad (4.16)$$

where $\Delta\theta$ accounts for the spatial discretization and p refers to the number of pole pairs. The model was tested at various pole counts and dimensions. Fig. 4.4 shows radial and tangential components of air gap flux density of an 8-pole slotless machine and shows good agreement with FEA. This model can be applied to an inner-rotor topology with boundaries and radii flipped.

4.1.2 Experimental validation

To validate the analytical model, field measurements from hardware builds were utilized. There were a total of two magnet assembly trials. The desired orientations of the magnets are shown in Fig. 4.5. In this case, the air gap flux density should be sinusoidal, as evidenced by Fig. 3.7.

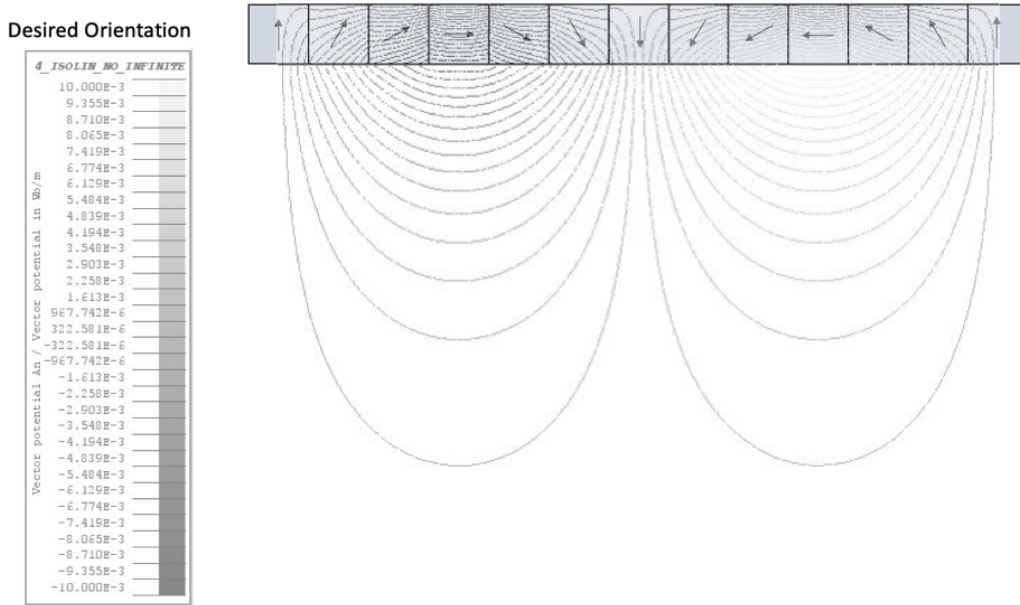
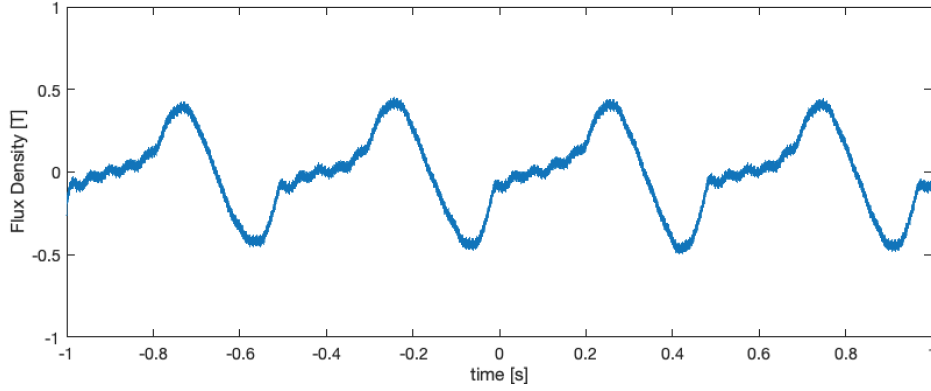


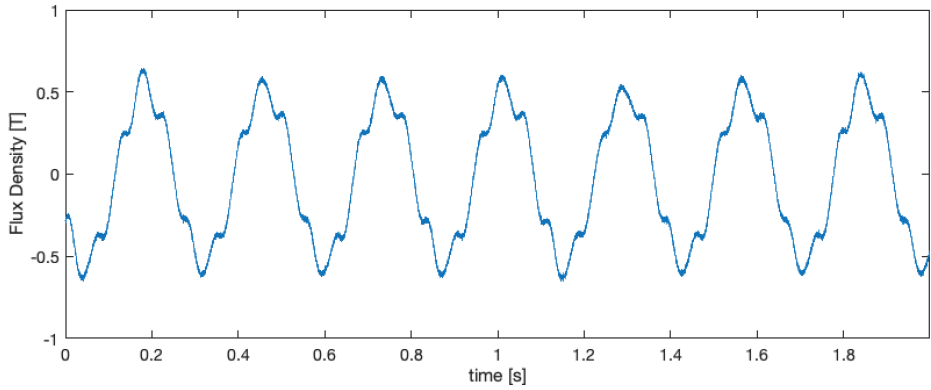
Figure 4.5: Desired orientation for the Halbach array with field lines. Each magnet is rotated 30° from the adjacent magnet piece.

However, upon receiving the rotor from the third party vendor and measuring magnetic field along the inner diameter of the two assembly trials, non-sinusoidal air gap fields were measured, as shown in Fig. 4.6. Note that periods of the two waveforms are different because measurements from the two assemblies were taken at different speeds. Both measurements show a periodic waveform. The field obtained from Assembly Trial I is characterized by an incomplete sine wave. The field obtained from Assembly Trial II is characterized by harmonics that create two additional peaks per half period. In either case, the fact that each magnet is non-uniformly magnetized with respect to the other magnets can be deduced from varying peaks of the waveforms. Based on the Gauss meter readings, suspected orientations for the two assembly trials are presented, as seen in Fig. 4.7 and Fig. 4.8, where misdirected magnets are represented with red arrows.

For Assembly Trial I, correctly oriented magnets are thought to cause the



(a) Flux density measured for Assembly Trial I.



(b) Flux density measured for Assembly Trial II.

Figure 4.6: Magnetic field measurements along the inner diameter of the rotor using a Gauss meter.

sinusoidal portion of the measured field. However, half of the magnets in the array no longer augment the field on the air gap side. Instead, those magnets are oriented to augment the field on the other side. In fact, the same flux density profile is observed along the outer diameter of the rotor. For this orientation, the radial magnetization vector is identical to the correct case, but the tangential magnetization vector has to be modified.

For Assembly Trial II, all magnets are suspected to augment the field on the correct side (air gap side). However, additional peaks observed in Fig. 4.6 are attributed to a consistent switch between the two adjacent magnets. In this case, both radial and tangential magnetization vectors need to be modified.

With the non-Halbach vectors for both assembly trials, the results from the analytical model can be compared against the measured field. Results are shown in Fig. 4.9. In both cases, the experimental measurements are

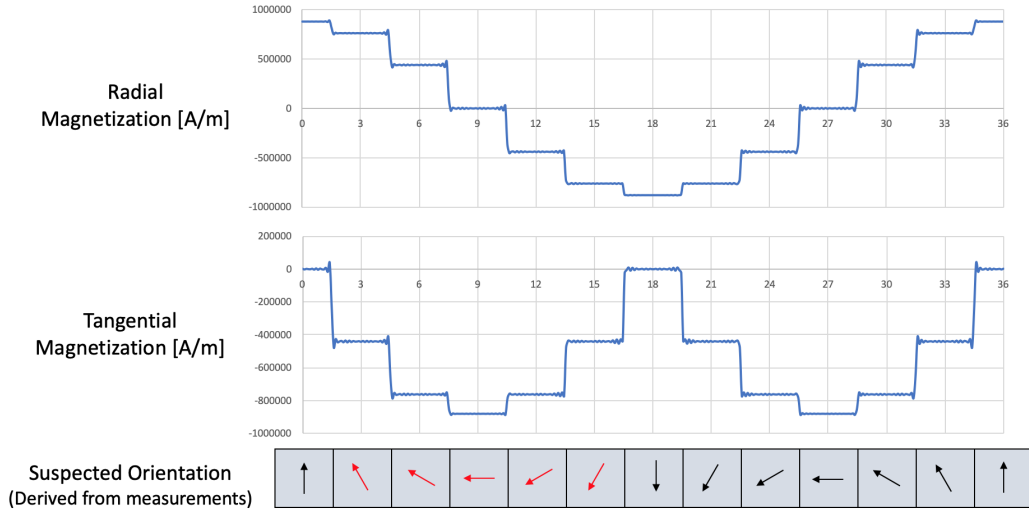


Figure 4.7: Suspected orientation based on Gauss meter measurements and corresponding magnetization vector (Assembly Trial I).

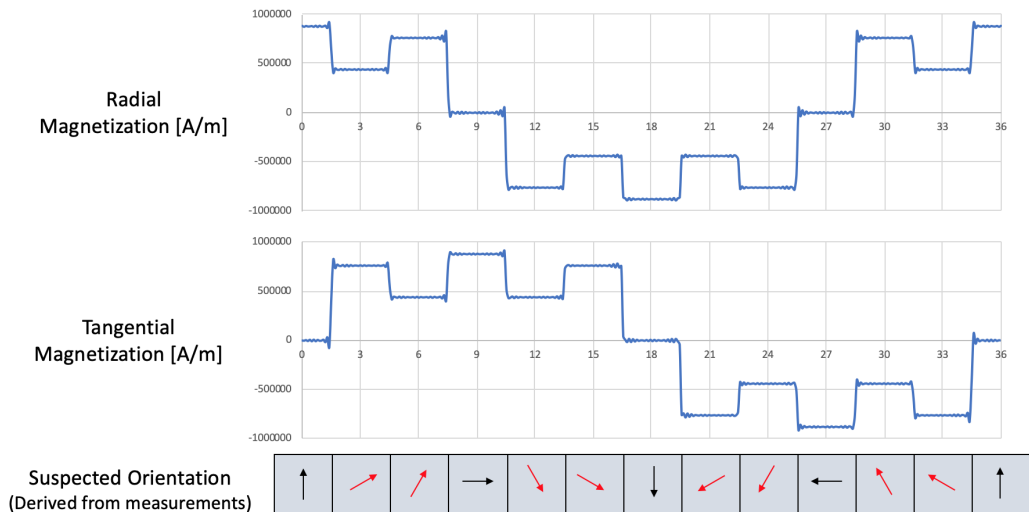
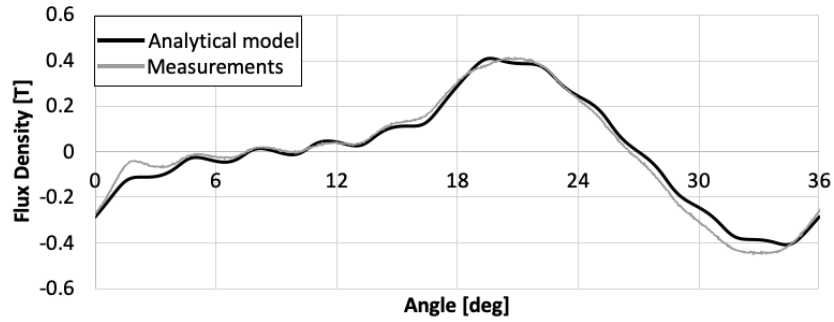
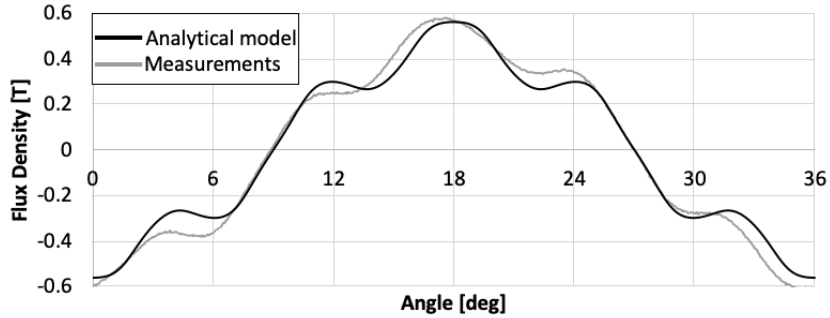


Figure 4.8: Suspected orientation based on Gauss meter measurements and corresponding magnetization vector (Assembly Trial II).

observed to match analytical results well. Any error between the analytical model and the Gauss measurements can be attributed to the magnetization strength of each magnet. While the analytical model assumes each magnet is magnetized with uniform remanent flux density, the process of magnetizing the pieces may not be completely uniform. For example, for the Assembly Trial I, magnets that occupy the space around $\theta_m = 3^\circ$ may have a lower strength than the desired specification. Another possible source of error can be non-uniform spacing between the magnets. When the two assemblies were



(a) Flux density comparison for Assembly Trial I.



(b) Flux density comparison for Assembly Trial II.

Figure 4.9: Comparison between magnetic field from analytical model and Gauss meter measurements.

visually inspected, gaps between some magnets were found to be larger than others. Ensuring even gaps between the magnet pieces is especially challenging for a Halbach array since the magnets are not uniformly oriented. Furthermore, since the Halbach array is assembled in segments before being mounted on the rotor shell, the dimensional tolerance of the rotor shell can also affect the non-uniformity of the gaps. This can cause uneven waveforms with even harmonic contents, as evidenced by Gauss measurements from Assembly Trial II. While the analytical model does not account for these manufacturing faults, the air gap field model compares well with the experimental data.

4.2 Losses

4.2.1 Iron losses

Numerous specific iron loss models have been proposed since Steinmetz' first formulation [31, 47, 48]. We found that the best model for specific iron loss allows for variable loss coefficients with frequency or induction, such that $k_h = f(B)$ and $k_e = f(B)$ [49]. Using this method, also referred to as the Cal2 method, specific iron loss in a stator yoke with yoke flux density, B_{yk} , at frequency, f , can be realized as

$$P_{yk} = k_h f B_{yk}^2 + k_e f^2 B_{yk}^2, \quad (4.17)$$

where the hysteresis loss varying coefficient, k_h , and eddy current loss varying coefficient, k_e , are each characterized as a cubic polynomial:

$$\begin{aligned} k_h &= k_{h,0} + k_{h,1} B_{yk} + k_{h,2} B_{yk}^2 + k_{h,3} B_{yk}^3 \\ k_e &= k_{e,0} + k_{e,1} B_{yk} + k_{e,2} B_{yk}^2 + k_{e,3} B_{yk}^3. \end{aligned} \quad (4.18)$$

Heat flux (W/m²) due to iron loss in the yoke can be expressed as

$$q_{yk} = [k_h f B_{yk}^2 + k_e f^2 B_{yk}^2] \rho_{fe} d_{yk}, \quad (4.19)$$

where ρ_{fe} and d_{yk} refer to volumetric mass density of yoke material and radial dimension of the yoke. Note that flux density in the yoke can be estimated as

$$B_{yk} = B_{ag} \frac{D_{ag}}{2d_{yk}p}, \quad (4.20)$$

where B_{ag} and p refer to peak air gap flux density and number of magnetic pole pairs.

Similarly, heat flux due to iron loss in the stator teeth can be shown as

$$q_{th} = [k'_h f B_{th}^2 + k'_e f^2 B_{th}^2] \rho_{fe} d_{th}, \quad (4.21)$$

where

$$\begin{aligned} k'_h &= k'_{h,0} + k'_{h,1} B_{th} + k'_{h,2} B_{th}^2 + k'_{h,3} B_{th}^3 \\ k'_e &= k'_{e,0} + k'_{e,1} B_{th} + k'_{e,2} B_{th}^2 + k'_{e,3} B_{th}^3, \end{aligned} \quad (4.22)$$

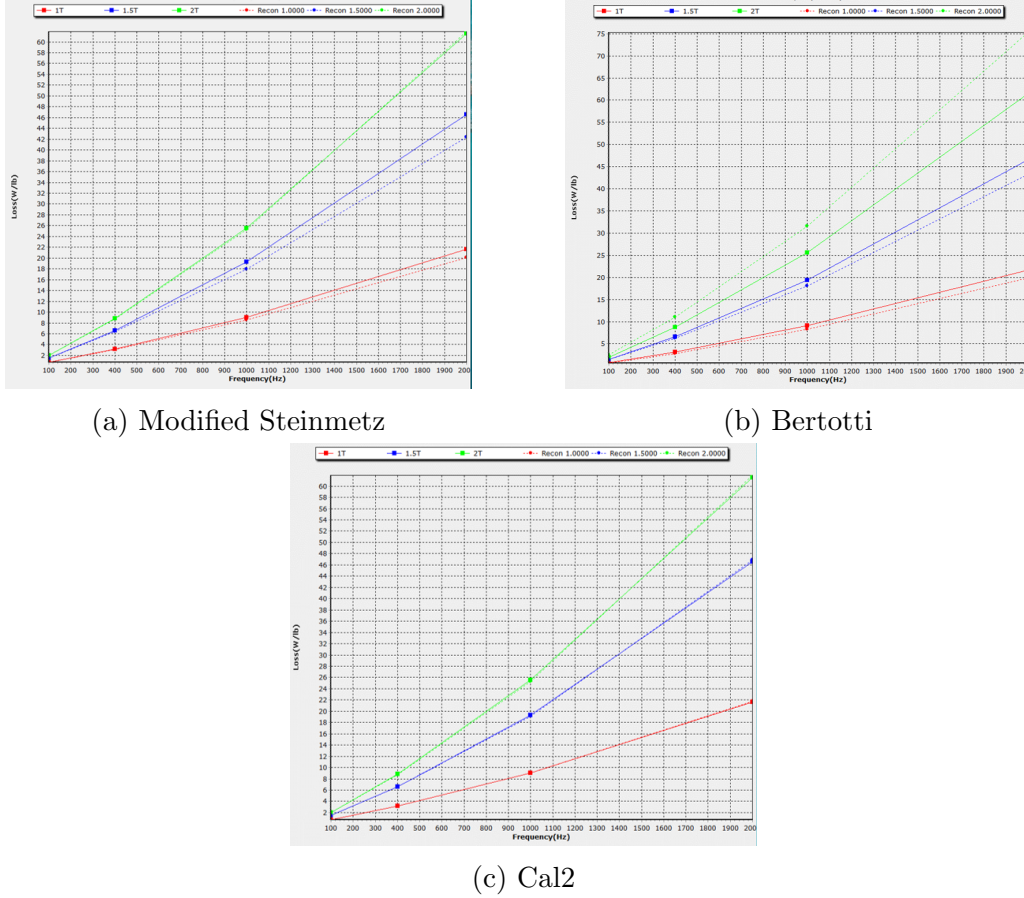


Figure 4.10: Iron loss model fit.

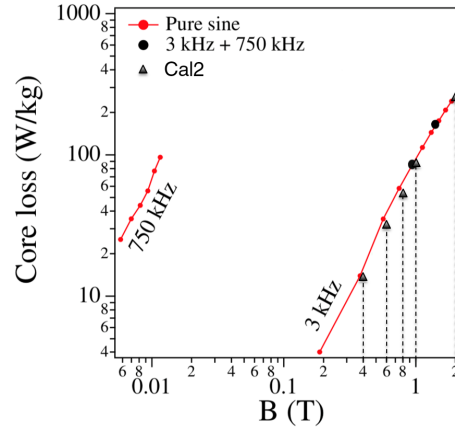
and flux density in the teeth, B_{th} , can be estimated as $B_{th} = B_{ag}/\tau$, where τ refers to teeth-to-slot pitch ratio. Fig. 4.10 shows the iron loss models, where the dotted lines represent the vendor data and solid lines represent model fit. While the modified Steinmetz and Bertotti models do not accurately fit the sample loss data, the Cal2 model is observed to fit the loss data well.

Observing the expressions for iron loss density, it is apparent that adoption of high frequency results in high iron loss density. While flux density in the yoke can be controlled to mitigate iron losses in the yoke, flux density in the teeth does not decrease with frequency or number of poles. Furthermore, while slot leakage, edge effects, and harmonics are not captured in the expressions, these effects may have more adverse effects on toothed topologies. In Chapter 5, toothed and toothless (slotless) topologies are compared.

To validate the model, a sample core of cobalt-iron alloy (“Vacoflux 48”) with lamination thickness of 0.05 mm was obtained from Vacuumschmelze,



(a) Vacoflux48 core with $N=65$ bifilar windings.



4.2.2 Copper losses

Several methods to analyze copper losses in Litz wire have been proposed [50–52]. Ac loss can be attributed to the skin and proximity effect. The skin effect is the tendency of high-frequency currents to flow on the conductor surface, whereas the proximity effect is the formation of eddy current loops from externally imposed varying magnetic fields. From [53], dc loss and ac loss are given as

$$P_{dc} = I_{rms}^2 R_{dc} \quad (4.23)$$

$$P_{ac} = \frac{\pi \omega_o^2 \bar{B}^2 n d_{str}^2 L_{act}}{128 \rho_{cu}}, \quad (4.24)$$

where ω_o , \bar{B}^2 , n , d_{str} , and ρ_{cu} refer to frequency, spatial average of peak flux density squared, strand number, copper strand diameter, and copper resistivity, respectively. These losses can be represented as heat flux as

$$q_{dc} = [J_{cu}^2 \rho_{cu}] d_{cu} ff (1 - \tau) \quad (4.25)$$

$$q_{ac} = \frac{\omega_o^2 \bar{B}^2 d_{str}^2}{32 \rho_{cu}} d_{slot} ff (1 - \tau), \quad (4.26)$$

where J_{cu} , d_{cu} , and ff refer to copper current density, radial dimension of copper coils (or slot), and copper fill factor. For the toothed topology, \bar{B}^2 represents flux density due to slot leakage. For the slotless topology, the windings lie directly in the path of the magnet flux and are expected to have higher ac losses.

Using the analytical models detailed in the last subsection, copper losses at various Litz wire strand diameters are computed and presented in Fig. 4.12. Good agreement is shown between analytical results and finite element analysis. However, to accurately assess the FEA results with experimental results, indirect balance calorimetry is used for its high-precision loss measurement capabilities, and the experiment setup is shown in Fig. 4.13. Results are shown in Fig. 4.14, where 11-13% error is consistently observed. Details of the experiment can be found in [23].

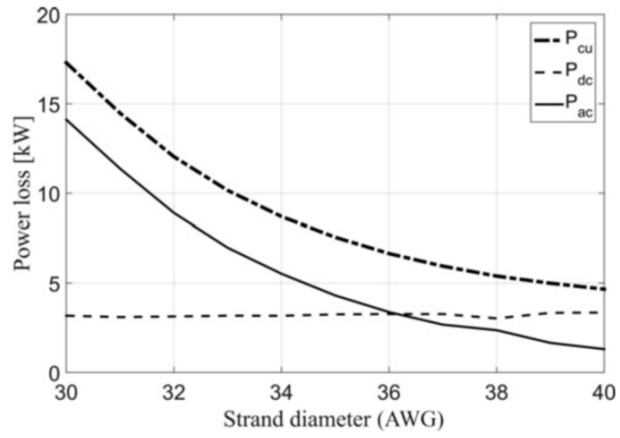


Figure 4.12: Copper losses at various strand diameters.

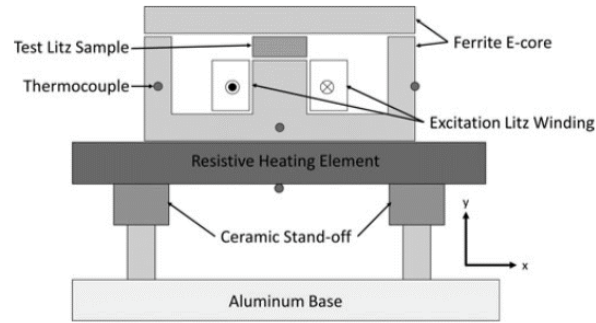


Figure 4.13: Schematic of indirect balance calorimetry test bench.

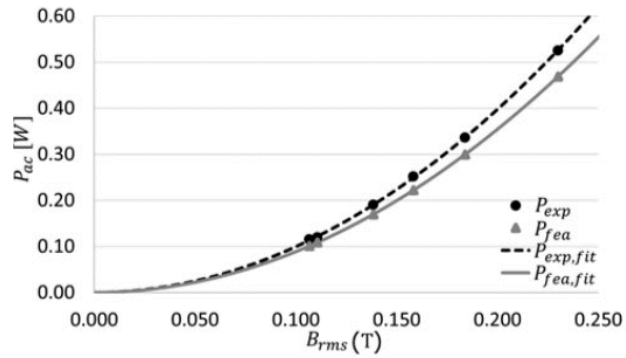


Figure 4.14: Experimental and FEA results.

4.2.3 Mechanical losses

Proper characterization of mechanical losses such as friction, windage, and bearing losses is especially important when considering high-speed machines. While there is no universal model for obtaining bearing losses, vendors typically provide such data. Windage losses can be represented as

$$P_{wind} = \frac{1}{2}\pi\rho n^3 R^4 LC_{cm}, \quad (4.27)$$

where

$$C_{cm} = 0.065(\delta/R)^{0.3} Re^{-0.2}, \quad (4.28)$$

and ρ , n , R , L , δ , and Re refer to air density, angular speed, rotating surface radius, rotating surface length, gap thickness, and Reynolds number [54]. Note that for obtaining windage losses in the air gap, δ is equal to air gap length. For obtaining windage losses in non-constrained surfaces, a hydrodynamic boundary layer must be found and used as δ . If a representative rotor is manufactured and windage losses are obtained experimentally, then (4.27) and (4.28) can be combined to find that windage losses can be scaled with diameter and length as

$$P_{wind} \propto n^{2.8} R^{3.5}. \quad (4.29)$$

A representative motor was built and tested to validate the analytical model. Fig. 4.15 shows the device under test and Fig. 4.16 shows estimated and measured windage loss. Note that the previously described analytical model for windage losses refers to “method 2” in Fig. 4.16. While the analytical model presents an over-estimation of the actual windage losses, general characteristics of losses vs. speed are comparable. Proper scaling of the analytical results may be adequate for a quick first-order assessment of windage losses of various designs for trade-off studies. Further details of the experiment can be found in [24].



Figure 4.15: Representative prototype in spin pit.

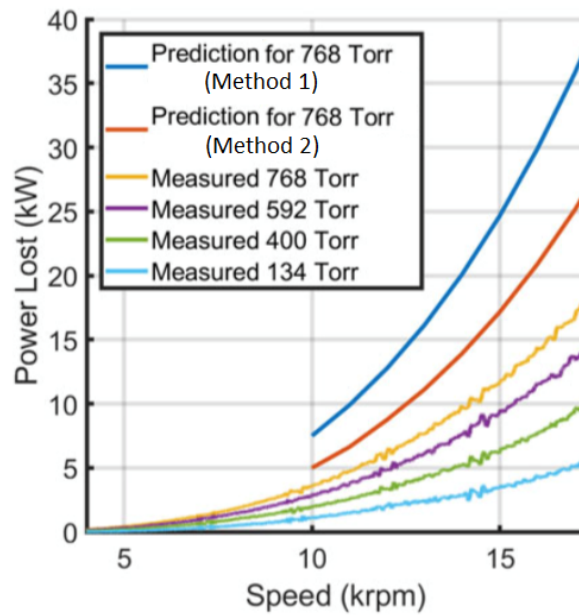


Figure 4.16: Analytical estimates of windage loss and experimental results.

CHAPTER 5

CASE STUDIES

5.1 Toothed topology vs. slotless topology

In this section, previously discussed loss models and torque computation models are used to examine whether certain topologies are favored at high frequencies. More specifically, a conventional toothed machine and a slotless machine will be compared with the 1 MW high-speed motor from Chapter 3 as the baseline.

For effective comparison of specific power between the conventional toothed topology and the proposed slotless topology, analytical models and loss models are coupled with an evolutionary genetic algorithm toolbox for MATLAB. The optimization is performed at various frequencies, within the design space of free variables given by

$$\theta_{fr} = \left[d_{cu} \quad d_{pm} \right]^T, \quad (5.1)$$

where d_{cu} and d_{pm} refer to radial dimensions of coils and magnets. Fixed variables are given by

$$\theta_{fx} = \left[D_o \quad q_{ag} \quad P \quad B_{yk} \right]^T, \quad (5.2)$$

where q_{ag} refers to the total heat flux ($q_{ag} = q_{fe} + q_{cu} + q_{mech}$). D_o , P , and B_{yk} refer to machine outer diameter, rated power, and yoke flux density, respectively. To quantify the rated torque and rated power of the slotless topology, transfer relations developed in Chapter 4 are used. For the conventional toothed topology, effective magnetic airgap distance is calculated as

$$g' = gc_s, \quad (5.3)$$

where g refers to physical airgap, and c_s refers to Carter's coefficient,

$$c_s = \frac{w_{ss} + w_{wt}}{w_{st} + \frac{4g}{\pi} \ln \left(1 + \frac{\pi w_{ss}}{4g} \right)}, \quad (5.4)$$

where w_{ss} and w_{st} refer to slot width and tooth width, respectively [55]. The obtained effective airgap is used with the transfer relation model to obtain the field in the airgap. Tooth width to slot pitch ratio, τ , of 0.5 is assumed.

A few assumptions are made to constrain the problem. For high frequencies, thin gauge lamination thickness (< 14 mils) is recommended [56]. Considering the practicality of thin laminations (in terms of manufacturability, handling, and availability), 7 mil lamination thickness is chosen. Low strand diameter wires are chosen to minimize ac losses. Tip speed is fixed to match the baseline design to focus the trade-off study on electrical and magnetic loading comparison. With a reference speed of 15000 rpm, frequency is increased while speed is kept constant. A minimum efficiency requirement of 96% is enforced.

Fig. 5.1 shows the comparison of specific power at different operating frequencies for two topologies.

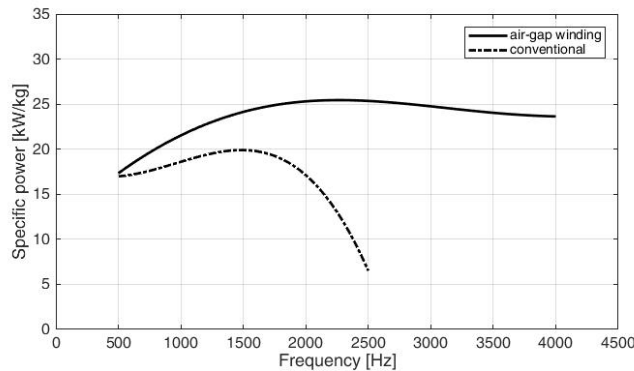


Figure 5.1: Specific power comparison between slotless topology and conventional toothed topology at different frequencies and $N = 15$ krpm.

As expected, while the benefit in weight for the slotless topology is apparent at higher frequencies, conventional toothed machines may display higher specific power at lower frequencies. Note that the data is not provided for the conventional toothed machine at frequencies higher than 2500 Hz because the

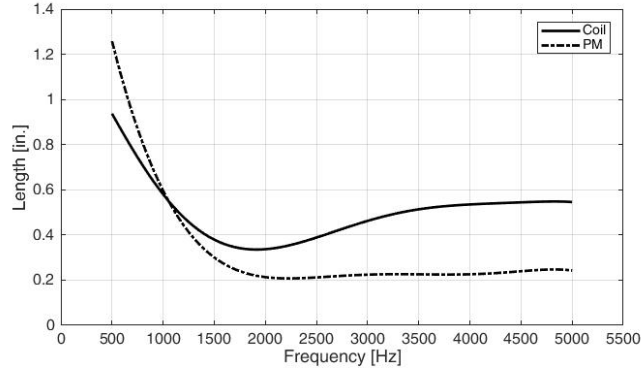


Figure 5.2: Radial dimensions of coil and magnet for the slotless topology.

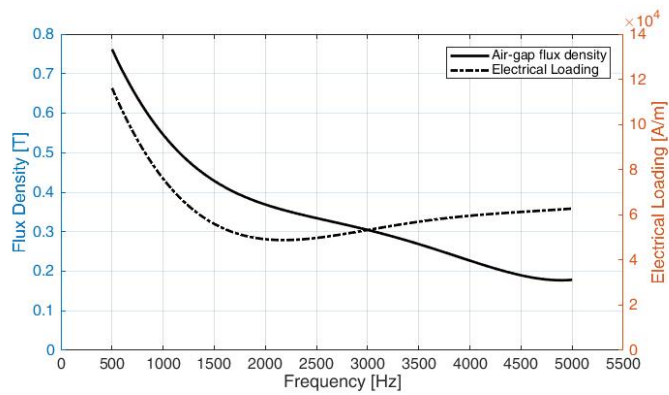


Figure 5.3: Comparison of electrical and magnetic loading for the slotless topology.

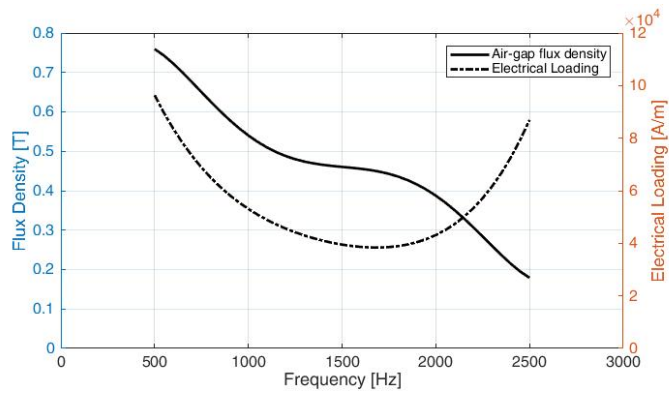


Figure 5.4: Comparison of electrical and magnetic loading for toothed topology.

efficiency constraint cannot be satisfied at higher frequencies for this particular speed chosen. A similar trend is expected for motor designs with various rotational speeds, assuming the same tip speed across the designs. At higher

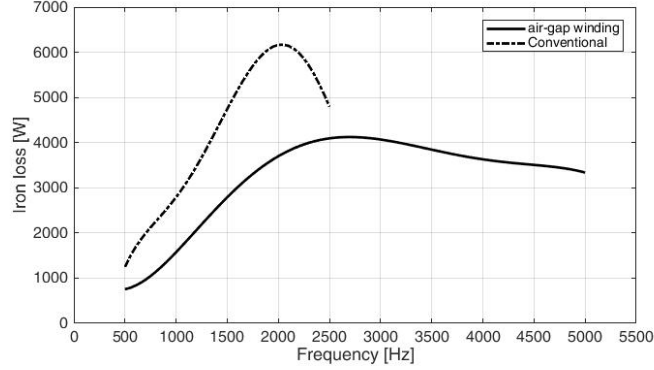


Figure 5.5: Comparison of electrical and magnetic loading for toothed topology.

speeds, the machine diameter decreases, being able to accommodate lower pole count.

In Fig. 5.2, decrease in radial length with increasing frequency is observed for the slotless topology, which can be directly related to the weight of the machine. However, as the efficiency of the topology reaches the minimum requirement at around 1750 Hz, the radial length is increased to maintain the 96% efficiency while sacrificing the specific power. A similar observation can be made in Fig. 5.3, where electrical loading and magnetic loading for the slotless topology are shown. As frequency increases, magnetic loading is decreased to account for iron losses, and electrical loading is forced to increase to maintain torque. Fig. 5.4 shows a similar trend.

The main difference between the two topologies is the presence of stator teeth. For the slotless topology, varying the dimension of magnets and copper radial dimension (because of the absence of teeth) can, to some degree, control the iron losses within a manageable amount. However, teeth are observed to cause very high iron losses, as shown in Fig. 5.5. Here, iron losses for the toothed topology are observed to increase faster than those of the slotless topology. Note that the decrease in iron losses for the toothed topology after 2000 Hz is due to the enforced efficiency constraint.

5.2 STARC-ABL

The previous section demonstrates that the slotless machines show a potential benefit in specific power at high frequencies, as shown in (2.11). However, the benefit of the high-frequency, slotless topology must also be studied to account for various applications of lightweight machines. Specifically, many aircraft propulsor designs have low angular velocity (~ 3000 rpm). While power density and specific power of conventional machines, described by (2.9), are thought to diminish at lower speeds, (2.11) shows that as long as high tip speed is maintained, high specific power can be achieved. To investigate the claim, designs are optimized at various speeds, while the tip speed of the rotor is kept constant.

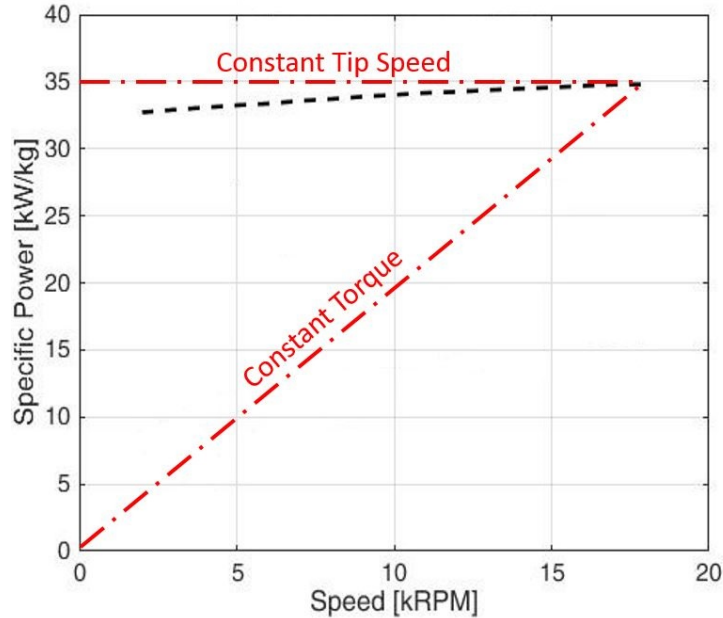


Figure 5.6: Specific power (active material only) of slotless machine at different angular speeds. Additional lines illustrate ideal cases of torque-sized machines and constant tip speed machines.

In Fig. 5.6, the line labeled “constant torque” illustrates machines described by (2.9). With electrical loading and magnetic loading restricted due to thermal and material constraints, specific power of torque-sized machines decays to zero with low angular speeds. However, if the size of the motor is allowed to grow to maintain high tip speeds even at lower rotational speeds, specific power is seen to decay only a little. The discrepancy between the

ideal constant tip speed case (labeled “constant tip speed” in Fig. 5.6) and the simulated case can be attributed to high dc losses at lower speeds. At these speeds, the D/L ratio of the machine grows and the effects of end windings become more prominent.

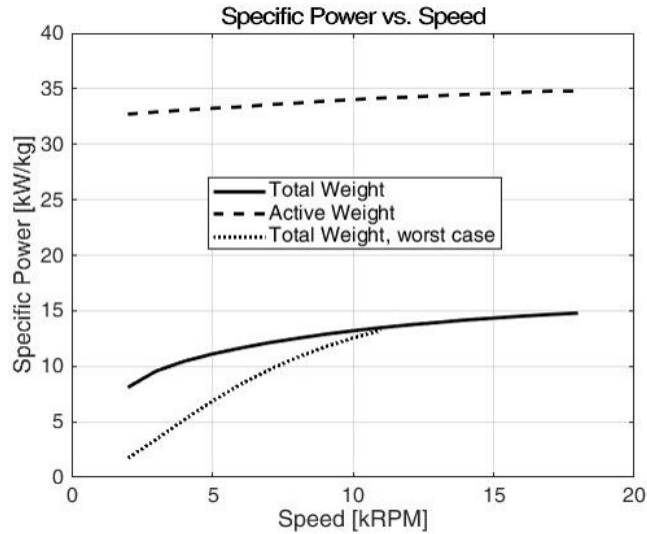


Figure 5.7: Specific power (auxiliary weight added) of a slotless machine at different angular speeds.

In Fig. 5.7, specific power of the designs considering the total weight of the machine is shown. While the growth in diameter allows the tip speed of the machine to stay constant, the structural weight of the machine is observed to cause rapid decrease of specific power (curve labeled “worst case” in Fig. 5.7). More specifically, the weight of the end plate region seen in Fig. 3.4 increases significantly, when the motor is applied to a notional electric propulsor. Another curve labeled “total weight” assumes a different system context where the motor may be directly integrated with the fan blades to reduce the weight increase associated with the end plate.

Following these results, a more extensive investigation is performed to compare the weight among several motor designs for an electric fan. The specific target application of this case study is the tail cone propulsor for the NASA’s newly proposed turboelectric concept aircraft called STARC-ABL. STARC-ABL stands for a single-aisle turboelectric aircraft with an aft boundary-layer propulsor and the aircraft is shown in Fig. 5.8. The 2.6 MW, 3000 rpm boundary layer propulsor allows reduction of drag that exists on the fuselage of an aircraft by ingesting the hydrodynamic boundary layer



Figure 5.8: STARC-ABL concept. (NASA photo).

that exists on the surface, which allows for a significant reductions in system fuel burn [57, 58].

Upon examining the geometry of the tail cone propulsor published in [57, 58], three possible motor-fan integrations are realized:

1. High speed, outer rotor (fan driven via a gearbox)
2. Direct drive, outer rotor (motor located at the base of the fan blades)
3. Direct drive, inner rotor (motor located at the tip of the fan blades, “rim driven”)

These concepts are illustrated in Fig. 5.9. Concept 1, with an operating speed of 15,000 rpm, has the potential for highest specific power. However, with a need for a 5:1 gear, both efficiency and specific power may be reduced. The second concept is a direct drive motor, with operating speed of 3000 rpm. The last concept places the motor at the tip of the fan with an operating speed of 3000 rpm. Fig. 5.10 and Fig. 5.11 illustrate what Concept 2 and Concept 3 motors would look like when integrated to the fan.

5.2.1 Multi-objective optimization scheme

For fair comparison of specific power and efficiency across different concepts, an evolutionary genetic algorithm toolbox for MATLAB, i.e., GOSET [60], was utilized to obtain a Pareto optimal front for each concept. The opti-

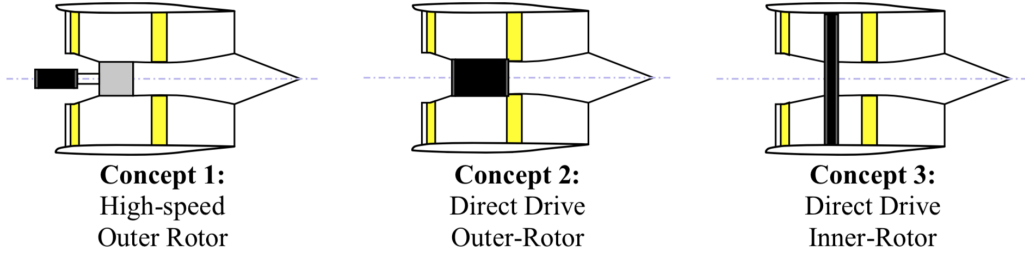


Figure 5.9: Schematic of the STARC-ABL tailcone propulsor showing three possible locations for the motor [59].

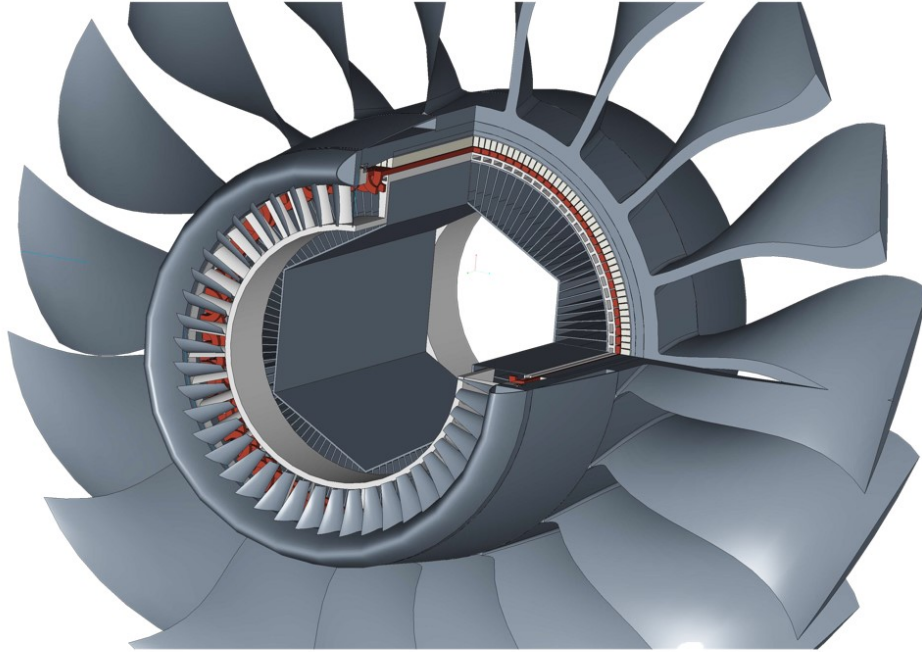


Figure 5.10: CAD illustration of direct drive, outer rotor motor and fan integration [59].

mization was performed within the design space of free variables,

$$V_{free} = \left[p \quad d_{cu} \quad d_{pm} \quad L_{act} \quad J_{slot} \right]^T, \quad (5.5)$$

where p , d_{cu} , d_{pm} , L_{act} , and J_{slot} refer to number of pole pairs, copper radial height, magnet radial height, active length, and slot current density, respectively. Since this is a slotless topology, each winding block is referred to as a

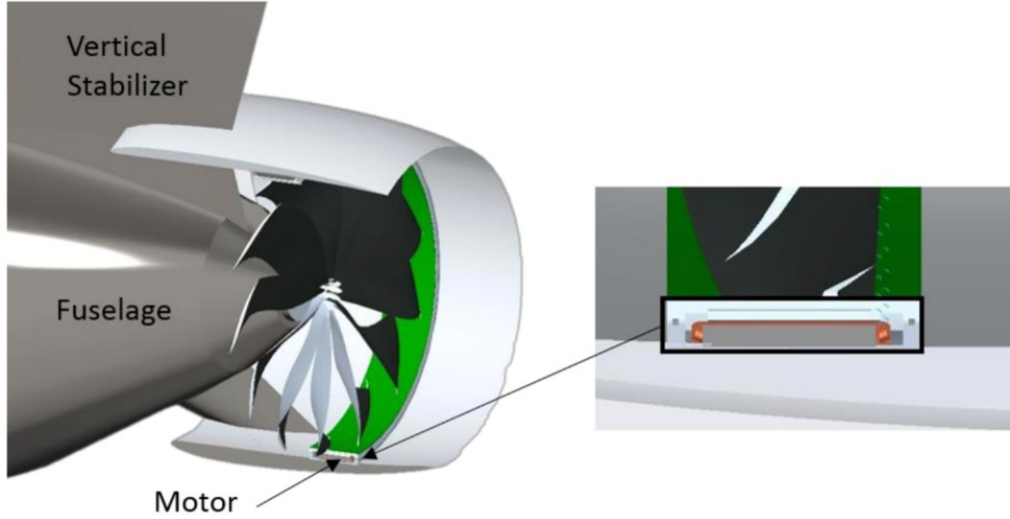


Figure 5.11: CAD illustration of direct drive, inner rotor rim driven fan integration [59].

slot. Fixed variables were included to constrain the optimization problem as

$$V_{fixed} = \left[\omega_m \quad q_{ag} \quad P \quad B_{yk} \quad D_o \right]^T, \quad (5.6)$$

where q_{ag} refers to total heat flux in the air gap such that $q_{ag} = q_{yk} + q_{dc} + q_{ac} + q_{wind}$. ω_m , P , B_{yk} , and D_o refer to mechanical angular speed, rated power, peak yoke flux density, and machine outer diameter, respectively. The heat flux in the air gap, denoted as q_{ag} , was fixed to that of the baseline design across different concepts and designs, as it was treated as a cooling specification. Experiences with the fan design from the baseline design suggest that $q_{ag} = 65 \text{ kW/m}^2$ is manageable with a 20 m/s airflow through the heat exchanger. While this assumption may not be completely true in other design concepts, it is useful in providing first-order comparison between the concepts.

The free variables, along with the constraints enforced by the fixed variables (such as P , B_{yk} , and D_o), were applied to the slotless, outer rotor transfer relation model developed in Chapter 4. Distance variables (α , β , γ , δ) from the transfer relation model were flipped to calculate torque for the Concept 3 topology with an inner rotor. Iron loss, copper loss, and windage loss for each concept are calculated using the models discussed from Chapter 4.

Permenorm 500V5 is chosen as the stator yoke material across all designs for its low iron loss characteristics. Hysteresis loss varying coefficient, k_h , and eddy current loss varying coefficient, k_e , of this material at a 4 mil lamination thickness are calculated to be

$$\begin{bmatrix} k_{h,0} \\ k_{h,1} \\ k_{h,1} \\ k_{h,2} \end{bmatrix} = \begin{bmatrix} 7.9312 \times 10^{-3} \\ -4.0627 \times 10^{-4} \\ -1.0379 \times 10^{-2} \\ 6.9669 \times 10^{-3} \end{bmatrix} \quad (5.7)$$

$$\begin{bmatrix} k_{e,0} \\ k_{e,1} \\ k_{e,1} \\ k_{e,2} \end{bmatrix} = \begin{bmatrix} 1.1698 \times 10^{-5} \\ -3.0958 \times 10^{-5} \\ 3.9228 \times 10^{-5} \\ -1.4954 \times 10^{-5} \end{bmatrix}, \quad (5.8)$$

where these coefficients fit the model described in (4.17).

From the input, V_{free} , the algorithm generates candidate designs and outputs a Pareto front that investigates the tradeoff between total weight, W_{tot} , and efficiency, η , with fitness functions given by

$$f(V_{free}) = \left[\frac{1}{W_{tot}} \quad \frac{1}{\eta} \right]^T. \quad (5.9)$$

To assess the total weight of a design, a detailed CAD model is used. With information from the baseline design, radial dimensions of structural components such as titanium, shell and carbon fiber retaining ring can be scaled for various rotor tip speeds. The effect of stack length on end plate thickness is also included to account for static deflection (thickness of end plate $\propto 1/L_{stack}$) [44]. In addition to materials, fixed Litz wire strand diameter, fill factor, and yoke lamination thickness are enforced. Note that the strand diameter is chosen to accommodate the skin depth at the maximum frequency used in the study.

5.2.2 Optimization results and concept comparison

Fig. 5.12 shows the results from the optimization study, as generated with 500 individual, 500 generation optimization runs per design. For Concept 1,

gearbox loss of 1% is assumed and the weight of the gearbox is estimated using empirical correlations from a survey of numerous gearboxes used in aircraft applications [61].

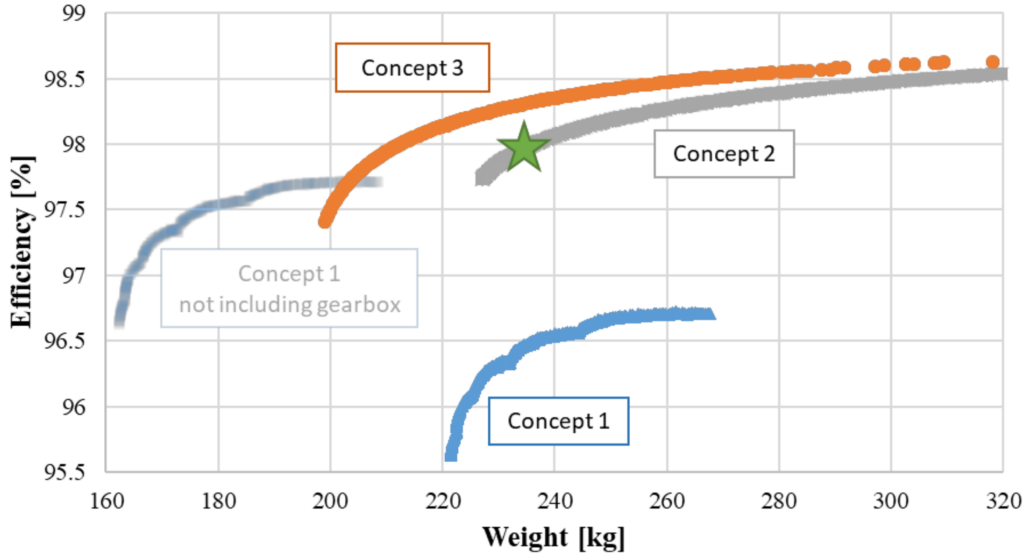


Figure 5.12: Case study results showing Pareto optimal front for three designs using genetic algorithm. The star symbol marks the final choice for BLI fan motor.

Upon comparison of the results, the benefits of 15000 rpm operation with an outer rotor motor are once again highlighted. With high rotational speed and high tip speed, the motor designed for Concept 1 displays the lowest weight among the three motors. However, when the effect of a gearbox is added, the high-efficiency, low-weight characteristics are compromised. The outer-rotor motor (Concept 2) in the plot shows potential for high efficiency, but with higher weight. The extra weight is in agreement with the fact that low rotor tip speed causes reduction in specific power. With a speed constraint of 3000 rpm and outer diameter constraint of 23 inches, tip speed of the motor is constrained to 1/4 to that of the Concept 1 and Concept 3 motors. The rim-driven fan design, however, has high tip speeds even at low rpm due to its larger outer diameter. The benefit of high tip speed is clear, while the high frequency causes slightly lower efficiency. Furthermore, because the rotor is no longer on the outside of the motor, the cantilevered design and its associated auxiliary weight can be eliminated. With an outer stator, the aluminum heat exchanger can also be eliminated since the heat due to copper and iron losses can be directly extracted from the outer surface of the ma-

chine. While this rim-driven fan topology seems optimal at a glance, having electromagnetic interaction at such a large diameter comes with significant mechanical risks and difficulty identifying appropriately rated bearings, and thus may not be a feasible concept.

A common parameter that drives the weight-efficiency tradeoff for the three concepts is found to be pole count (or rather, frequency). For example, an examination of the Pareto front for Concept 2 shows that the design with lowest efficiency and weight has 40 poles (1000 Hz), whereas the design with highest efficiency and weight has 14 poles (350 Hz). The 40 pole design is characterized by a very thin radial build at the expense of high ac losses, where the opposite is true for the 14 pole design. This is illustrated in Fig. 5.13, where both magnet radial height and copper radial height are observed to reduce due to high pole count designs toward the left of the curve.

Figs. 5.14 and 5.15 provide more insight into the trade-off between weight and efficiency of the most favorable concept - Concept 2. Because of the reduced radial dimensions for the magnet and the constrained outer dimension, air gap diameter is allowed to increase, as seen in Fig. 5.14. It is also interesting to note that these low weight, lower efficiency designs demonstrate longer active length than the designs on the far right. This indicates that the effect of higher pole, higher frequency designs on reduction in weight is greater than the effect of longer active length. Fig. 5.15 shows a trend in reduced electrical loading and magnetic loading for lower efficiency, low weight designs to accommodate higher losses.

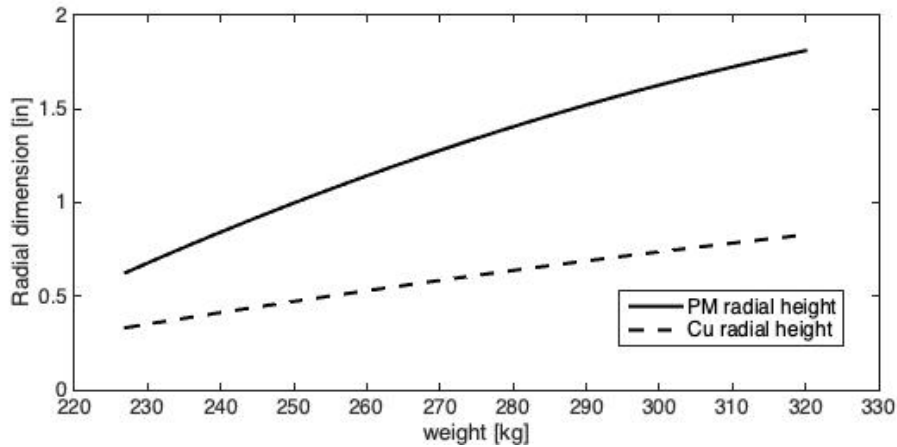


Figure 5.13: PM radial height and coil radial height for different designs for Concept 2.

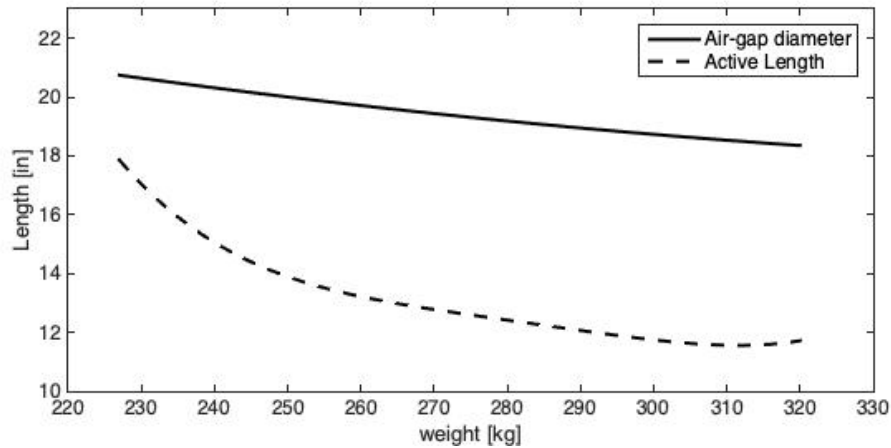


Figure 5.14: Air gap diameter and stack length for different designs for Concept 2.

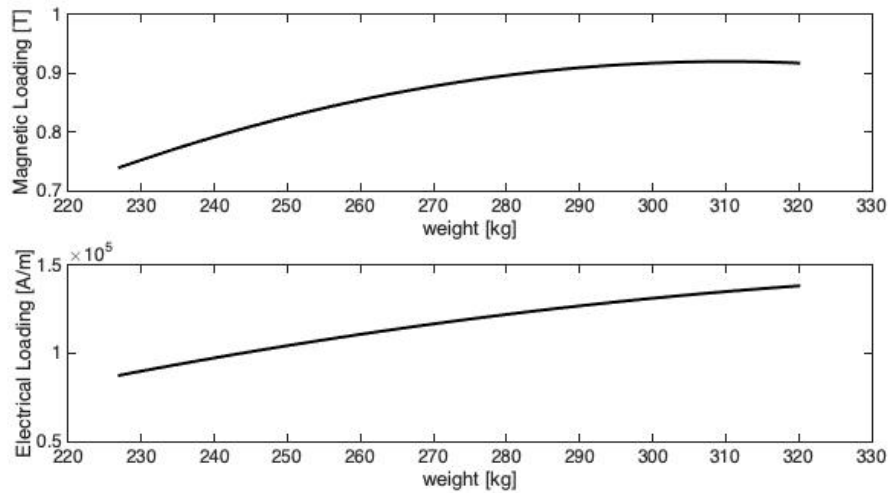


Figure 5.15: Electrical and magnetic loading for different designs for Concept 2.

5.2.3 Selected design

With various considerations discussed in the previous section, a final concept and design was chosen and marked with the star symbol in Fig. 5.12. While the weight of the machine is critical for aircraft, an additional 2 points of efficiency over the assumed 96% metric used in the STARC-ABL feasibility study in [57] could be valuable in a propulsion system context. Key metrics

and dimensions for the final design can be found in Table 5.1. The motor voltage is determined to be 470 V (rms, line-line). Modular inverters should be used to drive the motor to accommodate appropriate current ratings.

Table 5.1: Key metrics and dimensions for the selected motor

| | | |
|------------------------------|-------|-------|
| Rated Power | 2.6 | MW |
| Rated Efficiency | 98 | % |
| Nominal Speed | 3000 | rpm |
| Cooling, Forced air | 20 | m/s |
| Tip Speed | 93.76 | m/s |
| Outer Diameter | 23.5 | in. |
| Number of Poles | 32 | - |
| PM Radial Thickness | 0.84 | in. |
| Air Gap Diameter | 20.3 | in. |
| Coil Radial Thickness | 0.40 | in. |
| Stator Yoke Radial Thickness | 0.36 | in. |
| Physical Air Gap | 0.094 | in. |
| Stack Length | 15.3 | in. |
| Specific Power | 11 | kW/kg |
| Total Weight | 230 | kg |

Electromagnetic performance and a power rating of 2.6 MW were verified using FEA, where the model shown in Fig. 5.16 highlights the thin radial build of the topology. A loss breakdown of the machine is shown in Fig. 5.17. With tip speed that is only a third of the baseline 1 MW design, the percentage of windage losses is found to be much lower (compared to 70 % of the losses being windage in the baseline motor). As a result, a bigger percentage of air gap heat flux can be allocated to copper losses, allowing for more electrical loading (2.3 times larger), and thus maintaining a >10 kW/kg of specific power.

The hotspot temperature for this design was analyzed using thermal FEA, as shown in Fig 5.18. A periodic model with one coil segment was used to reduce the computational expense while capturing the most important heat transfer considerations. A heat source of 225 W was applied to the copper coils. This value corresponds to the total expected copper losses divided by the number of coil segments. Iron loss and windage loss at the air gap have also been included in the study. Across the heat sink, a convection boundary condition was applied with an air flow of 20 m/s at an ambient temperature of 23 °C. More moderate cooling is assumed in the air gap, with an air flow of 10 m/s [39]. These assumptions are analogous to the

studies performed for the baseline design [39]. The results show that the copper coils operate at an average temperature of about 150 °C, with a hotspot temperature of 176 °C. This two-dimensional analysis shows that the hotspot temperature is within the temperature rating of the intended Class H insulation. However, a more rigorous investigation considering the effects of atmospheric conditions at altitude and 3-d effects must be performed. For example, while the temperature at cruise altitude is around -56.5 °C, and can greatly help management of thermal losses, proper fan design must consider that atmospheric pressure drops by a factor of five (compared to sea level).

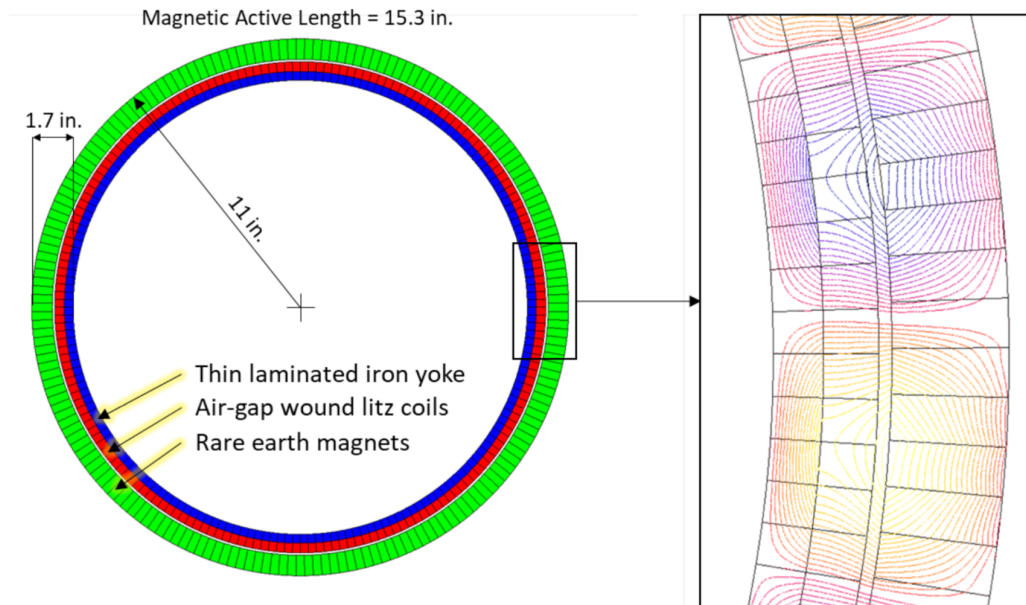


Figure 5.16: Electromagnetic finite element model and resulting magnetic field lines.

Mechanical analysis of the retaining ring is performed to ensure integrity of the rotor structure. This is important to ensure proper contacts with the bearings, which do not provide any support in tension. A static FEA was performed using Autodesk Inventor on a section of the periodic rotor. Boundary conditions and material properties were prescribed as shown in Fig. 5.19. The right end of the rotor is assumed not to expand due to added material from the fan and is set as a fixed boundary condition. The left end of the motor is open to expand. This direct drive motor is assumed to spin with a fan speed of 3000 RPM to generate radial body forces pointing away from the center of the motor. Note that the mechanical simulations were performed using retaining ring material properties at room temperature.

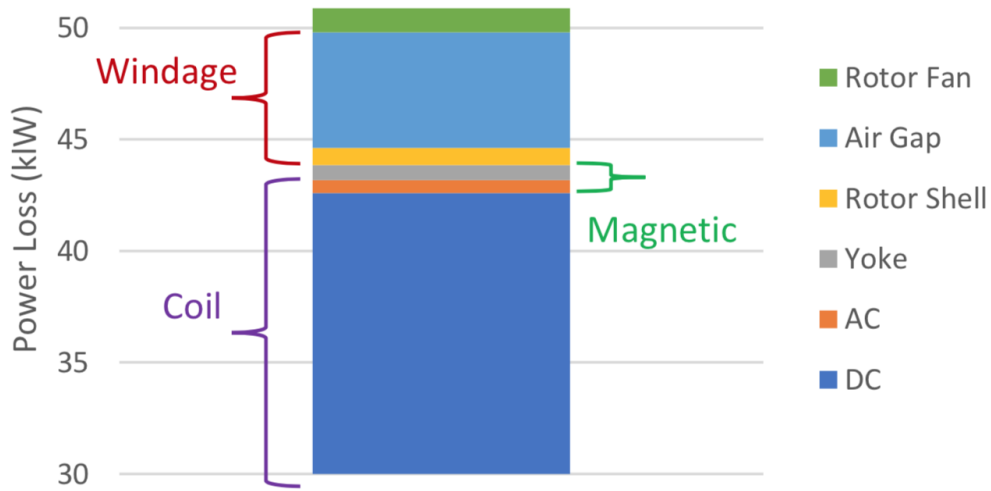


Figure 5.17: Loss breakdown of the selected design.

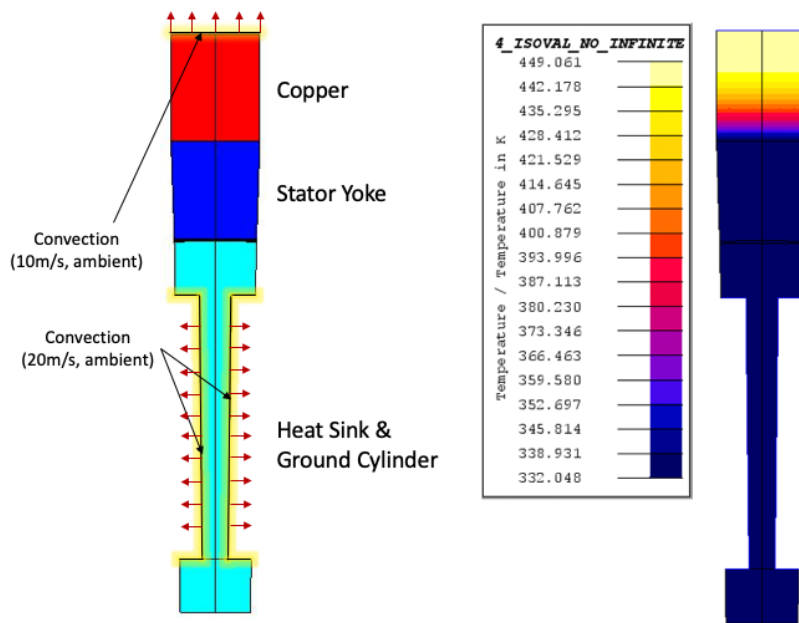


Figure 5.18: Thermal finite element model and resulting heatmap.

The effects of heat flux from the coils on the carbon fiber retaining ring and titanium are neglected in this analysis, because of convective cooling in the air gap. The heat flux due to windage at the rotor outer diameter is found to be small (as seen in Fig. 5.17) and thus was also excluded for this analysis. The results of the finite element analysis are presented in Fig 5.20. The maximum stress experienced in both the rotor shell and retaining ring are

well below the endurance life of carbon fiber and titanium, where endurance life is taken as half of the ultimate strength. The maximum displacement of the rotor is near 0.15 mm, validating the ability of the retaining ring to keep the rotor in contact with the bearings.

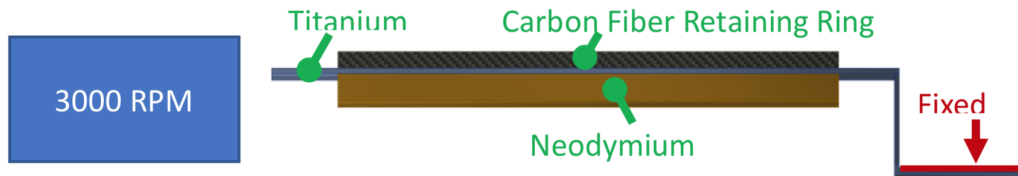


Figure 5.19: Mechanical boundary conditions for rotor finite element analysis.

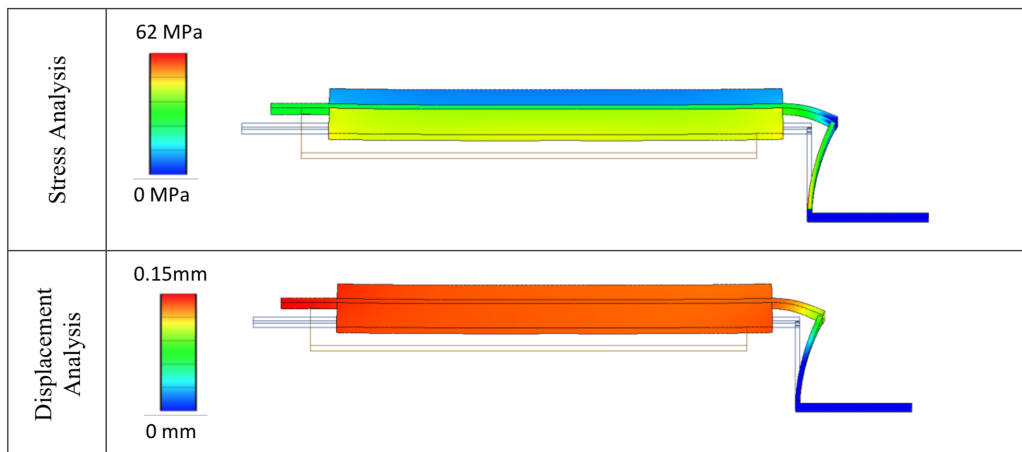


Figure 5.20: Results of retaining ring structural analysis.

A CAD rendering of the selected direct drive 2.6 MW BLI fan motor is shown in Fig. 5.21. Note that the fan shown in the figure is only for illustration and is not optimized to force air through the heat exchangers. Another iteration of design optimization will be performed in conjunction with a propulsor fan design, where the effects of fan dynamics will be taken into account. Because of the substantial axial load associated with propulsors, proper bearing choices will need to be made.

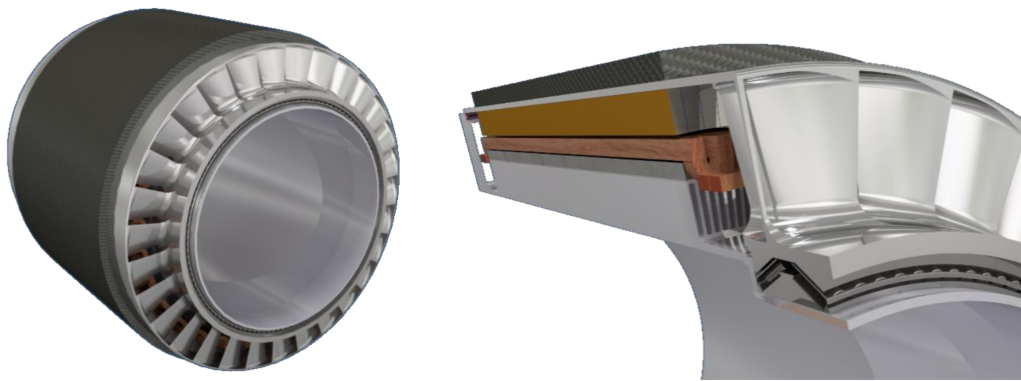
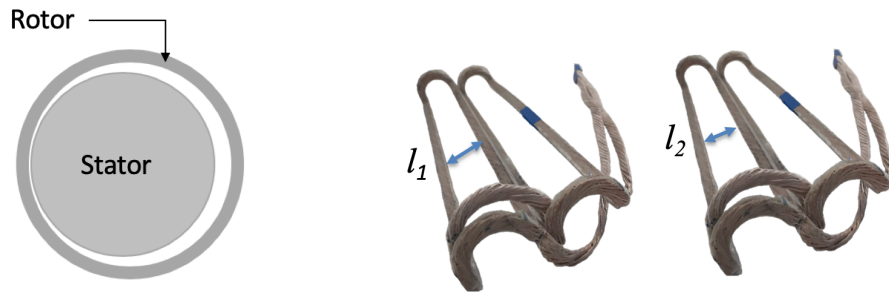


Figure 5.21: CAD rendering of Concept 2 motor selected from design optimization results. Fan and bearings shown in the rendering are not representative of the final design.

CHAPTER 6

EFFECTS OF MANUFACTURING TOLERANCES ON CIRCULATING CURRENT

As presented in earlier chapters, the benefits of the proposed topology in terms of reduction in weight and volume are clear. However, the cantilevered, outer rotor topology coupled with a slotless armature not only makes manufacturing the motor with tight tolerances a challenge, but also makes the topology more sensitive to the effects of these manufacturing tolerances. These effects may include significant circulating currents [62–64] and unbalanced magnetic forces and torque ripple. This chapter focuses on the effect on circulating currents in the form of imbalanced back-EMF between the coils. Fig. 6.1 shows two consequences of manufacturing the cantilevered, slotless motor.



(a) Rotor eccentricity. Rotor and stator center may not be aligned, causing varying air gap. (b) Imbalanced coils. l_1 may not equal l_2 causing variance in coil inductance.

Figure 6.1: Challenges of manufacturing a cantilevered, slotless motor.

A conventional megawatt class motor is characterized by a rotor that is supported by two bearings on each end. But in the case of the cantilevered rotor, the rotor is prone to eccentricity with respect to the stator. The resulting varying air gap length can lead to differences in back-EMF magnitude between the coils. The rotor eccentricity can cause differences between coil axis and the rotor direct axis, causing a phase shift between the back-EMFs.

This chapter considers the cantilevered structure with two bearings to be more prone to static eccentricity and considers only the effect of static eccentricity.

Conventional motors are characterized by nearly constant spacing between the coils, ensured by stator teeth. The stator laminations are usually stamped with very tight tolerances (± 5 mils, or 0.127 mm). These motors are insensitive to varying coil dimensions because the magnetic circuit is defined by the teeth. However, in the absence of these teeth, these pre-cast Litz coils may not be dimensionally identical to one another, creating imbalanced windings. Further imbalance can happen during the winding placement process on the stator yoke as well.

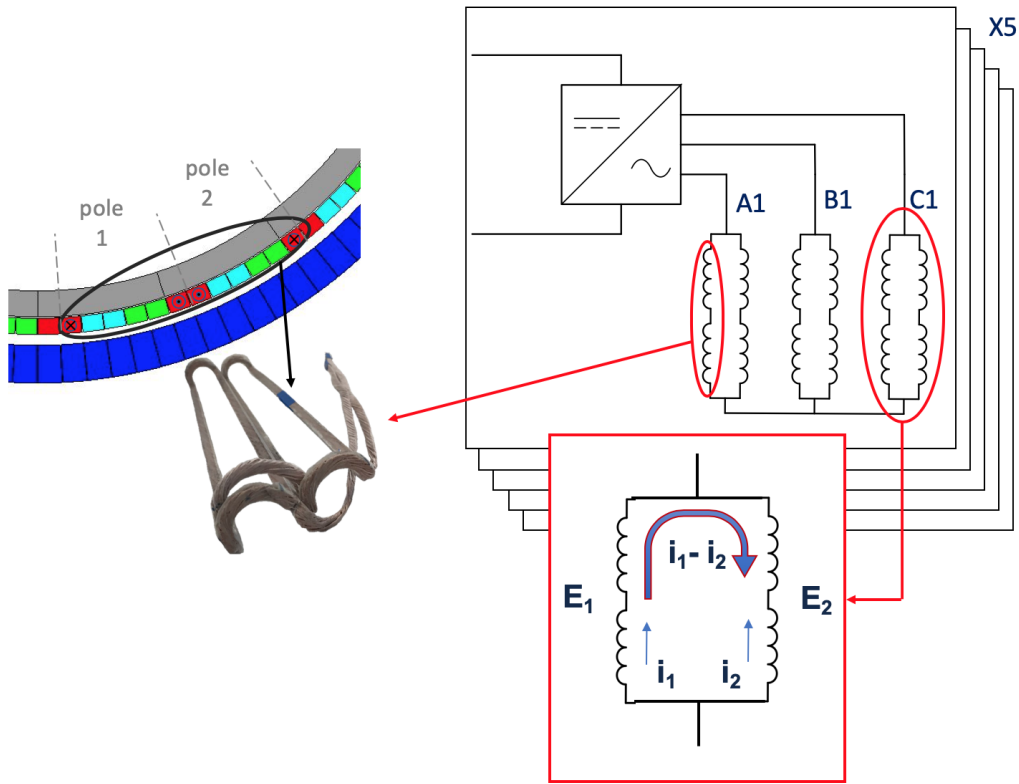


Figure 6.2: Armature coil connection and drive integration.

The effect of both static eccentricity and imbalanced coils could cause circulating current. As shown in Fig. 6.2, the armature consists of a 3 phase, 20 pole distributed winding with 2 slots per pole per phase (10 pre-cast coils per phase), and a 5/6th winding pitch. A total of five inverter modules will drive a section of the motor, where each module drives two coils per phase

in parallel. Ideally, there would be no imbalance between back-EMFs of two parallel coils, causing the circulating current (denoted by $i_1 - i_2$) to be zero. However, if there are any differences in the two back-EMFs, coupled with low reactance characteristics of the topology, a significant circulating current would be created within the parallel pair.

In the following sections, an analytical field model used to analyze the effect of manufacturing tolerances on the motor will be detailed and compared against nonlinear FEA. The method will be tested against measurements from a low-field rotor spin test.

6.1 Analytical model

6.1.1 Rotor eccentricity

The model used for eccentricity analysis is shown in Fig. 6.3. The ideal physical air gap of the machine is 2.4 mm at rated speed (15000 rpm) with the balanced rotor. For static eccentricity, the stator center position is changed in the radial direction (l_e mm) and angle (θ_e deg). From Fig. 6.3, coil # 1 occupies the space that corresponds to $\theta = 3^\circ$ through 39° . As shown in the figure, when $\theta_e = 21^\circ$, the section denoted as coil # 1 has the least magnetic reluctance, whereas the section denoted coil # 6 has the biggest reluctance. The variance in physical air gap can be described as

$$l_g(\theta) = l_0 - l_e \cos(\theta - \theta_e), \quad (6.1)$$

where l_0 is the air gap without eccentricity (2.4 mm). The rotor eccentricity can also generate a phase shift in back-EMF of the parallel coils. The phase shift (in degrees) can be calculated as

$$P_{shift} = \frac{l_e \sin(\theta - \theta_e)}{2\pi\alpha/(p/2)} \times 360, \quad (6.2)$$

where α corresponds to inner radius of the rotor. The expression for varying air gap can be directly applied to the transfer model described in Chapter 4,

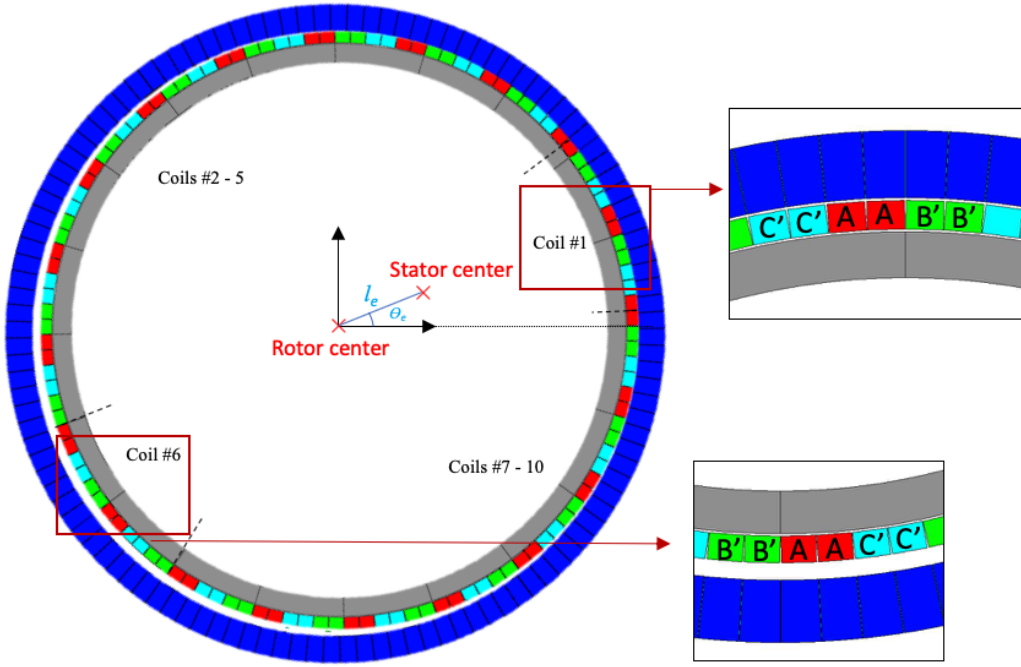


Figure 6.3: Eccentricity model with relevant parameters.

such that the outer radius of the yoke, γ , varies with θ ,

$$\gamma(\theta) = \gamma_0 - l_e \cos(\theta - \theta_e). \quad (6.3)$$

6.1.2 Circulating current

Because of the parallel connection between the coils, circulating current is generated due to eccentricity and fabrication tolerance. For example, the phasor voltage of each winding can be written as

$$V = ir - jX_L i \pm jX_M i_M + E, \quad (6.4)$$

where r , i_M , X_L and X_M refer to winding series resistance, mutual current, winding self-inductance, and mutual inductance, respectively. If we assume that the resistor voltage drop (ir) and the mutual voltage drop ($X_M i_M$) are small, then the following relationship between two parallel connected coils (coils # 1 and # 2, for example) can be found:

$$V_1 = V_2 \approx -jX_L i_1 + E_1 = -jX_L i_2 + E_2. \quad (6.5)$$

Thus, circulating current between them can be found as

$$i_1 - i_2 = \frac{(E_2 - E_1)}{jX_L}. \quad (6.6)$$

The above equation stresses the effect of unbalanced back-EMF between the coils. The influence of unbalanced back-EMF on circulating current is magnified by the low-reactance characteristic of the slotless topology [65]. While self-inductances across various windings are ideally uniform, they may also experience variation under eccentricity due to saturation.

6.1.3 Imbalanced winding

Apart from rotor eccentricity, another source of imbalance could arise from manufacturing tolerances of the stator windings. The coils of the discussed topology are manually pre-cast and are attached to the stator yoke with a ceramic filled resin for proper bonding and effective thermal transfer. This process can lead to nonuniform coil dimensions and spacing between the coils. The nonuniform spacing may cause variation in coil inductance. Such nonuniformity can be modeled by varying the arc angle between the coils, as shown in Fig. 6.4. As seen in the figure, each winding block occupies 2.82° and has an ideal gap of 0.18° between the blocks. The maximum range of movement between adjacent windings is set from -0.18° to 0.18° .

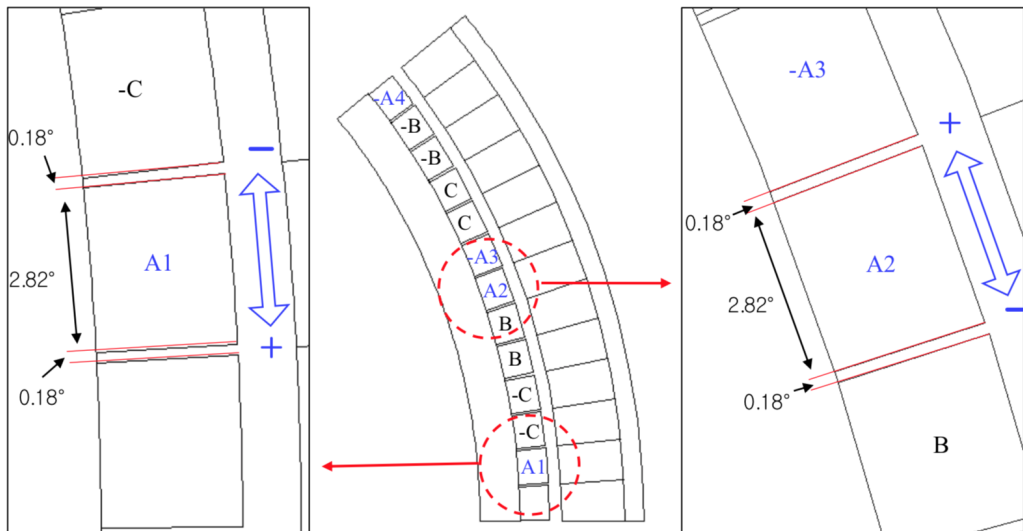


Figure 6.4: Coil nonuniformity model.

To obtain the effect of nonuniformity on inductance, transfer relations from Chapter 4 can be utilized. Following a typical method to calculate the inductance under unsaturated conditions, 1 A of current is injected into a single coil, while 0 A is enforced in all other coils. Fields from the magnets are neglected in this case. Fig. 6.5 (top) shows the input to the transfer relation model that corresponds to 1 A input with three turns. The resulting magnetic field at the coil surface is shown in Fig. 6.5 (bottom). The field result is consistent with that of FEA.

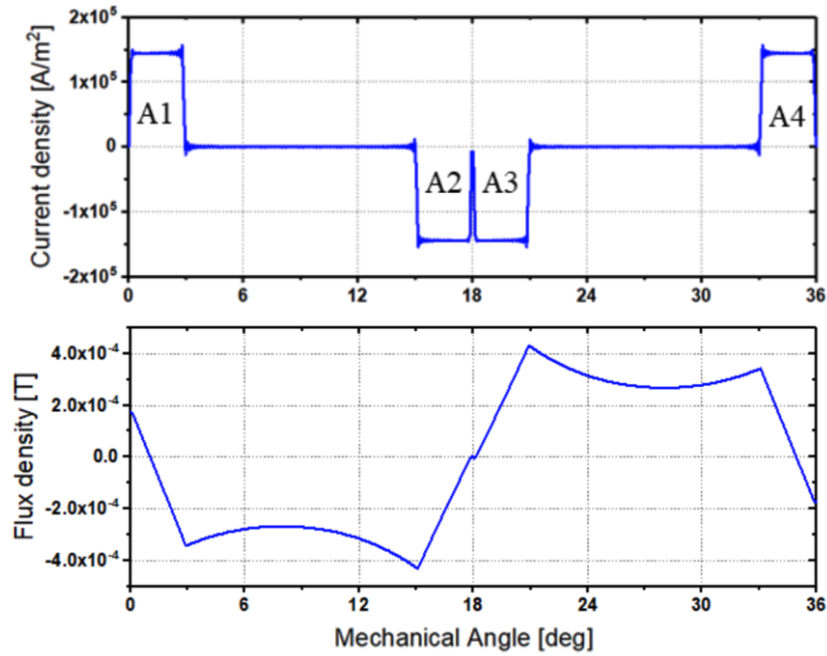


Figure 6.5: Current density distribution (top) and flux density waveform at coil surface due to coil excitation (bottom) using transfer relation.

However, the gap of 0.18° between the windings is small and thus impossible to implement using the transfer relations. The model uses the Fourier transform of the current density distribution, and is found to be insensitive to such a small gap. Therefore, inductances due to imbalanced windings are calculated only by changing the flux linkage area.

6.2 Analytical results and comparison

6.2.1 Back-EMF due to rotor eccentricity

For the analysis of no-load flux density distribution with eccentricity, $l_e = 0.6$ mm and $\theta_e = 21^\circ$ are chosen arbitrarily. In Fig. 6.6, the impact of eccentricity on field distribution is highlighted. Without eccentricity, the flux density in the stator yoke shows a uniform peak of 1.35 T in each pole, as designed. However, with eccentricity of just 0.6 mm, the highest flux density near coil #1 is observed to be 1.41 T, a 4.5% increase from the no-eccentricity case. The flux density in the vicinity of coil #6 shows a 7.4% decrease.

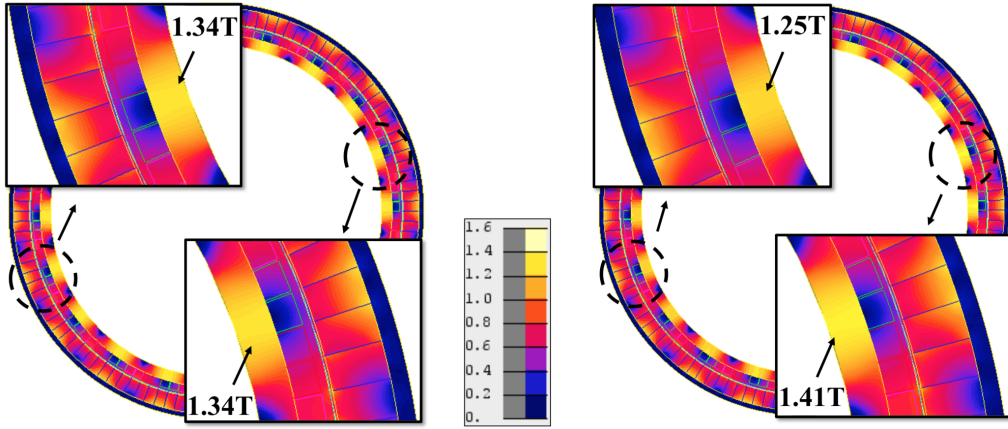


Figure 6.6: Flux density distribution of 1MW motor with no eccentricity (left) and eccentricity of $l_e = 0.6$ mm and $\theta_e = 21^\circ$ (right).

The impact of eccentricity on the back-EMF waveform is obtained using the transfer relation (as described in Chapter 4) and Faraday's law of induction. The results are shown in Fig. 6.7 and Table 6.1, and are shown to be very similar to the results obtained from FEA. As expected, coil #1 has the largest back-EMF of $502 V_{pk}$ while coil #6 has the lowest back-EMF of $462 V_{pk}$. The error in magnitude between the analytical model and FEA is at most 0.2%. As for phase shift, coils #3 and #4 have the largest leading angle, and coils #8 and #9 have the largest lagging angle, as expected, while coils #1 and #6 have no phase shift.

Fig. 6.8 shows the impact of varied l_e and θ_e on the magnitude of the back-EMFs among the coils. Shown in the left plot of Fig. 6.8 is the change of back-EMF magnitude from varying l_e when the angle is fixed at $\theta_e =$

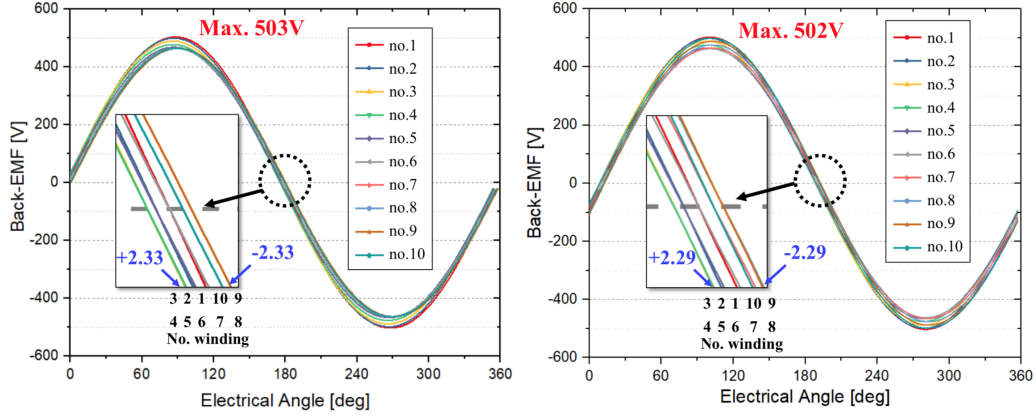


Figure 6.7: Back-EMF waveform of phase A with eccentricity of $l_e = 0.6$ mm and $\theta_e = 21^\circ$ obtained from analytical model (left) and non-linear FEA (right).

Table 6.1: Back-EMF results of analytical model and FEA

| Coil # | 1 | 2 | 3 | 4 | 5 | 6 | 7 | 8 | 9 | 10 |
|-----------------------------|-----|--------|-------|-------|-------|-----|-------|-------|-------|-------|
| V_{peak} (Analytical) | 503 | 499 | 489 | 477 | 467 | 463 | 467 | 477 | 489 | 499 |
| V_{peak} (FEA) | 502 | 499 | 488 | 476 | 466 | 462 | 466 | 476 | 488 | 499 |
| P_{shift} (Analytical) | 0 | +1.44 | +2.33 | +2.33 | +1.44 | 0 | -1.44 | -2.33 | -2.33 | -1.44 |
| P_{shift} (FEA) | 0 | + 1.41 | +2.29 | +2.30 | +1.43 | 0 | -1.43 | -2.30 | -2.29 | -1.41 |

21° , denoted as a percentage of the baseline back-EMF of $340.8 V_{rms}$. As mentioned, the back-EMFs of two opposite winding pairs are symmetrical. When the radial distance is increased, the value of the back-EMF is observed to increase or decrease linearly. In an extreme case of $l_e = 1.8$ mm, the back-EMF of coil #1 increases by 11.25% and the back-EMF of coil #6 decreases by 11.91%. Shown in the right plot of Fig. 6.8 is the change of back-EMF magnitude from varying θ_e while the distance is fixed at $l_e = 0.6$ mm. In this case, the back-EMF distributions are bilaterally symmetric around the axis at $\theta_e = 21^\circ$. Within the range of θ_e shown, coil #1 still demonstrates the largest back-EMF magnitude, while coil #6 demonstrates the smallest back-EMF magnitude. Back-EMF of coil #1 and coil #6 vary between 104.06% and 104.27%, and 95.88% and 96.08%, respectively. With bigger l_e , the variation is expected to be greater. Once θ_e exceeds 39° , the smallest air gap lies within the vicinity of coil #2, and the back-EMF of coil #2 will have the

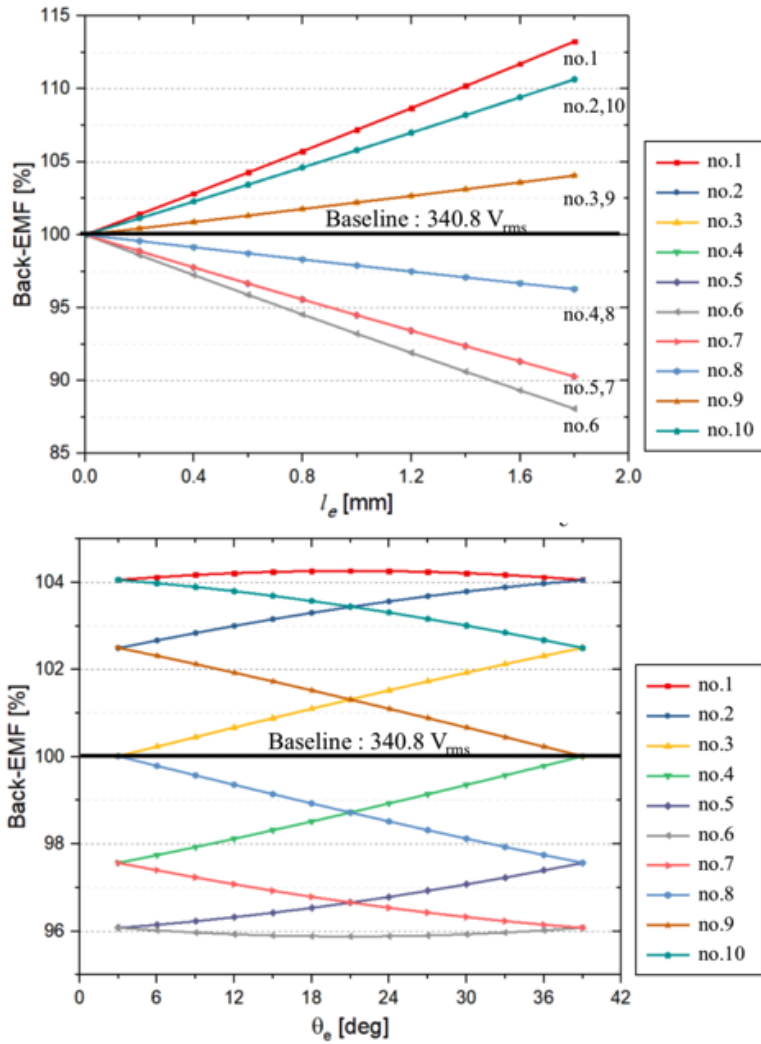


Figure 6.8: Back-EMF magnitude versus radial distance (top) and circumferential angle of eccentricity (bottom).

largest magnitude, with a maximum at $\theta_e = 57^\circ$.

6.2.2 Circulating current due to rotor eccentricity

Considering that the magnitude of circulating current in the parallel-connected coils is mainly determined by imbalance in back-EMF, proper choices in drive-motor connection can be employed. Two cases are highlighted in this subsection, where five inverters are used to drive the motor. In one case, each inverter is connected to two coils that are adjacent to each other. In

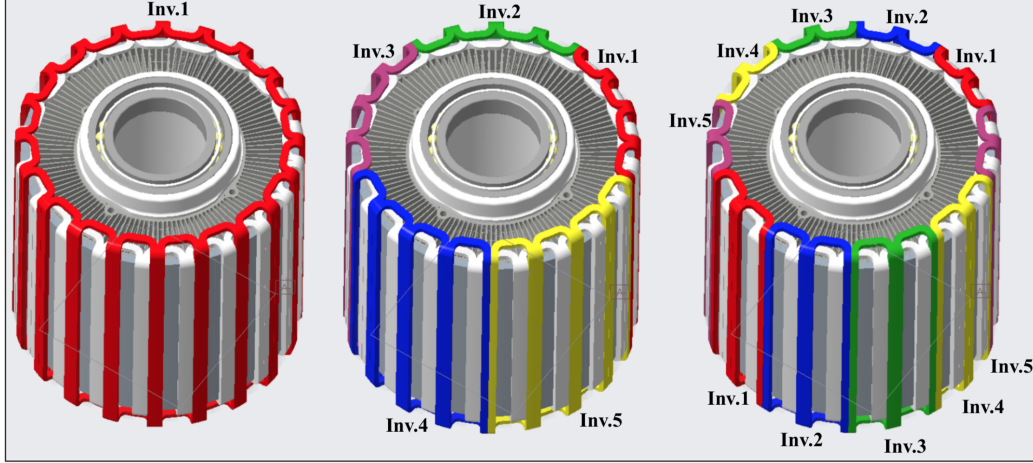


Figure 6.9: Configuration according to the winding method and inverter number.

the other case, each inverter is connected to two coils that are opposite of each other. The two cases, along with a “control” case of one (instead of five) inverter, are visualized in Fig. 6.9. Fig. 6.10 shows the magnitude of circulating current in each of the cases, with $l_e = 0.6$ mm and $\theta_e = 21^\circ$. The rated current is also marked in the figure. Coils with current magnitude that is farther away from the rated value of $93 A_{rms}$ can be interpreted as having higher circulating current. While the difference in magnitude of back-EMF between the coils causes circulating current in each of the coils, the effect is amplified by phase difference as well. As expected, having all coils connected in parallel (Case I) displays the biggest circulating current magnitude, where a maximum of 69% increase over the rated value is observed. At first glance, Case III seems most ideal, because coils #1 and #6 have no phase difference, as evidenced by the current magnitudes shown for the coils. However, this connection topology also couples coils #9 and #4, which have the largest phase difference, leading to a maximum current magnitude of 65% over the rated current. Case II connects two adjacent coils in parallel and thus minimizes the phase difference in back-EMF. Consequently, only a 32% increase over the rated coil current is observed. Case II is therefore the best drive-motor connection method for the 1 MW motor. Note that utilizing 10 inverters and having no coils in parallel would completely eliminate the circulating current issue.

One method to reduce circulating currents is to use ungrounded neutrals

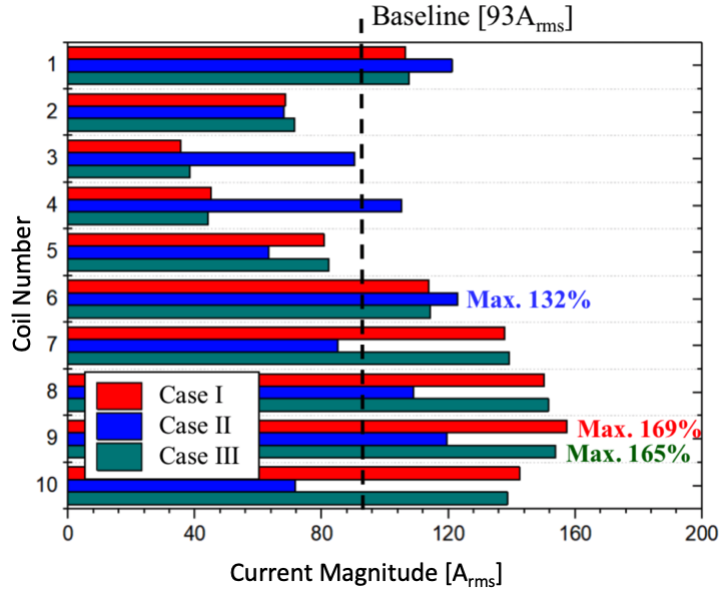


Figure 6.10: Coil current for different drive-motor connections.

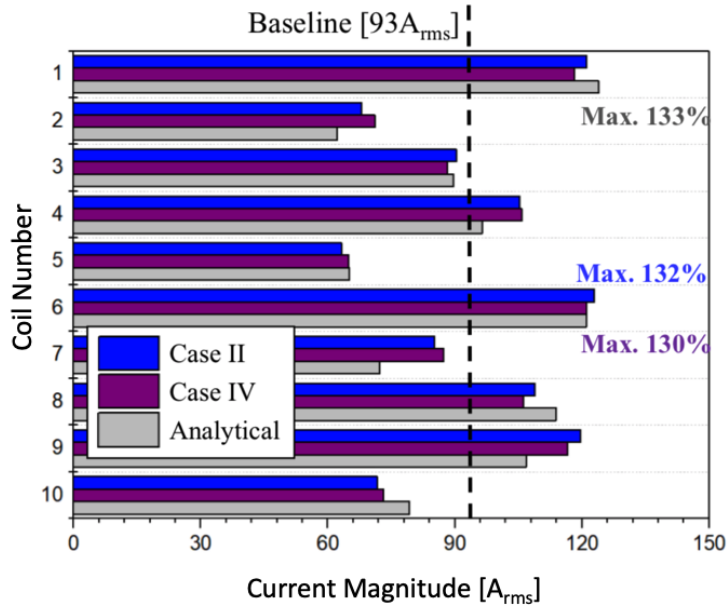


Figure 6.11: Comparison between grounding and non-grounding.

between the two parallel windings of each inverter. The differences in neutral point voltage are analyzed and the effects on circulating current magnitude are shown in Fig. 6.11, where Case IV corresponds to a case where neutrals of the paralleled coils are connected to the inverter.

The results show that while the overall trend of Case IV is similar to that

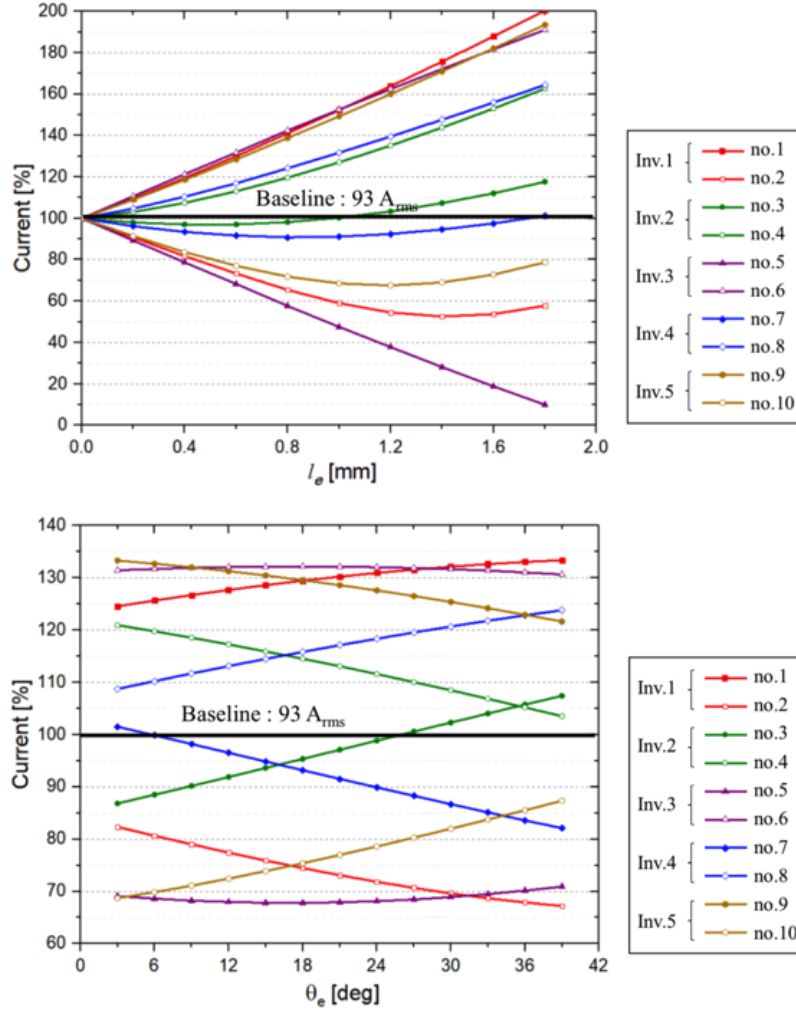


Figure 6.12: Coil current magnitude versus radial distance (top) and circumferential angle of eccentricity (bottom).

of Case II, the maximum circulating current for Case IV is reduced by 2%. An analytical model is also used to compare against Case IV, where an error is observed. That can be attributed to the fact that the analytical model does not take saturation into account. While the 2% improvement does not seem substantial, the effect on copper losses (which is proportional to current squared) can be bigger. For example, a 2% improvement in magnitude of circulating current corresponds to 3% improvement in dc copper losses. Thus, Case IV (with neutral grounding) is thought to be a good option to alleviate circulating current issues.

The effects of varying l_e and θ_e for Case IV are shown in Fig. 6.12. Note that the effect of saturation is more magnified in the current analysis due to

low reactance and presence of load. For varying l_e , the circulating current of coil #1 is increased by 86.37% while a reduction of 90.73% is observed for coil #5. For varying θ_e , coil #6 has the largest circulating current at $\theta_e = 21^\circ$, but no longer the largest as the angle is increased. This is due to the phase shift of the circulating current. Note that the scalar sum of the circulating current at the two connected parallel windings is higher than that of the baseline model because of phase shift.

6.2.3 Inductance due to imbalanced winding

Inductance is calculated using both an analytical model and FEA, and is shown in Fig. 6.13. Similar to the analytical model, an unsaturated core was used for FEA simulations with a current density distribution corresponding to that shown in Fig. 6.5. Results show that the inductance obtained from the analytical model has an error of 0.2% at a shift angle of zero. In any case, the increase or decrease in overall inductance of the coil with varying gap width is within $\pm 1.25\%$ according to the analytical model and 1.03% according to FEA. From the inductance measurements shown in Table 6.2,

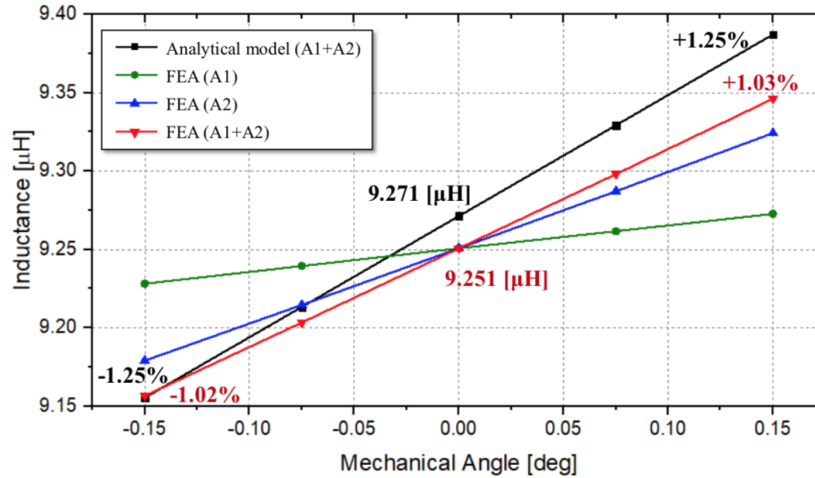


Figure 6.13: Self-inductance of a single coil.

the average inductances of different three phases are observed to be consistently higher than the expected values, due to effect of end windings. Note that the effect of longer end windings for phases B and C is observed in the form of higher inductances. While there is a non-negligible error between the experimental measurements and FEA, the percentage errors between the

Table 6.2: Lab measurements for coil self-inductance values (μH)

| Coil # | Phase A | Phase B | Phase C |
|---------|---------|---------|---------|
| 1 | 11.110 | 11.058 | 11.332 |
| 2 | 11.078 | 11.084 | 11.396 |
| 3 | 11.151 | 11.148 | 11.338 |
| 4 | 11.158 | 11.160 | 11.384 |
| 5 | 11.121 | 11.193 | 11.393 |
| 6 | 11.079 | 11.161 | 11.376 |
| 7 | 11.108 | 11.153 | 11.269 |
| 8 | 11.006 | 11.102 | 11.438 |
| 9 | 11.105 | 11.177 | 11.359 |
| 10 | 11.097 | 11.113 | 11.318 |
| Average | 11.101 | 11.135 | 11.360 |

measured inductances and their average values are well within the expected worst cases hypothesized by the study, as shown in Fig. 6.14.

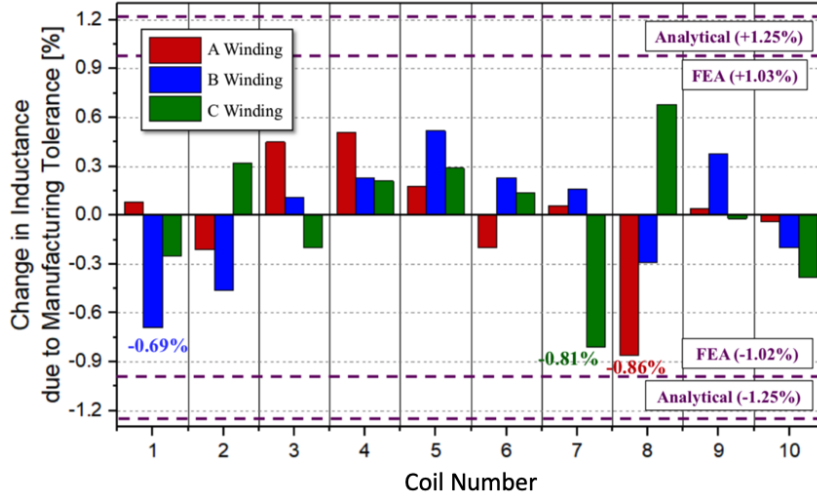


Figure 6.14: Inductance variance comparison between simulation and measurements.

6.3 Experimental validation with low-field rotor

To experimentally validate the rotor eccentricity model and its effect on the back-EMF, a low-field motor was manufactured. The low-field rotor, as shown in Fig. 6.15, consists of two rectangular magnets per pole, along with

a thin rotor yoke and a non-magnetic support structure. Table 6.3 shows the key dimensions and specifications. The motor is rated to spin safely at 300 rpm.

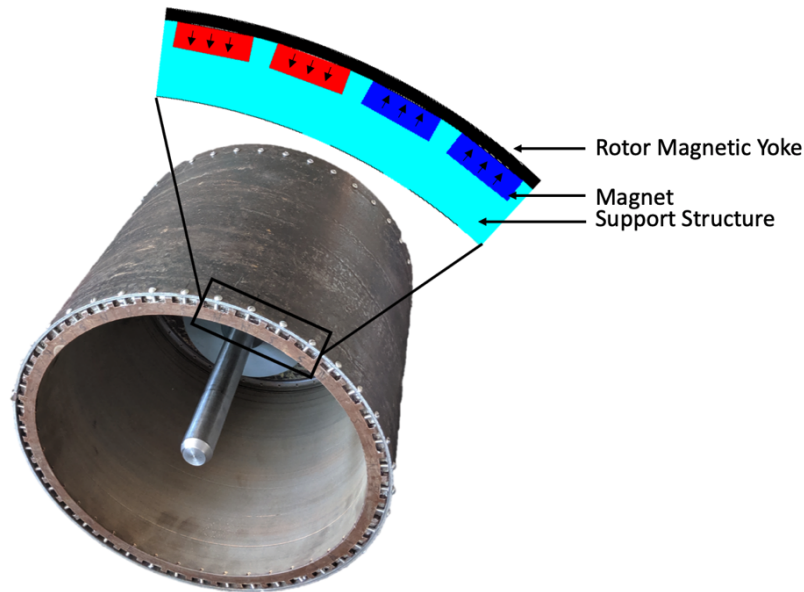


Figure 6.15: Low-field rotor hardware and FEA model. A pole pair is shown.

Table 6.3: Low-field rotor dimensions and specification

| | |
|------------------------------|----------|
| Outer diameter | 329.4 mm |
| Magnet height | 6.35 mm |
| Magnet width | 19.1 mm |
| Yoke thickness | 2.95 mm |
| Yoke saturation flux density | 1.7T |
| Magnet remnant flux density | 1.32T |

6.3.1 Air gap field and back-EMF model

The field model based on the transfer relation in Chapter 4 was specifically developed for a Halbach array and does not consider the presence of a rotor yoke. The low-field rotor described in the previous subsection includes a rotor yoke and the model must be re-formulated. The appropriate model is shown in Fig. 6.16.

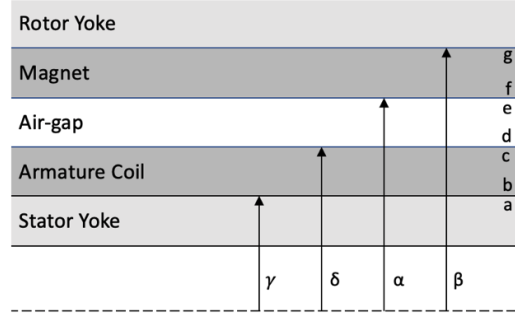


Figure 6.16: Analytical model for field estimation including the rotor yoke.

To include the presence of a rotor yoke in the transfer relation model, a boundary condition of $B_\theta^b = 0$ needs to be included. Applying the two boundary conditions to the transfer relation, the vector potential at boundary e can be obtained as

$$A_{z,n}^e = \frac{\frac{1}{\mu_r} M_s \left[\frac{G_o(\alpha,\beta)}{F_o(\alpha,\beta)} Y_s - X_s \right]}{\frac{1}{\mu_r} \frac{G_o(\alpha,\beta)G_o(\beta,\alpha)}{F_o(\alpha,\beta)} - \frac{G_o(\alpha,\gamma)G_o(\gamma,\alpha)}{F_o(\alpha,\gamma)} + F_o(\gamma,\alpha) - \frac{1}{\mu_r} F_o(\beta,\alpha)}. \quad (6.7)$$

From the vector potential solution at boundary e, vector potentials at boundaries b and g, and thus radial flux densities at those boundaries, can be obtained. It must be noted, however, that this transfer relation is derived in a cylindrical coordinate system. As shown in Fig. 6.17, if the magnet is arc-shaped and magnetized radially inward or outward, the radial magnetization vector will resemble a square wave, while the tangential magnetization is zero. However, in the case of the low-field rotor, rectangular magnets with magnetization vector normal to the magnet surface were employed. To accurately obtain the field from such magnets and magnetization using the transfer relation model, radial and tangential magnetization vectors in the model should be in the form shown in Fig. 6.17. More specifically, the top part of the square wave is replaced with a curve described by a sine function. Furthermore, a nonzero, sinusoidal wave models the tangential magnetization vector.

Following this method, the magnetization vector for the low-field rotor can be modeled as shown in Fig. 6.18, and the resulting air gap field can be found as in Fig. 6.19. The results show that the normal magnetization model matches FEA well, while the radial magnetization model displays error. This demonstrates that even rectangular magnets with magnetization normal to

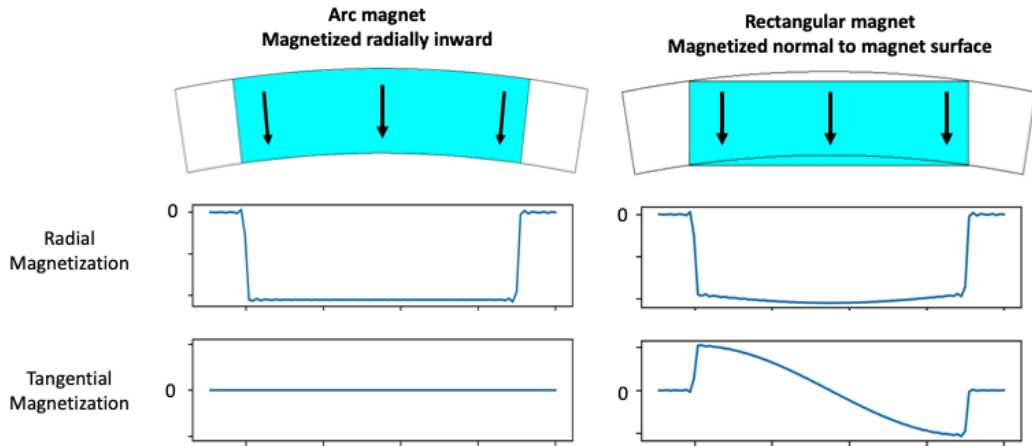


Figure 6.17: Magnetization vector shape comparison between two different magnet shapes and magnetization direction.

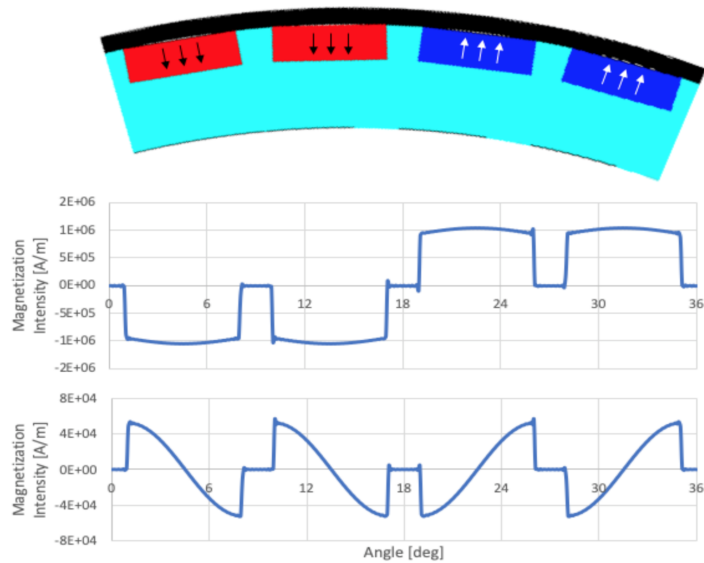


Figure 6.18: Magnetization vector for the low-field rotor (one pole pair shown).

the magnet surface can be successfully modeled using the transfer relation model with a cylindrical coordinate system.

The back-EMF waveform can be found by computing the time derivative of the flux linkage. While the air gap flux density of the 1 MW Halbach array is highly sinusoidal, the low-field rotor contains a non-negligible third-harmonic, even at the surface of the stator yoke. Thus, the fundamental and third harmonic content should be extracted from the field, and contributions from each to back-EMF must be considered separately. The back-EMF can

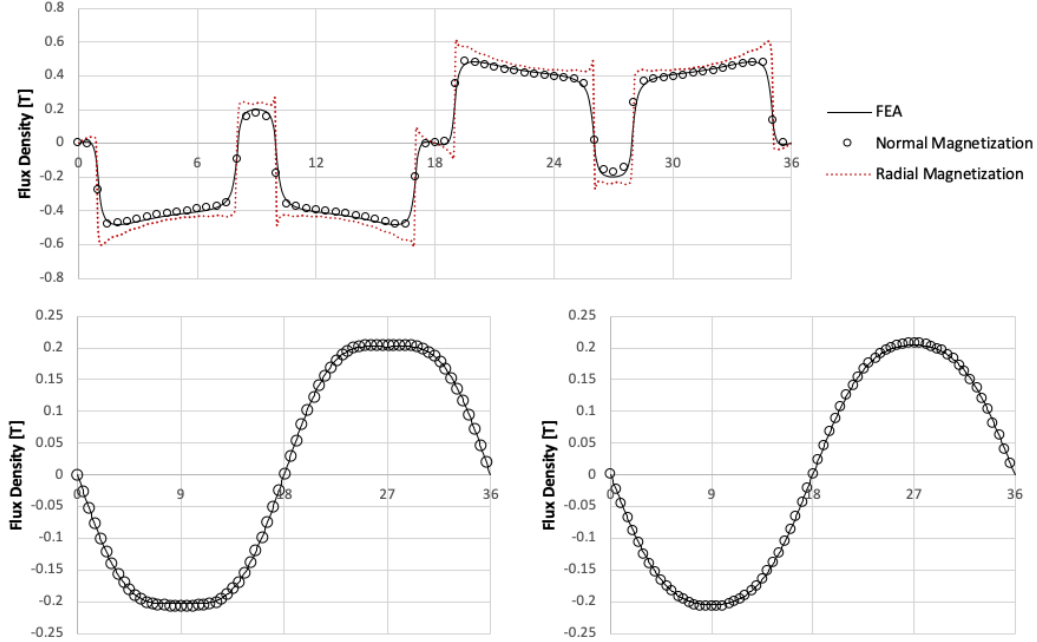


Figure 6.19: Comparison between air gap field from FEA and analytical model (normal magnetization model at magnet surface with radial magnetization model overlaid (top), air gap field (bottom-left), and field at stator yoke surface (bottom-right)). Note that the fields are obtained with no eccentricity modeled ($l_e = 0$).

be found as

$$E = \sum_{n=1,3} k_{w,n} \frac{d\lambda_n}{dt}, \quad (6.8)$$

where $k_{w,n}$ refers to the widely known winding factor and can be calculated from formulae shown in multiple sources [31, 66].

One important fact to consider for the analytical model is that saturation is not considered. To tune the analytical model to fit a saturated scenario, the field from the low-field rotor is obtained at the air gap, without the stator mounted, using a Gauss meter. The results are compared against FEA for the same scenario with $B_{sat}=1.7$ T in the rotor and the analytical model, and are shown in Fig. 6.20. As expected, because the analytical model neglects saturation, the field obtained from it is observed to be higher. To tune the model to correct for saturation, a factor of 85% is imposed on the analytical model in the following analyses.

Once a saturation factor is included, a more accurate back-EMF waveform can be computed. Fig. 6.21 shows good agreement between back-EMF

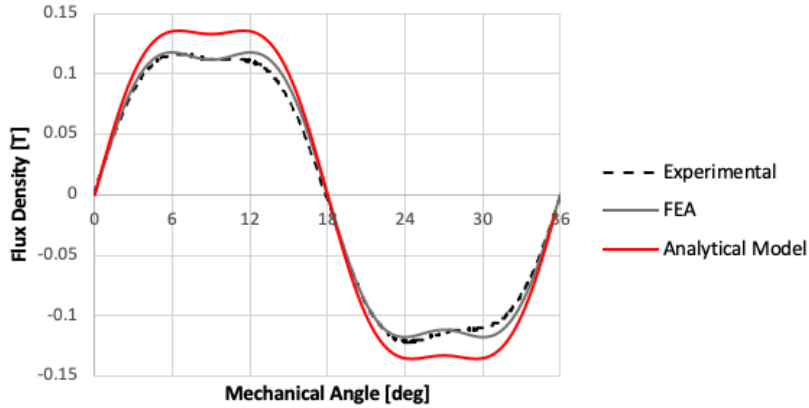


Figure 6.20: Field comparison among FEA, analytical model, and experimental measurements.

obtained from FEA and calculated back-EMF from fundamental and third harmonic content of the air gap flux density. This assumes 300 rpm.

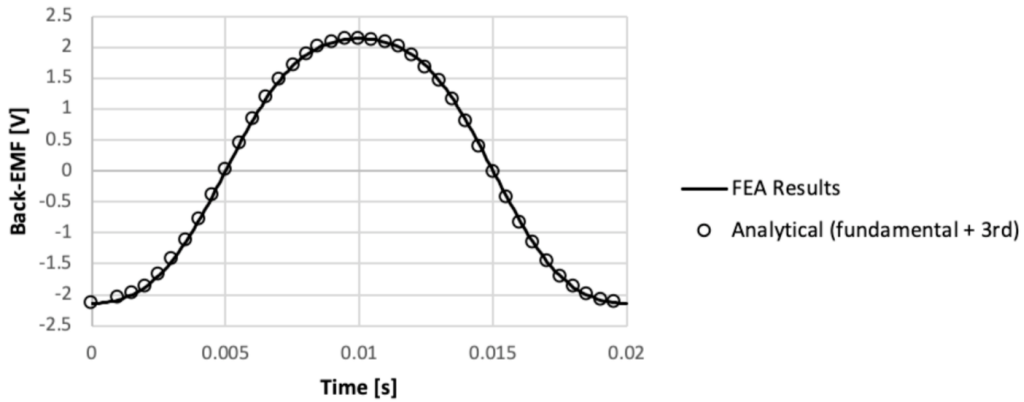


Figure 6.21: Back-EMF estimation comparison with FEA (no eccentricity).

6.3.2 Rotor eccentricity model

To obtain measurements from the lab, the low-field rotor was mounted to the stator and spun at 300 rpm. Raw data was collected using voltage probes, and sample data for a single phase are shown in Fig. 6.22. While the back-EMF measurements seem to be in phase with identical magnitudes, a more careful look reveals that rotor eccentricity may be present. Note that measurements for coils #4 and #7 are repeated to provide reference to account for measurement error between runs.

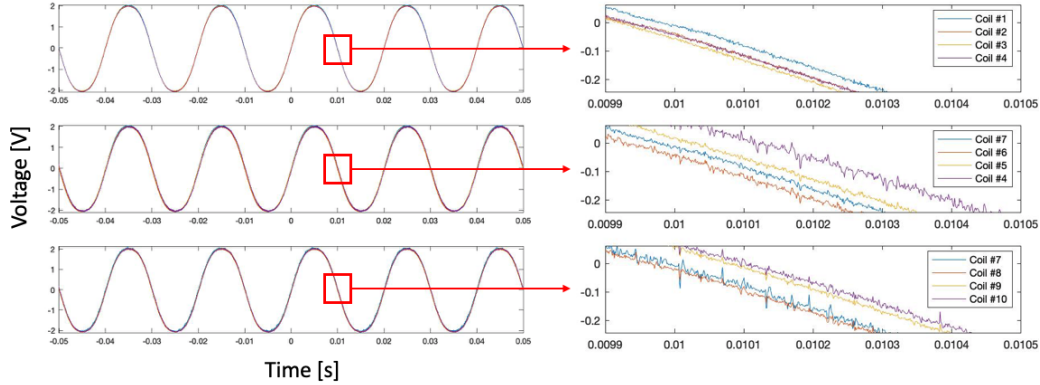


Figure 6.22: Raw back-EMF measurement data obtained from experiment.

To effectively compare the waveforms, a Fourier transform was performed on each waveform, assuming that the only major components of the back-EMF waveform are fundamental and third harmonics. Amplitudes of the harmonic waveform and the phase information were obtained and normalized using the repeated measurements for coil #4 and coil #7. In Fig. 6.23, the fundamental magnitudes are compared between the coils. While the plotted data from the top row seems irregular, plots on the bottom row clearly display rotor eccentricity. It is worth noting that back-EMF magnitudes display similar behavior among the phases. Note that phases are referred to as Y, B, and R to match the yellow, blue, and red markings assigned during winding assembly.

To compare the rotor eccentricity model with the experimental values, all phases were normalized to a single phase (i.e. phase Y) and plotted on a single polar graph. Generally, each coil should be shifted by a mechanical angle of $120^\circ \times 1/(P/2)$ (which corresponds to 12° for a 20 pole motor). However, during the process of assembling the coils to the stator yoke, the polarity of phase B was flipped and thus the magnetic axis of each phase B coil is mechanically 6° away from adjacent coils. Note that this has no effect on the performance of the motor.

Fig. 6.24 shows the comparison between back-EMF fundamental magnitude obtained via experiment and analytical model. The results from the analytical model were obtained by setting $l_e = 0.11$ mm and $\theta_e = 30^\circ$. Note that for this model, $\theta_e = 0^\circ$ is set to point to coil R10. Thus, $\theta_e = 30^\circ$ points to coil B9. While the factor of 85% to account for saturation resulted in accurate back-EMF results when compared to FEA (refer to Fig. 6.21), an

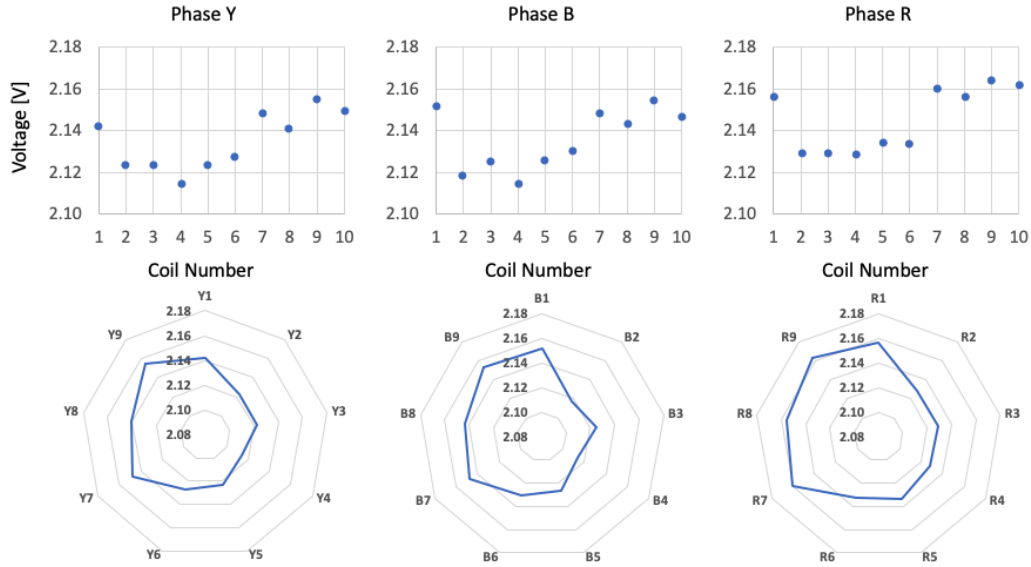


Figure 6.23: Comparison of fundamental component magnitude of back-EMF for different coils.

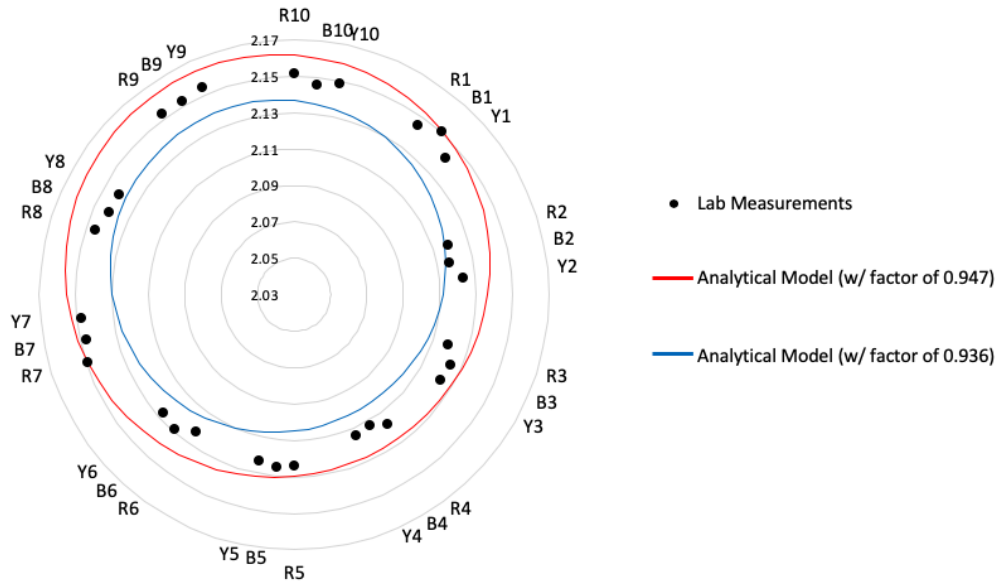


Figure 6.24: Comparison between back-EMF from experiment and analytical model. Result is obtained using $l_e = 0.11$ mm and $\theta_e = 30^\circ$.

error is observed when compared to the measurements (5.3-6.5%). Furthermore, slight variation between the measurements was observed. Ideally, the measurements should form an off-centered circle, as observed in results from the analytical models. However, offsets are observed in some measurements. While this can be attributed to measurement error, another possibility could

be imbalanced windings. If the spacings are irregular (refer to Fig. 6.4), back-EMF could vary by $\pm 4\%$. Taking into account small inductance variations from measurements, we can deduce that we can allow a $\pm 1\%$ variation in the back-EMF magnitudes.

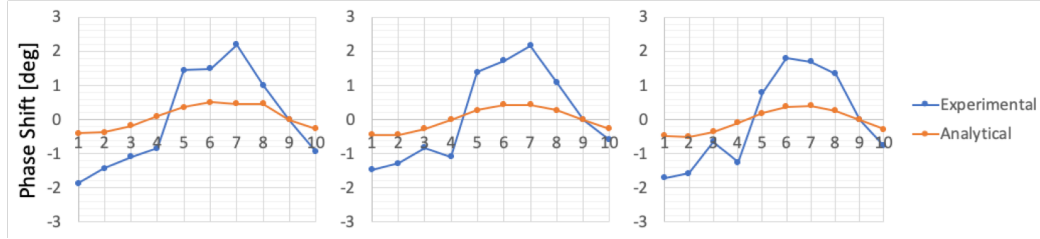


Figure 6.25: Comparison between back-EMF phase shift from experiment and analytical model for $l_e = 0.11$ mm and $\theta_e = 30^\circ$. (Phases Y, B, and R are shown left to right.)

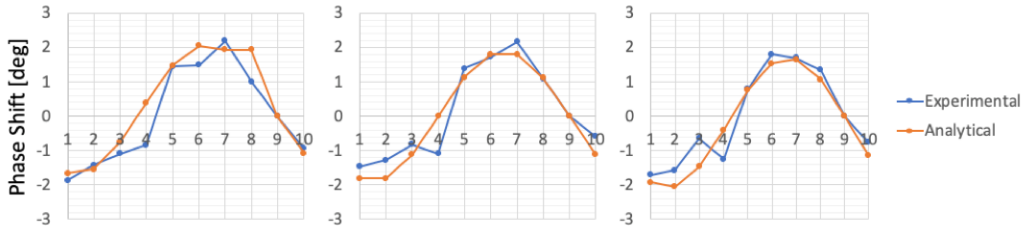


Figure 6.26: Comparison between back-EMF phase shift from experiment and analytical model for $l_e = 0.45$ mm and $\theta_e = 30^\circ$. (Phases Y, B, and R are shown left to right.)

From the recorded measurements and Fourier transform results, phase shift information can be extracted and compared with the eccentricity model, as shown in Equation (6.2). In Fig. 6.25, results obtained using $l_e = 0.11$ mm and $\theta_e = 30^\circ$ are compared with the experimental values. Note that coil #9 for each phase is set to be zero as the reference. While there exists a significant error, the general trend of phase shift angle from coil to coil is observed to match. For example, with coils #9 as references (since it is hypothesized that $\theta_e = 30^\circ$), symmetry dictates that phase shift should be close to zero between coils #3 and #5 for each phase.

If l_e is increased to 0.45 mm for the analytical model, the resulting phase shift matches that of the experiment well, as shown in Fig. 6.26. However, from Fig. 6.27, it is apparent that $l_e = 0.45$ mm is not consistent with the magnitude of the back-EMF. With these results, we can deduce that rotor

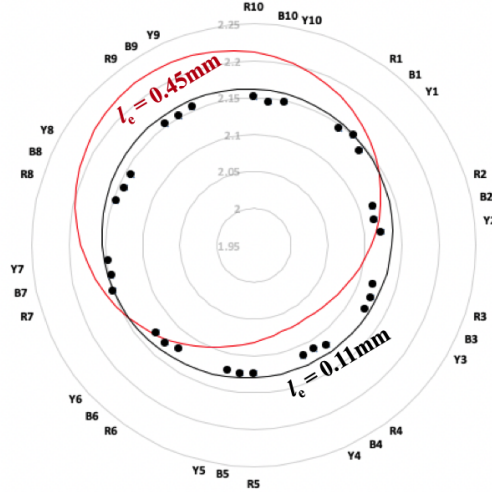


Figure 6.27: Comparison between back-EMF from experiment and analytical model. θ_e is fixed at 30° . Cases with both $l_e = 0.11$ mm and $l_e = 0.45$ mm are shown.

static eccentricity alone cannot accurately predict the phase angles. Another cause of the non-negligible error in phase shift angle could be imbalanced windings. Considering that 0.18° of mechanical angle shift corresponds to 1.8° of electrical angle for this 20 pole machine, we can explain the inconsistencies between the model and the measurements with misaligned coils. This seems likely because the error bound shown in Fig. 6.25 is at most 1.7° , which is within the range of movement for the coil blocks. This phenomenon is illustrated in Fig. 6.28. In the left figure, the coil magnetic axis and the rotor direct axis are aligned and all coil back-EMFs would be in phase. In case any misalignment occurs even without variations in coil dimensions, we expect a phase shift between the back-EMFs. The 1.7° shift between the eccentricity case of $l_e = 0.11$ mm and the experimental measurements corresponds to a 16 mil-wide misalignment.

With this information, we can expect there to be circulating current in this armature even with no eccentricity. To examine this case, the measured back-EMF magnitudes and phase angle measurements were corrected for eccentricity using the model. From Fig. 6.29, the blue lines show the no-eccentricity case for the armature, whereas the grey line shows the eccentricity case of $l_e = 0.11$ mm.

Fig. 6.30 shows the expected currents in the coils, where circulating currents are clearly observed for both cases. The largest circulating current

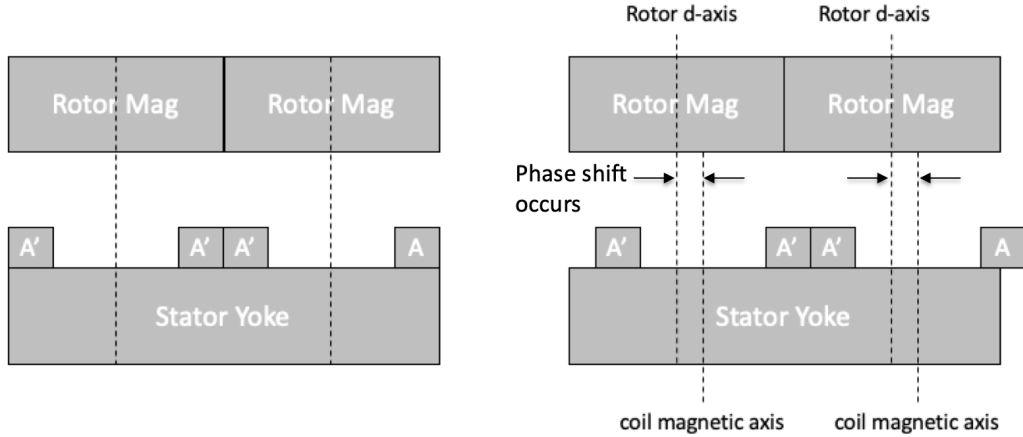


Figure 6.28: Coil misalignment causing phase shift in back-EMF waveforms between coils even without eccentricity. Ideal case (left) and misaligned case (right).

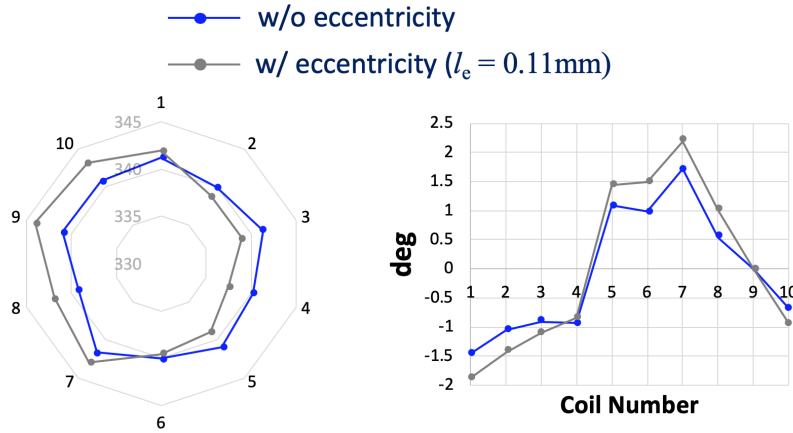


Figure 6.29: Back-EMF magnitude (left) and phase angle (right) for cases with and without eccentricity. The case with eccentricity corresponds to experimentally obtained data. The case without eccentricity is obtained by using the analytical model to correct for eccentricity.

of 22% is observed for the coil #7 and #8 pair, which is also observed to have the biggest phase difference (approximately 1.2°). The case where the circulating current is only 8% of the rated current corresponds to an offset of about 5 mils between the coils. If tolerance of 5 mils can be achieved (which is what stator laminations typically have) when manufacturing and assembling the coils, we can limit the amount of circulating current to about 8%.

Since phase shift in the back-EMF is closely associated with circulating

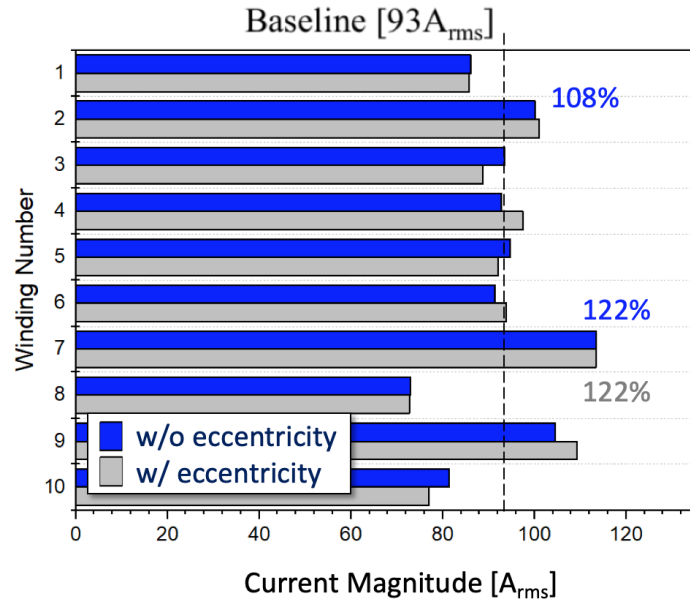


Figure 6.30: Expected current magnitudes in the coils.

currents (as discussed in Section 6.2.2), it can be concluded that imbalanced spacing between coils can greatly affect the magnitude of the circulating current, even without rotor eccentricity.

CHAPTER 7

CONCLUSION

In this dissertation, a high-frequency, slotless permanent magnet synchronous motor was discussed for its benefit in volume and weight reduction.

In Chapter 2, it has been shown that high fundamental frequency and high tip speed allow significant weight reduction. The scalability of this benefit in specific power across various sizes and rotational speed was also introduced.

In Chapter 3, further methods to accommodate high frequency and high tip speed were discussed. Slotless topology eliminates stator teeth and associated iron losses, and a Halbach array allows elimination of further iron from a design. Litz coils mitigate ac losses expected from the slotless topology. An outer rotor is utilized to accommodate the high rotor tip speed. An optimized 1 MW motor that incorporates all the discussed features was presented, along with detailed specifications. The motor is projected to meet the threshold for electric propulsion, with specific power of 13 kW/kg and full-load efficiency of 97.4%.

In Chapter 4, an analytical model based on a flux-potential transfer relation was presented. The results from the model compare well with the results from FEA. Field measurements from Halbach rotor assembly trials were utilized to validate the analytical model. When the analytical model is adjusted to account for manufacturing faults that were identified in the assembly trials, the model predicts the air gap field well. Efforts to characterize major losses (iron, copper, windage) for the topology were discussed.

In Chapter 5, the field and loss models, along with an evolutionary genetic algorithm, were used to compare the specific power between a conventional toothed topology and the slotless topology, where the benefits of the slotless topology at high frequencies were demonstrated. Characteristics of the slotless topology were further investigated to include its performance at various angular speeds. Weight benefits are evident even at lower angular speeds, as long as high tip speed is maintained. The study was extended to examine

the motor's integration with STARC-ABL. Three possible integration points were considered. An efficiency-weight tradeoff is observed for all three options to show that the direct drive, outer rotor motor and fan integration may be optimal. A suitable design was chosen along the Pareto front and first-order thermal and mechanical studies were performed to show that a 2.6 MW, 11 kW/kg propulsor motor with a 98% efficiency should be feasible.

In Chapter 6, a rotor eccentricity model and coil imbalance model were developed to investigate the effect of manufacturing tolerances on machine performance. A case of extreme static rotor eccentricity (0.6 mm) was investigated via the analytical model and FEA to show that circulating current up to 33% can exist. A coil imbalance model with measurement validation has shown that inductance variation is minimal and that the coils are manufactured with fairly consistent dimensions. A low-field rotor was manufactured for experimental validation of the model. Modifications to the field models were detailed to accommodate rectangular rotor magnets with magnetization direction normal to the magnet surfaces. The modified model was shown to predict the resulting airgap field well, when compared to FEA. Circulating current predictions for the 1 MW motor were improved based on experimental results. It was shown that misalignment of coils during assembly causes circulating current even without rotor eccentricity. The importance of manufacturing tolerance of armature coils was emphasized and tolerance guidelines to limit circulating current were set.

REFERENCES

- [1] International Air Transport Association, “Vision 2050,” 2011. [Online]. Available: https://www.iata.org/pressroom/facts_figures/Documents/vision-2050.pdf
- [2] European-Commission, “Reducing emissions from aviation,” May 2013. [Online]. Available: http://ec.europa.eu/clima/policies/transport/aviation/index_en.htm
- [3] B. Sarlioglu and C. T. Morris, “More electric aircraft: Review, challenges, and opportunities for commercial transport aircraft,” *IEEE Transactions on Transportation Electrification*, vol. 1, no. 1, pp. 54–64, June 2015.
- [4] W. Cao, B. C. Mecrow, G. J. Atkinson, J. W. Bennett, and D. J. Atkinson, “Overview of electric motor technologies used for more electric aircraft (MEA),” *IEEE Transactions on Industrial Electronics*, vol. 59, no. 9, pp. 3523–3531, Sept. 2012.
- [5] T. O’Connell, “Fundamentals of more electric aircraft design,” 2017, tutorial presented at the IEEE Transportation Electrification Conference (ITEC), Chicago, IL.
- [6] T. A. Burrell, S. L. Campbell, C. Coomer, C. W. Ayers, A. A. Wereszczak, J. P. Cunningham, L. D. Marlino, L. E. Seiber, and H.-T. Lin, “Evaluation of the 2010 Toyota Prius hybrid synergy drive system,” Oak Ridge National Lab. (ORNL), Oak Ridge, TN (United States). Power Electronics and Electric Machinery Research Facility, Tech. Rep., Mar. 2011.
- [7] S. G. Jayasinghe, L. Meegahapola, N. Fernando, Z. Jin, and J. M. Guerrero, “Review of ship microgrids: System architectures, storage technologies and power quality aspects,” *Inventions*, vol. 2, no. 1, 2017. [Online]. Available: <https://www.mdpi.com/2411-5134/2/1/4>
- [8] National Academies of Sciences, Engineering, and Medicine, *Commercial Aircraft Propulsion and Energy Systems Research: Reducing Global Carbon Emissions*. Washington, DC: The National Academies Press, 2016.

- [9] M. D. Hathaway, R. Del Rosario, and N. Madavan, "NASA fixed wing project propulsion research and technology development activities to reduce specific energy consumption," in *49th AIAA/ASME/SAE/ASEE Joint Propulsion Conference*, 2013, p. 3605.
- [10] G. V. Brown, "Efficient flight-weight electric systems," 2012, presented at the 5th Fundamanelal Aeronautics Program Technical Conf., Cleveland, OH.
- [11] M. Bradley and C. Droney, "Subsonic ultra green aircraft research phase II: N+4 advanced concept development," Boeing Research and Technology, Huntington Beach, Ca., Tech. Rep., 2012.
- [12] J. Felder, G. Brown, and H. Kim, "Turboelectric distributed propulsion in a hybrid wing body aircraft," in *20th International Society for Airbreathing Engines, ISABE-2011-1340, Gothenburg, Sweden*, 2011.
- [13] X. Zhang and K. S. Haran, "High-specific-power electric machines for electrified transportation applications-technology options," in *2016 IEEE Energy Conversion Congress and Exposition (ECCE)*, Sept. 2016, pp. 1–8.
- [14] R. Jansen, G. V. Brown, J. L. Felder, and K. P. Duffy, "Turboelectric aircraft drive key performance parameters and functional requirements," in *51st AIAA/SAE/ASEE Joint Propulsion Conference*, July 2015. [Online]. Available: <https://arc.aiaa.org/doi/abs/10.2514/6.2015-3890>
- [15] Siemens, "World-record electric motor for aircraft," 2015. [Online]. Available: <https://www.siemens.com/press/en/feature/2015/corporate/2015-03-electromotor.phpevent-toc-1>
- [16] R. DeRosario, "NASA fixed wing project: Green technologies for future aircraft generation," in *AIAA SciTech*, 2014.
- [17] D. J. Perreault, J. Hu, J. M. Rivas, Y. Han, O. Leitermann, R. C. N. Pilawa-Podgurski, A. Sagneri, and C. R. Sullivan, "Opportunities and challenges in very high frequency power conversion," in *2009 Twenty-Fourth Annual IEEE Applied Power Electronics Conference and Exposition*, Feb 2009, pp. 1–14.
- [18] P. A. Kyaw, A. L. F. Stein, and C. R. Sullivan, "Fundamental examination of multiple potential passive component technologies for future power electronics," *IEEE Transactions on Power Electronics*, vol. 33, no. 12, pp. 10 708–10 722, Dec. 2018.
- [19] A. J. Hanson, J. A. Belk, S. Lim, C. R. Sullivan, and D. J. Perreault, "Measurements and performance factor comparisons of magnetic materials at high frequency," *IEEE Transactions on Power Electronics*, vol. 31, no. 11, pp. 7909–7925, Nov. 2016.

- [20] W. G. Odendaal and J. A. Ferreira, "Effects of scaling high-frequency transformer parameters," *IEEE Transactions on Industry Applications*, vol. 35, no. 4, pp. 932–940, July 1999.
- [21] A. Yoon, X. Yi, J. Martin, Y. Chen, and K. Haran, "A high-speed, high-frequency, air-core PM machine for aircraft application," in *2016 IEEE Power and Energy Conference at Illinois (PECI)*, Feb. 2016, pp. 1–4.
- [22] X. Yi, A. Yoon, and K. S. Haran, "Multi-physics optimization for high-frequency air-core permanent-magnet motor of aircraft application," in *2017 IEEE International Electric Machines and Drives Conference (IEMDC)*, May 2017, pp. 1–8.
- [23] J. Martin, A. Yoon, A. Jin, and K. S. Haran, "High-frequency Litz air-gap windings for high-power density electrical machines," *Electric Power Components and Systems*, vol. 45, no. 7, pp. 798–805, 2017. [Online]. Available: <https://doi.org/10.1080/15325008.2017.1310951>
- [24] R. Sanchez, A. Yoon, X. Yi, L. Zheng, Y. Chen, K. S. Haran, A. Provenza, and J. Veres, "Mechanical validation of a high power density external cantilevered rotor," *IEEE Transactions on Industry Applications*, vol. 54, no. 4, pp. 3208–3216, July 2018.
- [25] A. Yoon and K. Haran, "High frequency electric machines for boundary layer ingestion fan propulsor," in *AIAA/IEEE Electric Aircraft Technologies Symposium*, 2018.
- [26] A. K. Yoon, J. Xiao, D. Lohan, F. Arastu, and K. S. Haran, "High frequency electric machines for boundary layer ingestion fan propulsor," *IEEE Transactions on Energy Conversion*, pp. 1–1, 2019.
- [27] D. Lee, A. Yoon, S. Sirimanna, S. Salon, and K. Haran, "Impact of manufacturing tolerances on a low-reactance slotless PM synchronous machine," *IEEE Transactions on Energy Conversion*, pp. 1–1, 2019.
- [28] A. Yoon, Y. Wang, A. Anderson, D. Lee, and K. Haran, "Experimental validation of rotor eccentricity model of a slotless pm synchronous machine," in *AIAA/IEEE Electric Aircraft Technologies Symposium. Indianapolis, IN.*, 2019.
- [29] T. Finken, M. Felden, and K. Hameyer, "Comparison and design of different electrical machine types regarding their applicability in hybrid electrical vehicles," in *2008 18th International Conference on Electrical Machines*, Sept. 2008, pp. 1–5.
- [30] E. B. Agamloh and A. Cavagnino, "High efficiency design of induction machines for industrial applications," in *2013 IEEE Workshop on Electrical Machines Design, Control and Diagnosis (WEMDCD)*, March 2013, pp. 33–46.

- [31] J. Hendershot and T. Miller, *Design of Brushless Permanent-Magnet Machines*. Motor Design Books, 2010.
- [32] S. Huang, J. Luo, F. Leonardi, and T. A. Lipo, “A general approach to sizing and power density equations for comparison of electrical machines,” *IEEE Transactions on Industry Applications*, vol. 34, no. 1, pp. 92–97, Jan. 1998.
- [33] M. Popescu, D. A. Staton, A. Boglietti, A. Cavagnino, D. Hawkins, and J. Goss, “Modern heat extraction systems for power traction machines—a review,” *IEEE Transactions on Industry Applications*, vol. 52, no. 3, pp. 2167–2175, May 2016.
- [34] W. Tong, *Mechanical Design of Electric Motors*. CRC Press, 2014.
- [35] J. Gieras, *Advancements in Electric Machines*. Springer, 2008.
- [36] A. Binder and T. Schneider, “High-speed inverter-fed ac drives,” in *2007 International Aegean Conference on Electrical Machines and Power Electronics*, Sept. 2007, pp. 9–16.
- [37] J. F. Gieras, “Multimegawatt synchronous generators for airborne applications: A review,” in *2013 International Electric Machines Drives Conference*, May 2013, pp. 626–633.
- [38] K. Halbach, “Design of permanent multipole magnets with oriented rare earth cobalt material,” *Nuclear Instruments and Methods*, vol. 169, no. 1, pp. 1 – 10, 1980. [Online]. Available: <http://www.sciencedirect.com/science/article/pii/0029554X80900944>
- [39] X. Yi, R. Sanchez, K. Haran, J. Veres, A. T. Perry, and P. J. Ansell, “Self-pumped air-cooling design for a high-speed high-specific-power motor,” in *2018 IEEE Transportation Electrification Conference and Expo (ITEC)*, June 2018, pp. 274–279.
- [40] J. Gieras, “New applications of synchronous generators,” *Przegląd Elektrotechniczny*, vol. 88, pp. 150–157, Sept. 2012.
- [41] Launchpoint Motors. [Online]. Available: <http://www.launchpnt.com/portfolio/aerospace/electric-machines-for-propulsion/>
- [42] A. V. Radun, “High-power density switched reluctance motor drive for aerospace applications,” *IEEE Transactions on Industry Applications*, vol. 28, no. 1, pp. 113–119, Jan. 1992.
- [43] A. Borisavljevic, *Limits, Modeling and Design of High-Speed Permanent Magnet Machines*. Springer, 2012.

- [44] Y. Chen, R. Sanchez, A. Yoon, and K. S. Haran, "Mechanical design considerations of an ironless, high-specific-power electric machine," *IEEE Transactions on Transportation Electrification*, vol. 3, no. 4, pp. 855–863, Dec. 2017.
- [45] C. B. Barth, T. Foulkes, W. H. Chung, T. Modeer, P. Assem, Y. Lei, and R. C. N. Pilawa-Podgurski, "Design and control of a GaN-based, 13-level, flying capacitor multilevel inverter," in *2016 IEEE 17th Workshop on Control and Modeling for Power Electronics (COMPEL)*, June 2016, pp. 1–6.
- [46] J. R. Melcher, *Continuum Electromechanics*. MIT Press, Cambridge, MA, 1981.
- [47] C. P. Steinmetz, "On the law of hysteresis," *Proceedings of the IEEE*, vol. 72, no. 2, pp. 197–221, Feb 1984.
- [48] T. J. E. Miller and M. I. McGilp, *PC-BDC 6.5 for Windows-Software*. SPEED Laboratory, Univ. Glasgow, Glasgow, UK, 2004.
- [49] D. M. Ionel, M. Popescu, S. J. Dellinger, T. J. E. Miller, R. J. Heideman, and M. I. McGilp, "On the variation with flux and frequency of the core loss coefficients in electrical machines," *IEEE Transactions on Industry Applications*, vol. 42, no. 3, pp. 658–667, May 2006.
- [50] R. P. Wojda and M. K. Kazimierczuk, "Winding resistance of Litz-wire and multi-strand inductors," *IET Power Electronics*, vol. 5, no. 2, pp. 257–268, Feb. 2012.
- [51] M. Bartoli, N. Noferi, A. Reatti, and M. K. Kazimierczuk, "Modeling Litz-wire winding losses in high-frequency power inductors," in *PESC Record. 27th Annual IEEE Power Electronics Specialists Conference*, June 1996, pp. 1690–1696.
- [52] P. B. Reddy and T. M. Jahns, "Analysis of bundle losses in high speed machines," in *The 2010 International Power Electronics Conference - ECCE ASIA*, June 2010, pp. 2181–2188.
- [53] Xu Tang and C. R. Sullivan, "Stranded wire with uninsulated strands as a low-cost alternative to litz wire," in *IEEE 34th Annual Conference on Power Electronics Specialist, 2003. PESC '03.*, June 2003, pp. 289–295.
- [54] E. Bilgen and R. Boulos, "Functional dependence of torque coefficient of coaxial cylinders on gap width and Reynolds numbers," *Journal of Fluids Engineering*, vol. 95, no. 1, pp. 122–126, Mar. 1973. [Online]. Available: <http://dx.doi.org/10.1115/1.3446944>

- [55] P. Krause, O. Wasynczuk, S. D. Sudhoff, and S. Pekarek, *Analysis of Electric Machinery and Drive Systems*. Wiley-IEEE Press, 2013, See Appendix B: Carter’s Coefficient, pp. 626-628. [Online]. Available: <https://ieeexplore.ieee.org/document/6739372>
- [56] S. Constantinides, “Designing with thin gauge,” Arnold Magnetic Technologies. Presented at SMMA Fall Technical Conference, Oct. 2008.
- [57] J. Welstead, J. Felder, M. Guynn, B. Haller, M. Tong, S. Jones, I. Ordaz, J. Quinlan, and B. Mason, “Overview of the NASA STARC-ABL (rev. b) advanced concept,” in *One Boeing NASA Electric Aircraft Workshop*, 2017.
- [58] J. Welstead and J. L. Felder, “Conceptual design of a single-aisle turboelectric commercial transport with fuselage boundary layer ingestion,” in *AIAA SciTech Forum*, Jan. 2016. [Online]. Available: <https://arc.aiaa.org/doi/abs/10.2514/6.2016-1027>
- [59] A. K. Yoon, D. Lohan, F. Arastu, J. Xiao, and K. Haran, “Direct drive electric motor for starc-abl tail-cone propulsor,” in *AIAA Propulsion and Energy 2019 Forum*, Aug. 2019. [Online]. Available: <https://arc.aiaa.org/doi/abs/10.2514/6.2019-4516>
- [60] S. Sudhoff, *Optimization-based Design*. IEEE Press, 2014.
- [61] T. Krantz, “Gearbox weight estimation,” NASA Glenn Resesarch Center, Tech. Rep., 2002.
- [62] R. Takahata, S. Wakui, K. Miyata, K. Noma, and M. Senoo, “Analysis of rotor eccentricity on permanent magnet synchronous motor characteristics,” in *The 2010 International Power Electronics Conference - ECCE ASIA*, June 2010, pp. 1306–1311.
- [63] E. Maruyama, A. Nakahara, A. Takahashi, and K. Miyata, “Circulating current in parallel connected stator windings due to rotor eccentricity in permanent magnet motors,” in *2013 IEEE Energy Conversion Congress and Exposition*, Sept. 2013, pp. 2850–2855.
- [64] A. Foggia, J. E. Torlay, C. Corenwinder, A. Audoli, and J. Herigault, “Circulating current analysis in the parallel-connected windings of synchronous generators under abnormal operating conditions,” in *IEEE International Electric Machines and Drives Conference. IEMDC’99. Proceedings*, May 1999, pp. 634–636.
- [65] Z. Q. Zhu, L. J. Wu, and M. L. Mohd Jamil, “Distortion of back-EMF and torque of PM brushless machines due to eccentricity,” *IEEE Transactions on Magnetics*, vol. 49, no. 8, pp. 4927–4936, Aug 2013.

- [66] S. Umans, A. Fitzgerald, and C. Kingsley, *Fitzgerald and Kingsley's Electric Machinery*, 7th ed. McGraw-Hill, 2014.